**SANDIA REPORT**
SAND2022-15920
Printed November 2022

Sandia National Laboratories

# Metal Hydride Compressor for High-Pressure (875 bar) Hydrogen Delivery

Terry A. Johnson
Anne M. Mallow
Robert C. Bowman
D. Barton Smith
Lawrence M. Anovitz
Craig M. Jensen

Prepared by
Sandia National Laboratories
Albuquerque, New Mexico
87185 and Livermore,
California 94550

Issued by Sandia National Laboratories, operated for the United States Department of Energy by National Technology & Engineering Solutions of Sandia, LLC.



Available to DOE and DOE contractors from
U.S. Department of Energy
Office of Scientific and Technical Information
P.O. Box 62
Oak Ridge, TN 37831

| | |
|---|---|
| Telephone: | (865) 576-8401 |
| Facsimile: | (865) 576-5728 |
| E-Mail: | reports@osti.gov |
| Online ordering: | http://www.osti.gov/scitech |

Available to the public from
U.S. Department of Commerce
National Technical Information Service
5301 Shawnee Rd
Alexandria, VA 22312

| | |
|---|---|
| Telephone: | (800) 553-6847 |
| Facsimile: | (703) 605-6900 |
| E-Mail: | orders@ntis.gov |
| Online order: | https://classic.ntis.gov/help/order-methods/ |

## ABSTRACT

Metal hydride hydrogen compression utilizes a reversible heat-driven interaction of a hydride-forming metal alloy with hydrogen gas. This paper reports on the development of a laboratory scale two-stage Metal Hydride Compressor (MHC) system with a feed pressure of 150 bar delivering high purity H2 gas at outlet pressures up to 875 bar. Stage 1 and stage 2 $AB_2$ metal hydrides are identified based on experimental characterization of the pressure-composition-temperature (PCT) behavior of candidate materials. The selected metal hydrides are each combined with expanded natural graphite, increasing the thermal conductivity of the composites by an order of magnitude. These composites are integrated in two compressor beds with internal heat exchangers that alternate between hydrogenation and dehydrogenation cycles by thermally cycling between 20 °C and 150 °C. The prototype compressor achieved compression of hydrogen from 150 bar to 700 bar with an average flow rate of 33.6 g/hr .

## ACKNOWLEDGEMENTS

Funding for this effort was provided by the US Department of Energy Hydrogen and Fuel Cell Technologies Office. The authors would like to acknowledge the work of a number of individuals that contributed to this project. Project concept, metal hydride identification and high-pressure alloy characterization was led by project partner Robert Bowman (ORNL). High-pressure alloy characterization was carried out by project partners Robert Bowman, Bart Smith, and Larry Anovitz (ORNL) and Martin Sulic (GWE). Low-pressure alloy characterization and sourcing and procurement of metal hydrides and prototype compressor components was led by project partner Craig Jensen (HHC). Low-pressure alloy characterization was carried out by Stephen Kim (HHC). Geoffrey Grimmett (HHC) assisted in metal hydride pellet fabrication for the prototype compressor. The design of the prototype compressor system was performed with the help of Brendan Davis who also carried out the assembly of the compressor beds, design and development of the test apparatus and balance of plant.

## CONTENTS

## LIST OF FIGURES

## LIST OF TABLES

This page left blank

# ACRONYMS AND DEFINITIONS

| Abbreviation | Definition |
|---|---|
| MH | Metal hydride |
| MHC | Metal hydride compressor |
| ORNL | Oak Ridge National Laboratory |
| HHC | Hawaii Hydrogen Carriers |
| SNL | Sandia National Laboratories |
| LP | Low-pressure |
| HP | High-pressure |
| GfE | GfE Metalle und Materialien GmbH |
| JMC | Japan Metals and Chemicals |
| PCT | Pressure-composition-temperature |
| HZG | Helmholtz Zentrum Geesthacht |
| GWE | Green Way Energy |
| SMR | Steam methane reforming |
| COP | Coefficient of performance |
| VCC | Vapor compression cycle |
| AHP | Absorption heat pump |
| HTHP | High-temperature heat pump |
| VHTHP | Very high-temperature heat pump |
| GWP | Global warming potential |
| TRL | Technology readiness level |
| HTC | Heat transfer coefficient |
| HTF | Heat transfer fluid |
| Re | Reynolds number |
| Pr | Prandtl number |
| Nu | Nusselt number |
| ID | Inner diameter |
| OD | Outer diameter |
| Peq | Equilibrium pressure |
| ENG | Expanded natural graphite |
| HiP | High Pressure Equipment |
| FMECA | Failure modes effects and criticality analysis |
| P&ID | Piping and instrumentation diagram |
| HEML | Hydrogen Effects on Materials Laboratory |

| Abbreviation | Definition |
|---|---|
| MAWP | Maximum allowable working pressure |
| DAQ | Data acquisition |
| BP | Back pressure |

# 1. INTRODUCTION

The Metal Hydride Compressor project was motivated by the desire to develop improved technologies for high pressure compression of hydrogen, specifically for hydrogen refueling stations. Conventional hydrogen compressors often contribute over half of the station cost [1]. Fatigue associated with their moving parts, including cracking of diaphragms and failure of seals, leads to failure in conventional compressors, which is exacerbated by the repeated starts and stops expected at fueling stations. Furthermore, the conventional lubrication of these compressors with oil is generally unacceptable at fueling stations due to potential fuel contamination.

Metal hydride (MH) compression is currently at early stages of R&D. Potential advantages of this concept include simplicity in design and operation, absence of moving parts, compactness, safety and reliability, and the possibility to utilize waste industrial heat where available instead of locally generated or purchased electricity for much, if not all, of the heating of the MH compressor beds.

MH hydrogen compression utilizes a reversible heat-driven interaction of a hydride-forming metal, alloy, or intermetallic compound with hydrogen gas to form the MH phase and is a promising process for hydrogen energy applications [2, 3]. Equilibrium of this reaction is based on the relation between the hydrogen pressure, concentration of hydrogen in the solid phase, and temperature. As shown in Figure 1-1, during hydrogenation and dehydrogenation, hydrogen atoms form an interstitial solid solution in the metal matrix in α-phase (low hydrogen concentration) or β-phase (high hydrogen concentration). During the transition between α-phase and β-phase, a first order phase transition occurs at a nearly constant hydrogen pressure, referred to as the plateau pressure. The width of the pressure plateau is representative of the reversible hydrogen capacity of the material over which MHC systems are designed to operate; the relationship between the plateau pressure, the operational temperature, and the thermodynamics of hydride formation is described by the van't Hoff equation:

$$\ln\left(\frac{P_p}{P^0}\right) = \frac{\Delta S^0}{R} + \frac{\Delta H^0}{RT} \quad (1)$$

where $P^0 = 1.013$ bar, $\Delta S^0$ and $\Delta H^0$ are the standard entropy and enthalpy of hydride formation, and R is the gas constant. This is shown graphically in the right-hand plot in Figure 1-1. Since $P_p$ increases exponentially with temperature, low temperature ($T_L$) hydrogen absorption occurs at a lower pressure accompanied by a release of heat, and high temperature ($T_H$) hydrogen desorption occurs at a higher pressure during which heat is absorbed [2]. This is shown in Figure 1-2 for an idealized metal hydride. As effective hydrogenation and dehydrogenation for compressor operation rely on maintaining $T_L$ and $T_H$, respectively, enhanced heat transfer is necessary to achieve good performance from the compressor beds due to the associated release and absorption of heat during the reactions.

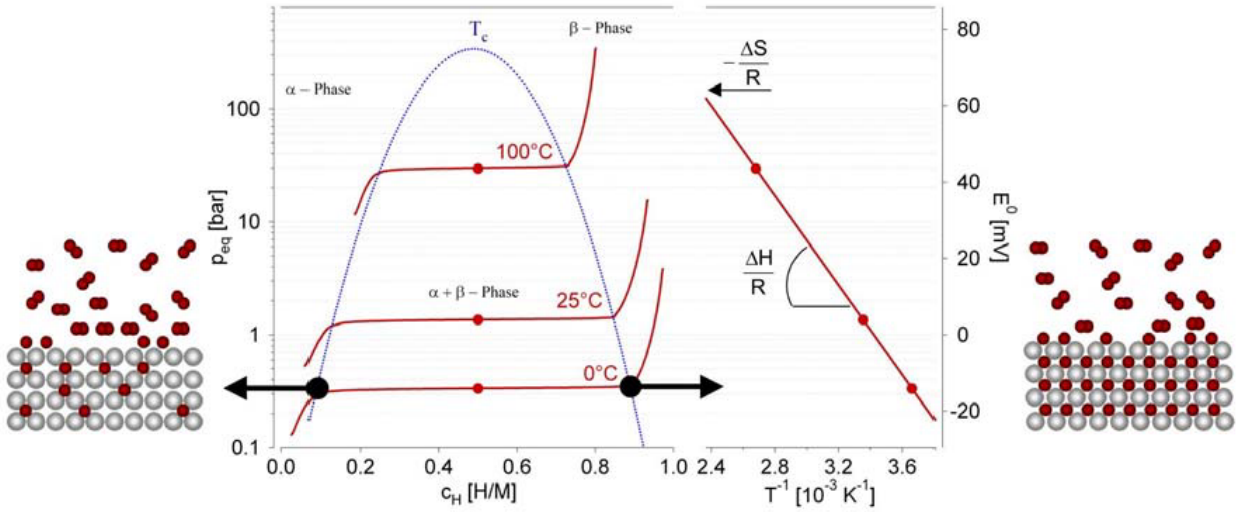


**Figure 1-1. Pressure-Composition-Temperature (PCT) isotherms for a prototype interstitial metal hydrogen system [4].**

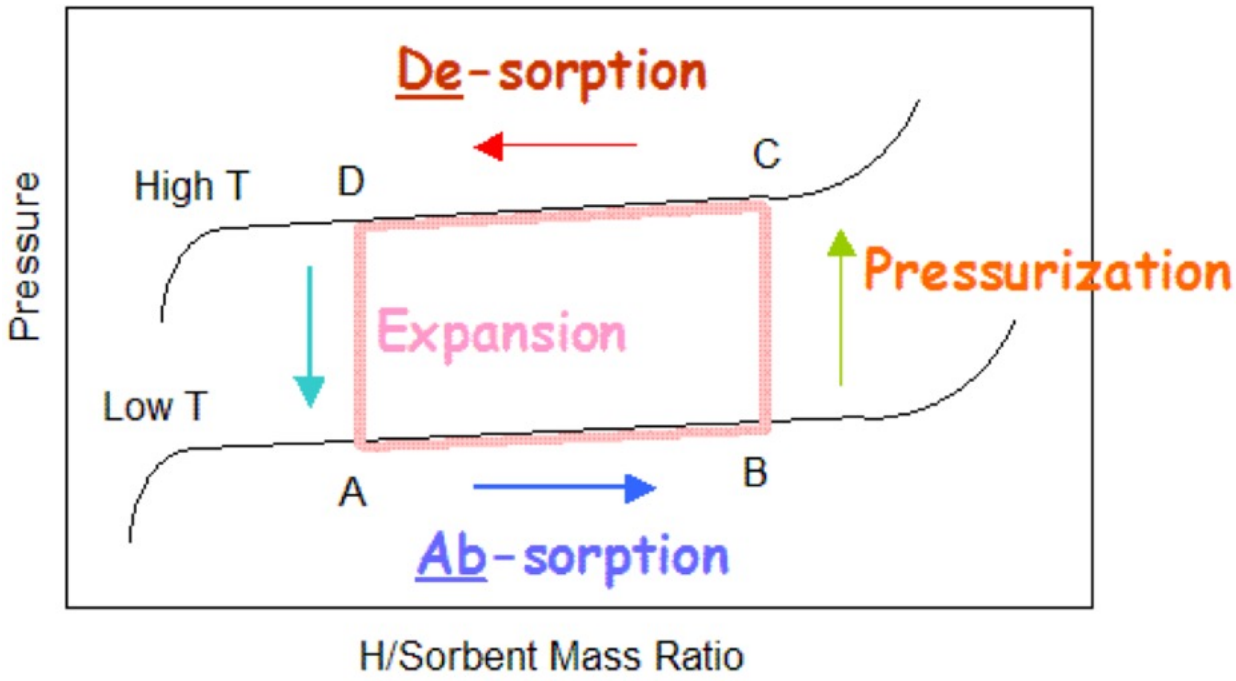


**Figure 1-2. Idealized schematic of the hydrogen compression cycle for metal hydrides.**

Heat transfer within the metal hydride relies on both thermal conductivity enhancement of the MH composite and heat exchanger design. High conductivity material additives, such as graphite or aluminum [5], as well as internal features (foam, plates, fins, etc.) have been used to increase the effective conductivity of the metal hydride . Regarding the accompanying heat exchanger design, three different concepts are commonly found in the literature: shell and tube [6-8], cylinder with internal heat exchange [9], and cylinder with external heat exchange [10-13]. All design concepts have various benefits and challenges. Shell and tube designs are conceptually easy to design and have high heat transfer rates due to high surface area to volume ratio. However, these designs may require

considerable welding, complex gas manifolds, and many tubes which translates to higher cost. Cylinders with external heat exchange have fewer parts, fittings, and welds, but likely require significant internal heat transfer enhancement that can be complex and expensive. Cylinders with an internal heat exchanger have the potential to be more energy efficient due to minimal external heat loss and may be less expensive since fewer cylinders are required compared to the shell and tube design. However, design of the internal heat exchanger to integrate with the MH composite poses difficulties. Additionally, all internal components must be rated to the operating pressure of the compressor.

In addition to enhanced heat transfer, metal hydride compressor designs must consider the material issues of hysteresis and plateau slope of the metal hydride reaction [2]. Hysteresis in metal hydrides is the existence of higher plateau pressure for hydrogen absorption than for hydrogen desorption at a given temperature. Additionally, the plateau pressure can be sloped due to variation in the chemical potential of the MH during hydrogen uptake and release. Considering this non-ideal behavior due to hysteresis and plateau slope, hydrogen compression for real systems requires higher source pressures and lower delivery pressures for the same temperature range than the ideal values predicted by the van't Hoff equation. A consequence of this behavior is that the achievable compression ratio under reasonable conditions is low, seldom exceeding 5-10 with a temperature swing of 100 K. This effect is shown in Figure 1-3 for $La_{0.85}Ce_{0.15}Ni_5$ where a realistic compression ratio of only 3.9 is achieved once hysteresis and plateau slope are taken into account. To reach the capacity at point B at 20 °C, a higher absorption pressure is required due to hysteresis and the sloping equilibrium pressure than predicted by the van't Hoff equation. Once heated to 150 °C, the lower equilibrium pressure due to hysteresis and plateau slope result in a lower delivery pressure at point C. Thus, multi-stage compression is required to reach higher compression ratios with modest operating temperatures [2]. With this approach, different metal hydrides are typically used for each stage which introduces additional complexities as the system design must appropriately couple both temperature and pressure responses of the MH materials.

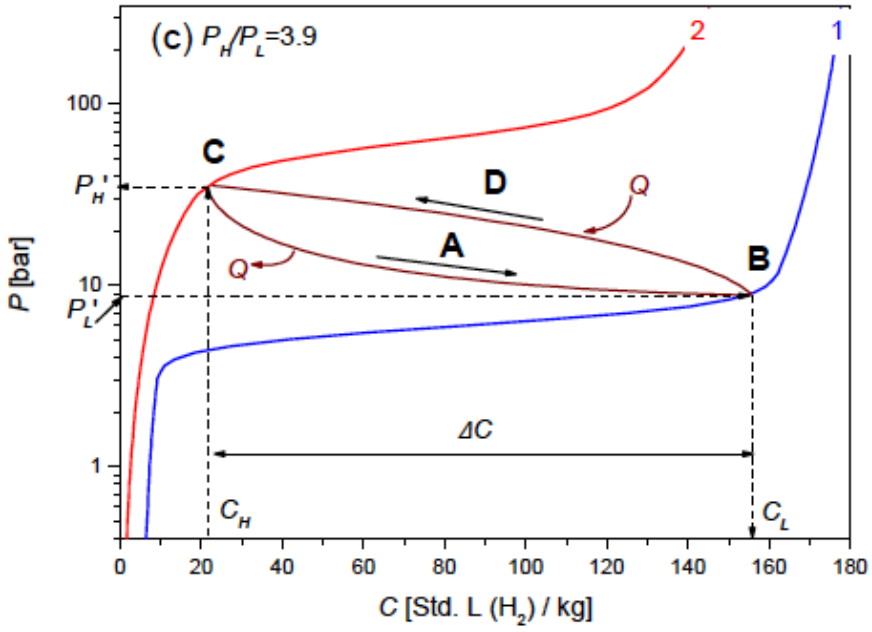


**Figure 1-3. Pressure – composition isotherms at $T_L$=20 °C (1) and $T_H$=150 °C (2) for$La_{0.85}Ce_{0.15}Ni_5$ [2].**

The operation of a two-stage MHC system is depicted in Figure 1-4. The black lines represent the van't Hoff plot for the hydrogenation process for Stage 1 (lower black line) and for Stage 2 (upper black line). The dashed red line represents the coupling between Stage 1 and Stage 2. The compression cycle is summarized as follows:

- Step A: A low-pressure $H_2$ supply is attached to the first stage at pressure $P_s$. The temperature of Stage 1 is maintained at $T_L$ during hydrogenation resulting in state B.
- Step B-C: A sensible heating process raises the bed temperature to $T_H$, increasing the pressure of the stage 1 vessel.
- Step D-E: Coupling between Stage 1 (dehydrogenation at $T_H$) and Stage 2 (hydrogenation at $T_L$) occurs resulting state F for Stage 2.
- Step F-G: Stage 2 hydride bed undergoes sensible heating to achieve the delivery pressure of $P_d$.
- Step H: During dehydrogenation of stage 2, high-pressure hydrogen is released from the compressor at $P_d$.

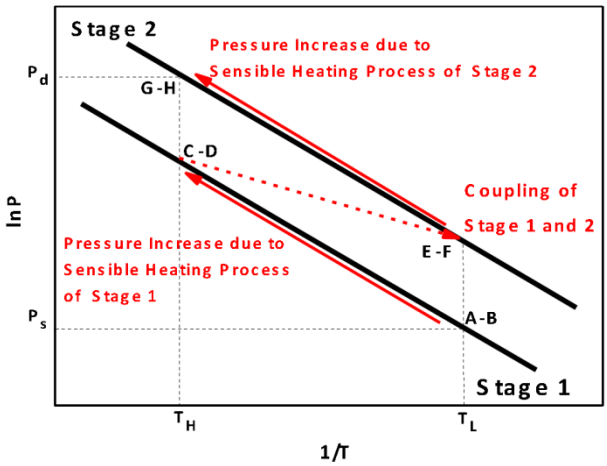


**Figure 1-4. van't Hoff plots illustrating the operation of a two-stage Metal Hydride Hydrogen Compression system from low temperature $T_L$ to high temperature $T_H$ [3].**

Figure 1-5 provides a layout of a two-stage hydride compressor described by Figure 1-4. To continuously deliver hydrogen, each stage of the compressor must consist of multiple MH beds with synchronized hydrogenation and dehydrogenation cycles. The lower pressure (LP) alloy is placed in the first stage compressor beds (A1.1, A1.2), and the higher pressure (HP) MH is loaded into the second stage compressor beds (A2.1, A2.2) to provide a quasi-continuous supply of pressurized $H_2$ at the delivery pressure $P_d$. During Step 1 (red dashed lines) bed A1.1 is cooled while being filled from the low pressure source at $P_L$ while bed A2.2 is heated to deliver hydrogen at the high pressure $P_H$. Simultaneously, bed A1.2 is heated to deliver hydrogen to bed A2.1 which is cooled. When this half cycle completes, heating and cooling are switched to carry out Step 2 (red dotted lines) in which bed A1.2 is filled, bed A2.1 delivers high pressure hydrogen and bed A1.1 delivers hydrogen to fill bed A2.2. Such multi-stage operation allows achievement of higher overall compression ratios using the same or smaller temperature swings compared to single stage compressors.

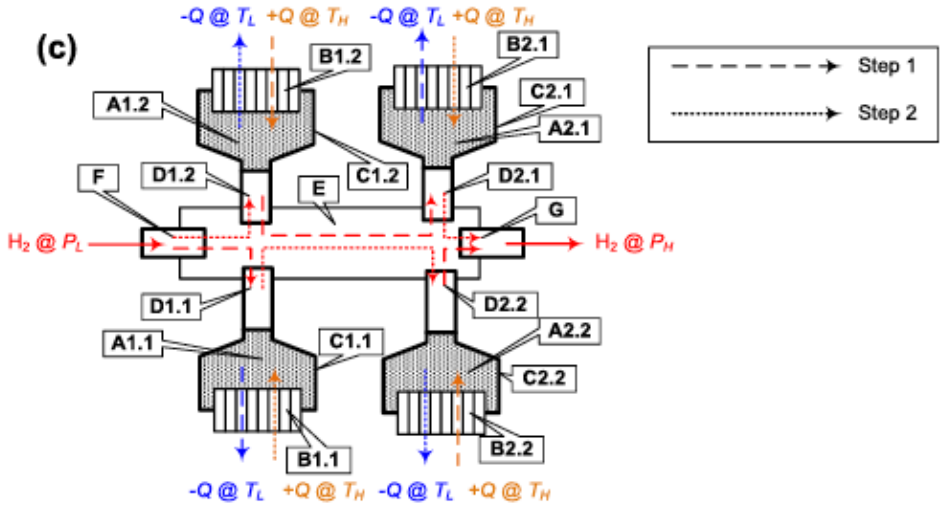


**Figure 1-5. Schematic layout of two-stage MH compressor using two alloys differing by thermal stabilities of their hydrides [2].**

Multi-stage MHC feasibility has been known with various demonstration and limited commercial units being offered for a number of years. For example, using the desorption isotherms of intermetallic alloys $La_{0.85}Ce_{0.15}Ni_5$ (1) and C14-$Ti_{0.65}Zr_{0.35}(Mn,Cr,Fe,Ni)_2$ (2), Yartys et al. [3] describes how during a two-stage operation it is possible to achieve $H_2$ compression from $P_L(1)$ = 3.5 atm to $P_H(2)$ = 261 atm (i.e., a compression ratio 74.6) over the temperature range from 20 °C to 130 °C. Additionally, the team reports on the fabrication and performance testing of a two-stage hydride compressor using $AB_5$ and $AB_2$ alloys that compressed $H_2$ from 10 bar to 200 bar with an output flow rate of 10 $Nm^3$/hr (0.4 kg $H_2$/hr) over a heating range between 20 °C and 150 °C [3]. The experimental compression factor of 20 is reasonably close to the value predicted by simulations using absorption and desorption isotherms and points out the necessity of reliably measuring these actual pressures for the candidate hydrides at their operating temperatures. Karagiorgis et al. [9] summarizes published data on various multi-stage metal hydride compressors. Only one metal hydride compressor that produced greater than 700 bar is reported [5], however, poor energy efficiency of 22.4 kWh/kg $H_2$ is exhibited by the shell and tube prototype, even when neglecting the heat loss.

The objectives of this research are to investigate and demonstrate on a laboratory scale a two-stage MH hydrogen ($H_2$) gas compressor with a feed pressure of 150 bar in order to deliver high purity $H_2$ gas at outlet pressures ≥ 875 bar using the scheme shown in Figure 1-4. To maximize the energy efficiency, an internal heat exchanger will be demonstrated for the first time with this high-pressure design. First, two MH alloys are identified for Stage 1 and Stage 2 and system-level modeling is used to assess the potential MHC performance. Next, the compressor bed design is discussed which includes the internal heat exchanger design and considerations such as energy usage, manufacturability, MH loading, and heat transfer fluid pressure drop and heat transfer coefficient. Additionally, the development of enhanced thermal conductivity composites with expanded natural graphite will be reviewed. The final prototype design and assembly is described along with that of the test apparatus. Finally, the experimental performance assessment of the prototype MHC is described.

# 2. METAL HYDRIDE SELECTION AND CHARACTERIZATION

## 2.1. Identification of Candidate Hydride Alloys

The number of potential metal-hydrogen systems is vast. Extremely diverse materials react with hydrogen gas under suitable conditions and can be used for many types of applications. A generic family tree of the types of metal hydrides that have been investigated over the past 60+ years is shown in

Figure 2-1. However, as discussed in depth by Lototskyy, et al. and Yartys, et al. [2, 3] only a relatively small subset of interstitial-type of metal hydrides have the reversibility and reaction kinetics properties appropriate to become viable candidates for hydrogen compression applications. Furthermore, other than a very few elemental hydrides (e.g., $VH_x$) nearly all of the practical hydrides for consideration in hydride compressors are crystalline intermetallic compounds with one of the crystal structures shown in Figure 2-2. Group A alloys are based upon the body-centered-cubic (BCC) metal vanadium (V) while Group B alloys are the hexagonal $AB_5$ phases. The Group C $AB_2$ phases nearly always possess either the hexagonal C14 Laves structure or the cubic C15 Laves structure. Finally, the Group D are derived from the cubic AB structure of TiFe.

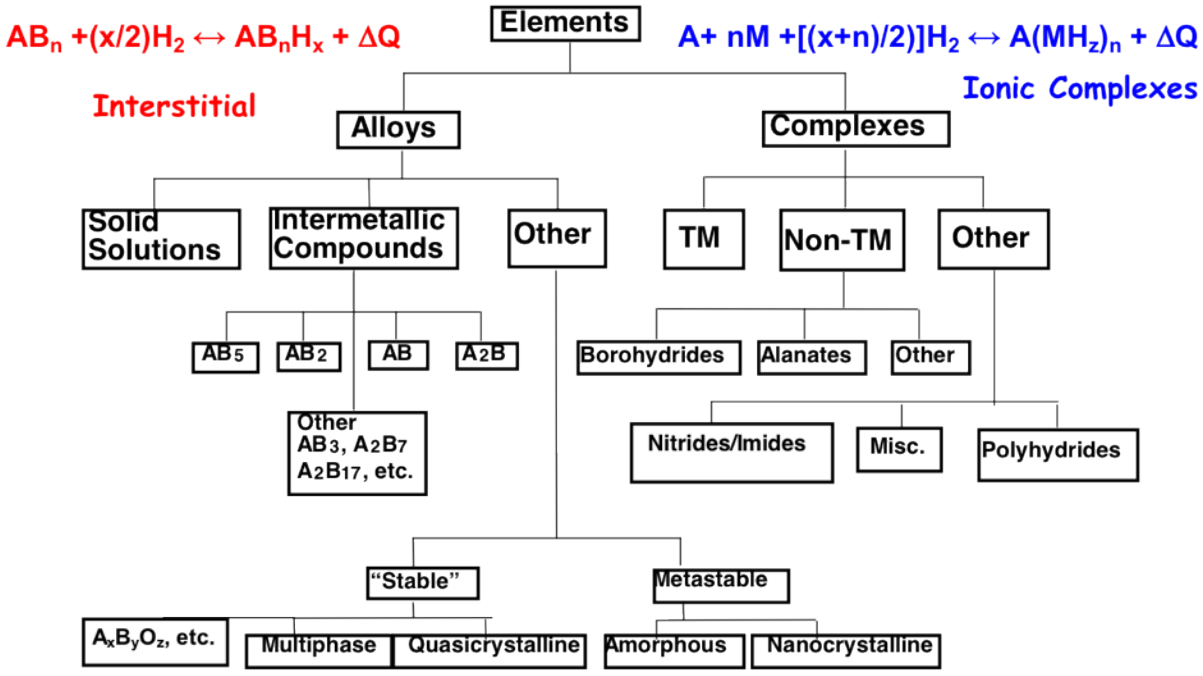


**Figure 2-1. Family Tree of Hydriding Alloys and Complexes (TM = transition metal).**

| Group (repre-sentative) | Structure of parent alloy | Structure of hydride | $\Delta V/V_0$ [%] |
|---|---|---|---|
| A (BCC-V) | 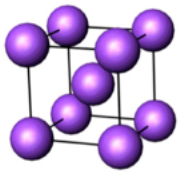 | 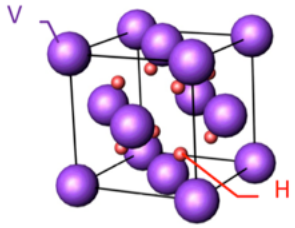 | 35.5 ($V \rightarrow VH_2$)<br>30.9 ($V_2H \rightarrow VH_2$) |
| B ($LaNi_5$) | 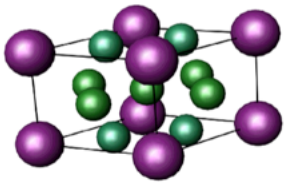 | 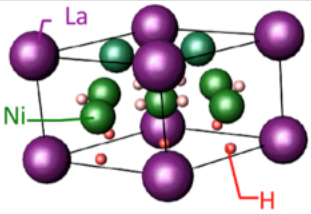 | 20.4 ($LaNi_5 \rightarrow LaNi_5H_6$) |
| C ($TiMn_2$) | 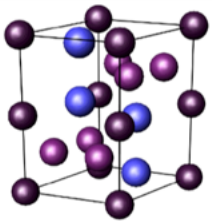 | 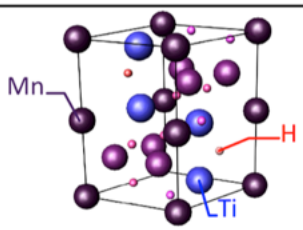 | 19.6 ($TiMn_2 \rightarrow TiMn_2H_{2.5}$) |
| D (TiFe) | 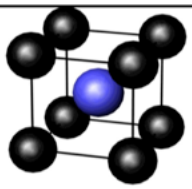 | 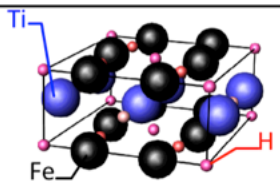 | 18.3 ($TiFe \rightarrow TiFeH_2$) |

**Figure 2-2. Crystal structures of parent and hydrogenated alloys (i.e. $AH_x$, $AB_5H_x$, $AB_2H_x$, and $ABH_x$) that are most viable for metal hydride $H_2$ compression applications [2].**

Table 2-1 provides a summary of key properties for several intermetallic alloys and alloys that were assessed by Lototskyy, et al. [2] that should be suitable for compressor applications. The data are sorted in ascending order for desorption plateau pressure at 25 °C ($P_0$) which are calculated. The lower pressure ($P_L$) and higher pressure ($P_H$) values correspond to the lower ($T_L$) and higher ($T_H$) temperatures, respectively, as reported in the original publications. Initial candidates considered during this project for 2-stage compression to greater than 700 bar are shown in blue font for the low-pressure stage (10 – 100 bar) and orange font for the high-pressure stage (50 – 900 bar).

**Table 2-1. Equilibrium characteristics of metal hydride-forming alloys suitable for $H_2$ compression [2].**

| Alloy | $-\Delta S^0$ [J/(mol $H_2$ K)] | $-\Delta H^0$ [kJ/mol $H_2$] | Temperature range [°C] | | Pressure [atm] | | |
|---|---|---|---|---|---|---|---|
| | | | $T_L$ | $T_H$ | $P_0$ | $P_L$ | $P_H$ |
| $LaNi_{4.8}Sn_{0.2}$ | 104.3 | 32.83 | 20 | 90 | 0.50 | 0.40 | 5.32 |
| | 105.0 | 32.80 | 0 | 240 | 0.55 | 0.16 | 139.9 |
| $Mm_{0.5}La_{0.5}Ni_{4.7}Sn_{0.3}$ | 111.2 | 33.80 | 25 | 80 | 0.77 | 0.77 | 6.44 |
| $LaNi_{4.8}Al_{0.2}$ | 101.6 | 30.40 | 50 | 150 | 0.96 | 2.47 | 35.84 |
| $MmNi_{4.7}Fe_{0.3}$ | 87.4 | 25.00 | 20 | 102 | 1.53 | 1.29 | 12.14 |
| $V_{0.85}Ti_{0.1}Fe_{0.05}$ | 148.0 | 42.90 | -20 | 100 | 1.64 | 0.08 | 53.14 |
| $La_{0.85}Ce_{0.15}Ni_5$ | 91.28 | 24.30 | 10 | 110 | 3.24 | 1.93 | 28.50 |
| $MmNi_{4.7}Al_{0.3}$ | 107.8 | 28.88 | 20 | 90 | 3.73 | 3.05 | 29.98 |
| $V_{92.5}Zr_{7.5}$ | 147.0 | 40.32 | 30 | 60 | 4.11 | 5.38 | 22.71 |
| $La_{0.2}Y_{0.8}Ni_{4.6}Mn_{0.4}$ | 105.3 | 27.10 | 20 | 90 | 5.62 | 4.67 | 39.78 |
| $Zr_{0.7}Ti_{0.3}Mn_2$[4] | 85.0 | 21.00 | 30 | 150 | 5.77 | 6.63 | 70.41 |
| $Ti_{0.9}Zr_{0.1}Mn_{1.4}Cr_{0.35}V_{0.2}Fe_{0.05}$[5] | 106.9 | 25.89 | 25 | 100 | 11.17 | 11.17 | 91.14 |
| $TiCr_{1.9}$ | 122.0 | 26.19 | –100 | 30 | 60.77 | 0.03 | 72.34 |
| $ZrFe_{1.8}Cr_{0.2}$ | 109.0 | 22.30 | 20 | 90 | 61.19 | 52.49 | 306.2 |
| $(Ti_{0.97}Zr_{0.03})_{1.1}Cr_{1.6}Mn_{0.4}$ | 115.0 | 23.40 | 10 | 99 | 80.80 | 49.00 | 527.9 |
| $TiCr_{1.5}Mn_{0.25}Fe_{0.25}$[5] | 101.6 | 19.32 | –10 | 165 | 83.61 | 29.65 | 1009 |
| $TiCr_{1.5}Mn_{0.2}Fe_{0.3}$[5] | 101.0 | 18.32 | –10 | 148 | 116.4 | 43.57 | 1008 |
| TiCrMn | 106.0 | 19.60 | –60 | 100 | 126.8 | 5.42 | 621.2 |

Various candidate alloys for both the low pressure (LP) and high pressure (HP) metal hydrides were identified at the start of this project from this compilation that was further augmented with other compositions based on past experience, further literature review, and design requirements for the compressor. Based on this effort, the following alloys were selected for more detailed assessments:

<u>High Pressure Candidates (Phase and crystal structure type)</u>
1.) $TiCr_{1.6}Mn_{0.2}$ ($AB_2$ C14)
2.) $Zr_{0.8}Ti_{0.2}FeNi_{0.8}V_{0.2}$ ($AB_2$ C15)
3.) $TiCr_{1.8}$ ($AB_2$ C15)
4.) $(Ti_{0.97}Zr_{0.03})_{1.1}Cr_{1.6}Mn_{0.4}$ ($AB_2$)
5.) $TiCrMn_{0.7}Fe_{0.2}V_{0.1}$ ($AB_2$)

<u>Low Pressure Candidates (Phase and crystal structure type)</u>
1.) $MmNi_{4.7}Al_{0.3}$ ($AB_5$)
2.) $Ti_{0.9}Zr_{0.1}Mn_{1.4}Cr_{0.35}V_{0.2}Fe_{0.05}$ ($AB_2$ C14)
3.) $TiMn_{1.66}Vf_{0.34}$ ($AB_2$ C14/C15 mixed Hydralloy C1)
4.) $Ti_{0.25}Zr_{0.75}Fe_{1.0}Ni_{0.8}V_{0.2}$ ($AB_2$ C-15)
5.) $TiCr_{1.6}Mn_{0.2}$ ($AB_2$ C14)

This list was compared against alloys that could be obtained commercially to further narrow the selection. Several potential vendors who had previously produced and supplied metal hydrides were contacted to determine a reliable source for the selected hydride alloys. Of these suppliers, GfE Metalle und Materialien GmbH (GfE), Ames Laboratory at the Iowa State University, Sigma Aldrich, and Japan Metals and Chemicals (JMC) were able to provide one or more alloys of interest. Both Ames Lab and JMC claimed the ability to produce any of the candidate alloys of interest. In addition, it was

determined that Sandia had possession of ~100kg of GfE Hydralloy C5 ($Ti_{0.955}Zr_{0.045}Mn_{1.52}V_{0.43}Fe_{0.12}Al_{0.03}$) from a previous project, which was identified as an additional LP alloy candidate.

With promising lists of materials for both LP and HP stages of the compressor, small samples of many of the candidates were procured for the purpose of experimental characterization. The characterization was to consist of pressure-composition-temperature (PCT) measurements of the candidate materials at the temperatures and pressures of interest for the compressor design. This data was meant to verify and/or supplement literature PCT data.

Alloy samples were purchased from Ames Lab and JMC. Whereas JMC would only provide alloys that they had in-stock, Ames Lab custom synthesized 50-gram samples via arc-melting with heat treatments specified by team members at Oak Ridge National Laboratory (ORNL). Three alloy samples were initially fabricated by Ames Laboratory which were all titanium-based $AB_2$-type metal hydrides: 1) $Ti_{0.95}Zr_{0.05}Cr_{1.2}Mn_{0.75}V_{0.05}$ [14], 2) $Ti_{0.8}Zr_{0.2}Fe_{1.6}V_{0.4}$ [15], and 3) $TiCrMn_{0.7}Fe_{0.2}V_{0.1}$ [16]. These will be referred to as Ames #1, #2, and #3 respectively for brevity. An additional alloy was later produced by Ames based on the Ames #2 composition, but with nickel substitution for the iron (i.e., $Ti_{0.6}Zr_{0.4}Fe_{1.0}Ni_{0.6}V_{0.4}$ [15]). This material was formulated to try to produce flatter plateau pressures with somewhat lower pressure than Ames #2 and is referred to as Ames #4. The published isotherms are cited for these alloys.

JMC provided two alloy samples: 1) $Zr_{0.75}Ti_{0.25}FeNi_{0.8}V_{0.2}$ which was a low-pressure hydride candidate and 2) $Ti_{1.0}Cr_{1.0}M_{n0.7}Fe_{0.2}V_{0.1}$ which was the same nominal composition as Ames alloy #3. The reason for the repeated sample was to determine if there was a difference between the processing techniques of Ames and JMC. In addition, sample material of the GfE Hydralloy C5 alloy $Ti_{0.955}Zr_{0.045}Mn_{1.52}V_{0.43}Fe_{0.12}Al_{0.03}$ [17] was provided for characterization as a LP candidate.

## 2.2. Assessment of MH Alloys for the High-Pressure Hydride Compressor

**Ames Laboratory (Only high-pressure alloys)**

1.) $Ti_{0.95}Zr_{0.05}Cr_{1.20}Mn_{0.75}V_{0.05}$ [14] (referenced in this report as Ames Lab alloy #1)

2.) $Ti_{0.8}Zr_{0.2}Fe_{1.6}V_{0.4}$ [15] (Referenced as Ames Lab alloy #2; note three separate preparations #2A, #2B and #2C were made at Ames, and all three were tested at ORNL. Alloys #2A and #2C were also tested by GreenWay Energy (GWE).

3.) $Ti_{1.0}Cr_{1.0}M_{n0.7}Fe_{0.2}V_{0.1}$ [16] (Ames Lab alloy #3) – Only GreenWay Energy (GWE) made isotherm measurements on this material

4.) $Ti_{0.6}Zr_{0.4}Fe_{1.0}Ni_{0.6}V_{0.4}$ [15] (Ames Lab alloy #4) – Only GWE made isotherm measurements on this material

**Japan Metals Corporation (JMC) – both high- and low-pressure alloys**

1.) $Ti_{1.0}Cr_{1.0}M_{n0.7}Fe_{0.2}V_{0.1}$ [16] - same nominal composition as Ames alloy #3; however, no measurements were made at ORNL on this material. It was provided to the Helmholtz Zentrum Geesthacht (HZG) in Germany for possible isotherm measurements there in the future. [Status (Sept. 1, 2019): No isotherm measurements made at HZG due to unresolved issues with operation and calibration of their newly constructed Sieverts apparatus.

2.) $Zr_{0.75}Ti_{0.25}FeNi_{0.8}V_{0.2}$ (A low-pressure hydride candidate that was purchased from JMC & characterized by HHC in 2017) [Status Sept. 1, 2019): No isotherm measurements were made.

In addition, sample material of the GfE Hydralloy C5 alloy $Ti_{0.955}Zr_{0.045}Mn_{1.52}V_{0.43}Fe_{0.12}Al_{0.03}$ [17] was provided to ORNL by SNL. Some this material was subsequently forwarded to GWE who measured isotherms at 22°C, 70°C, and 150°C.

The goal of the MH assessment was to select one alloy each for the LP and HP stages of the compressor. The target for the LP metal hydride was absorption at 20°C with a feed pressure of 100 bar and the capability of desorbing at an appropriate pressure when heated to 150°C for the absorption of a high-pressure metal hydride. In turn, the HP alloy would absorb at 20°C and produce 875 bar when heated to 150°C. The following is a brief summary of the results of the characterization of five candidate alloys. The alloys were assessed using PCT measurements targeting the temperature and pressure ranges needed for the compressor design.

### *2.2.1. Test Apparatus*

Low-pressure candidate materials were screened at Sandia National Laboratories in a PCT Pro 1000, capable of measurements up to 200 bar and 400°C. Additionally, low pressure alloys were characterized at Hawaii Hydrogen Carriers (HHC) using a Suzuki Shokan 2 channel thermo-volumetric analyzer capable of measurements up to 150 bar and 150°C. Note that because the pressure capability of these two systems wasn't high enough for the targeted desorption pressure of the LP stage, the most promising LP materials were also characterized at ORNL.

Characterizations of four identified high-pressure alloys produced at Ames Laboratory was performed by ORNL. In addition, GreenWay Energy (GWE), who was leading a related hybrid electrochemical-metal hydride compressor project, collaborated with our team on material characterization. GWE had assembled their own high-pressure Sievert's apparatus and performed PCT characterization on three materials of their choosing along with four of our team's alloys. The alloys chosen for characterization by GWE were $Ti_{1.1}CrMn$, $(Ti_{0.97}Zr_{0.03})_{1.1}Cr_{1.6}Mn_{0.4}$, and $TiCr_{1.55}Mn_{0.2}Fe_{0.2}$.

To carry out PCT measurements, ORNL designed and fabricated a custom, high-pressure Sievert's apparatus capable of accurate isotherm measurements up to 1000 bar and 175°C. The original configuration of this high-pressure Sievert's system design is shown in Figure 2-3, while a photograph of the system is given in Figure 2-4. The sample reactor and gas-handling manifold is situated inside the rectangular perimeter of the T-slotted framing. Below the manifold is the vacuum station consisting of an oil-less scroll pump and turbomolecular pump. An external high-pressure gas booster provides high-pressure hydrogen for absorption measurements, and each component is routinely tested for high-pressure leaks using a helium leak detector. The design incorporated ideas and practices from similar high-pressure cycling stations at both Jet Propulsion Laboratory and Sandia National Laboratories (SNL; HyMARC Project) as well as several literature sources. The design focuses on minimizing internal volume to enable measurements of small quantities of hydride alloys and made use of the existing laboratory infrastructure at ORNL as much as possible.

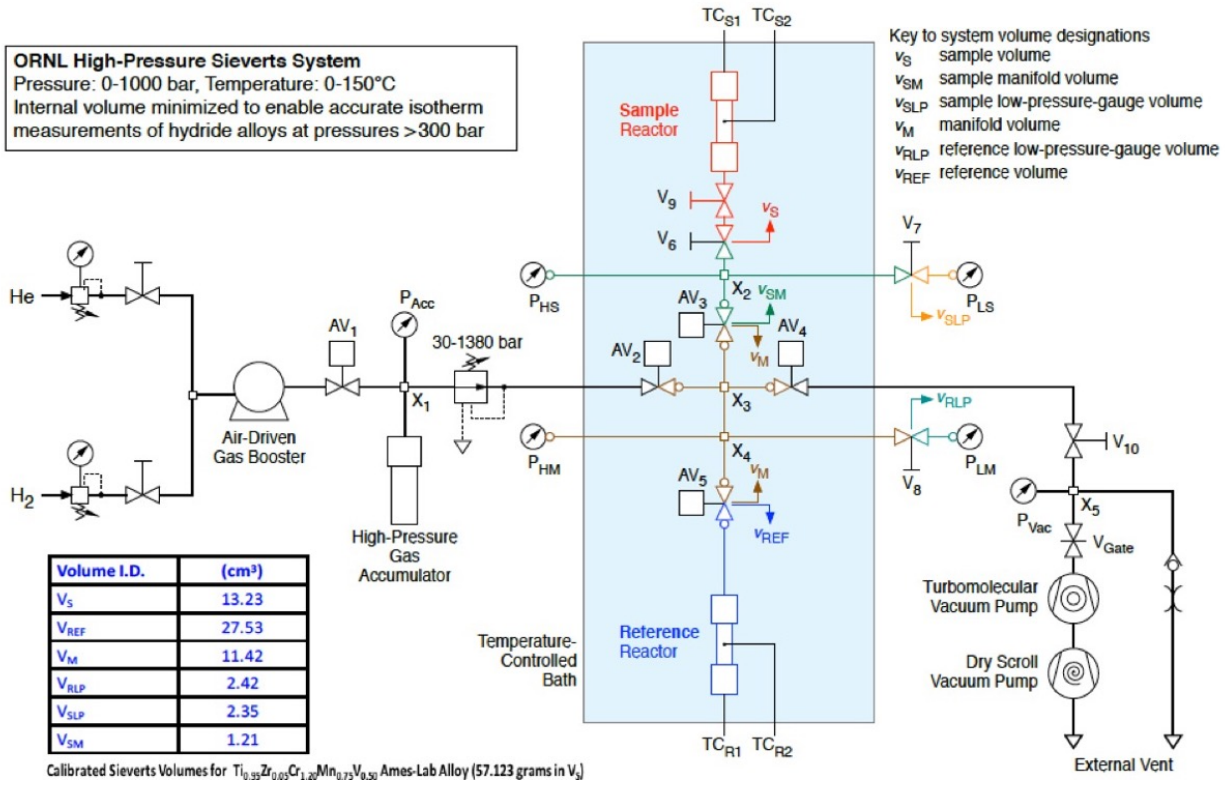


**Figure 2-3. Schematic of initial design of the ORNL Sieverts system.**

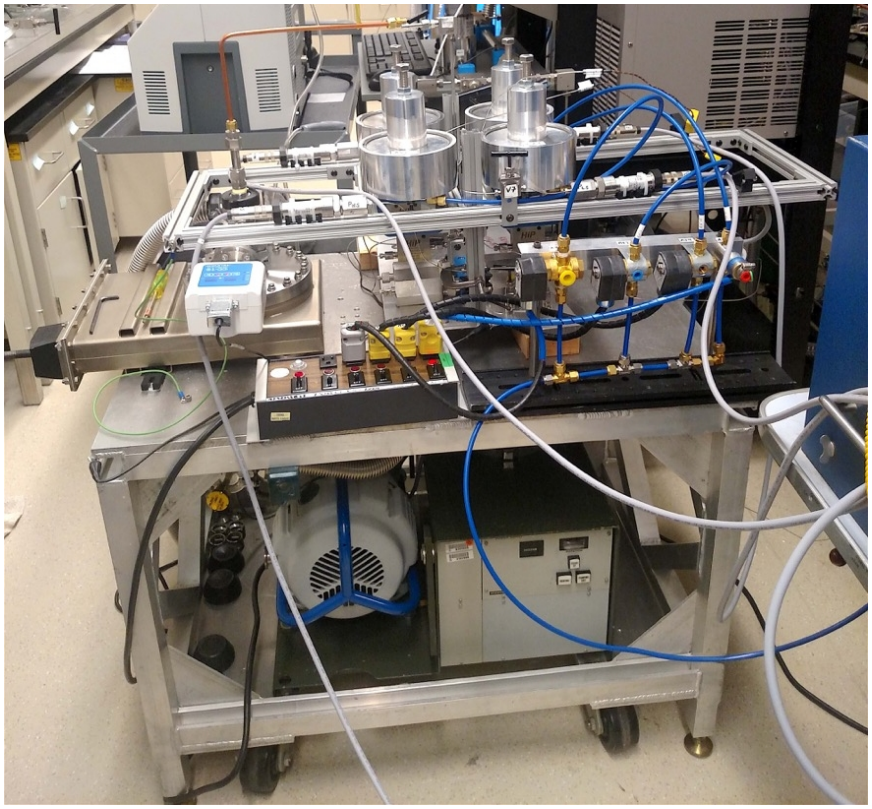

**Figure 2-4. Photograph of the complete Sieverts System setup in ORNL Building 4100.**

A schematic drawing of the ORNL sample reactor is given in Figure 2-5 and a photograph of the unassembled sample reactor vessel components is shown in Figure 2-6.

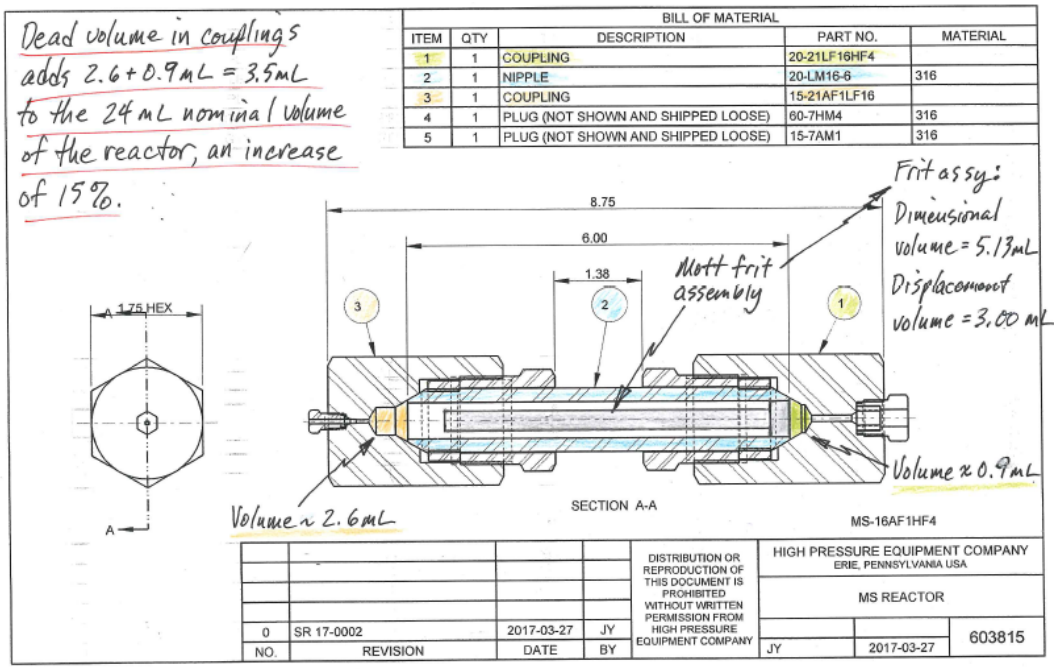


**Figure 2-5. Schematic Drawing of ORNL Hydride Reactor.**


**Figure 2-6. Photograph of unassembled components including isolation valve and Mott porous filter tube.**

Figure 2-7 (left) shows isotherms of the Hydralloy C5 alloy provided by SNL and measured at HHC. This result is consistent with literature data for the alloy at up to 50 °C but provides higher temperature and pressure data not previously measured. The isotherms indicate that Hydralloy C5 is a viable candidate for the low-pressure stage of the compressor.

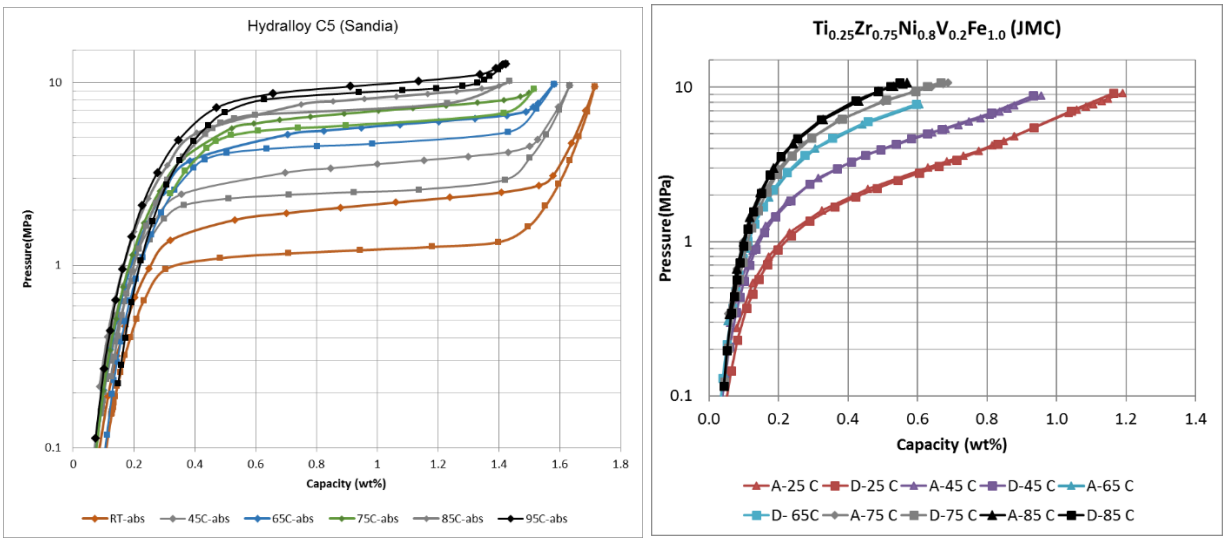


**Figure 2-7. PCT measurements of Hydralloy C5 (left) and JMC low pressure candidate (right).**

The second low pressure candidate, $Zr_{0.8}Ti_{0.2}FeNi_{0.8}V_{0.2}$, was also measured at HHC, but the alloy showed significant slope in plateau pressures as shown in Figure 2-7 (right). It is suspected that the material may not have been sufficiently annealed resulting in highly disordered distributions of metal atoms in the crystal structure. In a previously published study [15] a similar alloy had been annealed in evacuated quartz tubes at 900°C for 240 hours and quenched in cold water. For this material, the 20°C absorption isotherms had relatively small slopes across the plateau regions as well as very little hysteresis. Given the good performance found for Hydralloy C5, no further investigation in this issue was carried out.

Initially characterized at ORNL, the Ames #1 material ($Ti_{0.95}Zr_{0.05}Cr_{1.20}Mn_{0.75}V_{0.05}$) showed a room temperature absorption isotherm (Figure 2-8) which was consistent with literature data indicating that it could easily be filled by the low-pressure stage at a reasonable temperature. Desorption pressure from the alloy was then measured at up to 180°C displaying desorption pressures in excess of 875 bar. While complete isotherms were not measured at ORNL to these temperatures, the discrete measurements indicated that the alloy was a potential candidate for the high-pressure stage of the compressor. Subsequent characterization data obtained at GWE at temperatures between 22°C and 170°C is shown in Figure 2-9. While the material could produce high pressure, the isotherms indicate that temperature in excess of 170°C would be required to deliver greater than 700 bar over a reasonable capacity range. This temperature range was beyond the planned operating range of the compressor design.

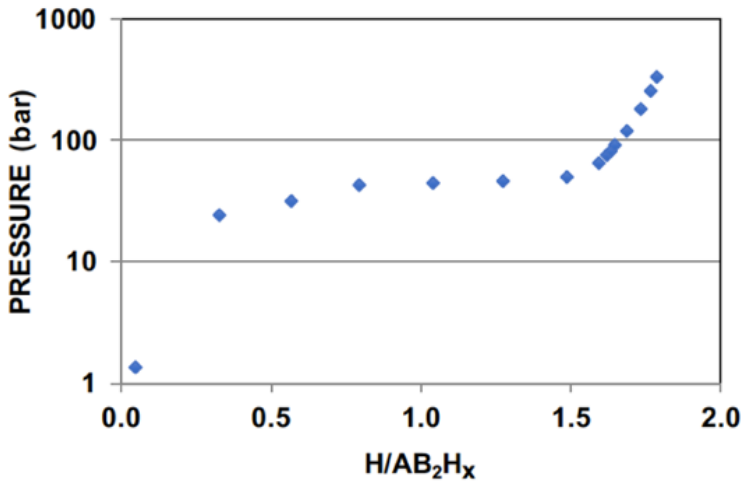


**Figure 2-8. Absorption isotherm of Ames #1 at 24°C (ORNL).**

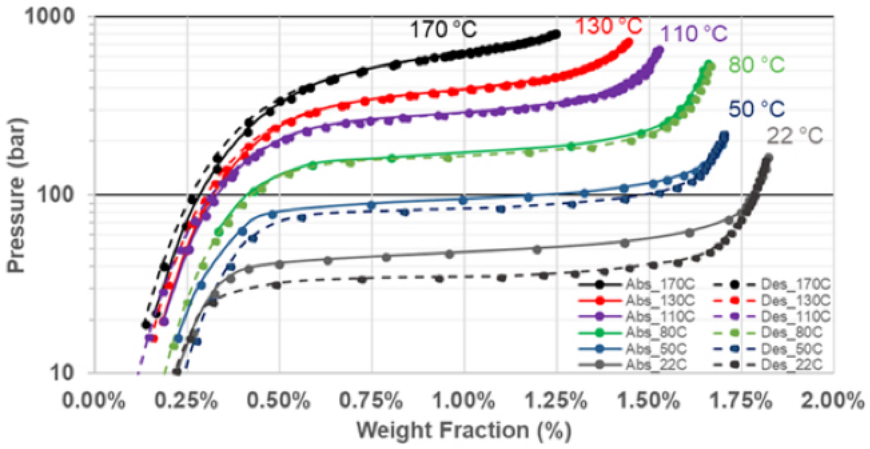


**Figure 2-9. Absorption/Desorption Isotherms for Ames #1 (GWE).**

Ames #2 ($Ti_{0.8}Zr_{0.2}Fe_{1.6}V_{0.4}$) was found to have the highest desorption pressure capability of all the alloys tested during this project. Isotherms of this alloy were measured at ORNL and GWE. As Figure 2-10 shows for two different samples measured by ORNL (Ames #2 and #2B), room temperature absorption requires greater than 400 bar pressure to reach a capacity greater than 1.5 wt%. The isotherm on the right in Figure 2-10 shows that a pressure greater than 875 bar can be desorbed from the alloy at 150°C. This result indicated that Ames #2 was a viable candidate for the high-pressure stage. However, the highly sloping isotherms prevent it from reaching an ideal compression ratio or capacity.

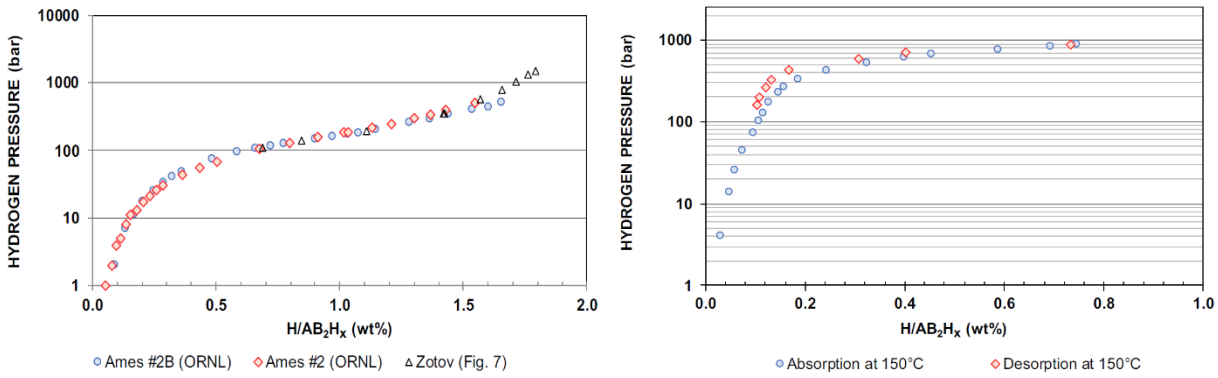


**Figure 2-10. Room Temperature (~20 °C) and 150 °C Isotherms of Ames #2 ($Ti_{0.8}Zr_{0.2}Fe_{1.6}V_{0.4}$).**

To correct this characteristic, Ames #4 was produced with the intent that the nickel substitution would flatten and slightly lower the plateau pressures. Unfortunately, the results showed that the desorption pressure was lowered too significantly, and both the absorption and desorption isotherms remained highly sloped (Figure 2-11).

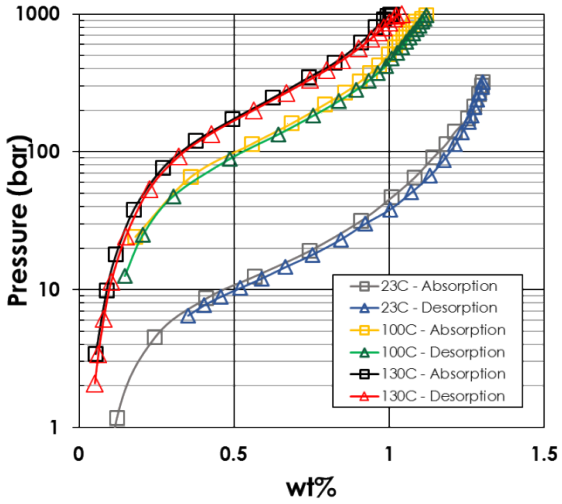


**Figure 2-11. Isotherms of Ames #4 at 23ºC, 100ºC and 130ºC.**

Based on literature data, Ames #3 held the most promise for our application with flat plateau pressures that spanned the range of interest for the high-pressure stage of the compressor. However, characterization by GWE showed that the sample tested did not produce as high a pressure as anticipated. Based on the measurements shown in Figure 2-12, the material could be filled at room temperature with about 150 bar $H_2$, but might only provide 500-600 bar pressure at 150°C, which is significantly lower than expected.

Similar results were found by GWE when characterizing their selected materials. Two of their materials had very sloped isotherms that prevented them from being viable. The third material, $Ti_{1.1}CrMn$, had relatively flat plateau pressures, but provided lower desorption pressures than anticipated. At 170°C, this material only produced 400-500 bar pressure over a reasonable capacity.

Based on the inability of either team to find an ideal high-pressure stage candidate, three options were considered for the prototype compressor demonstration. Option 1 would use Hydralloy C5 for the LP stage and Ames #3 for the HP stage and target compression from 50 to 600 bar over the temperature range of 20°C to 150°C. Option 2 would use Ames #3 for the LP stage and Ames #2 for HP stage and target compression from 150 bar to 875 bar over the same temperature range. Finally, the third option was to use a 3-stage compressor and use Hydralloy C5, Ames #3, and Ames #2 to compress from 50 to 875 bar. This 3-stage option would include additional complexity and cost to add a third compressor bed, but would increase the compression ratio.

The decision was made to retain the 2-stage approach and the goal of 875 bar output and use the Ames #3 - Ames #2 combination. Figure 2-12 and Figure 2-13 show the proposed operating temperature and pressure ranges for the prototype compressor. Note that the negative trend in wt% at high H/M ratio for Ames #3 is likely a result of imperfect volume calibration.

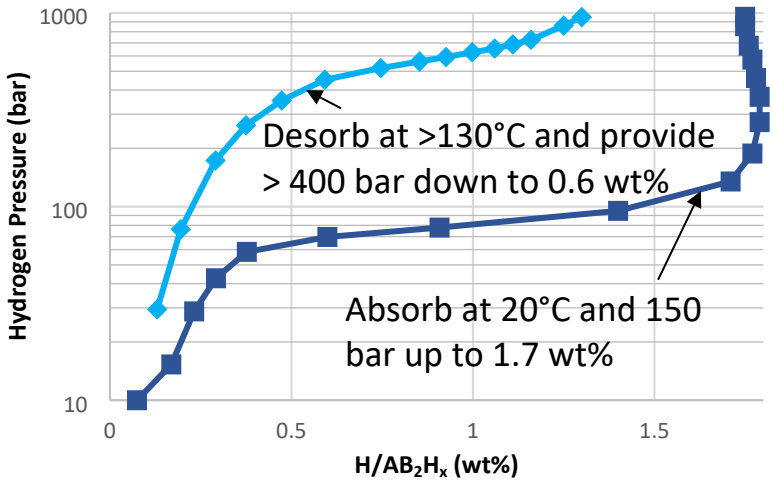


**Figure 2-12. Absorption isotherm at 20 ºC and desorption isotherm at 130 ºC for Ames #3 ($TiCrMn_{0.7}Fe_{0.2}V_{0.1}$).**

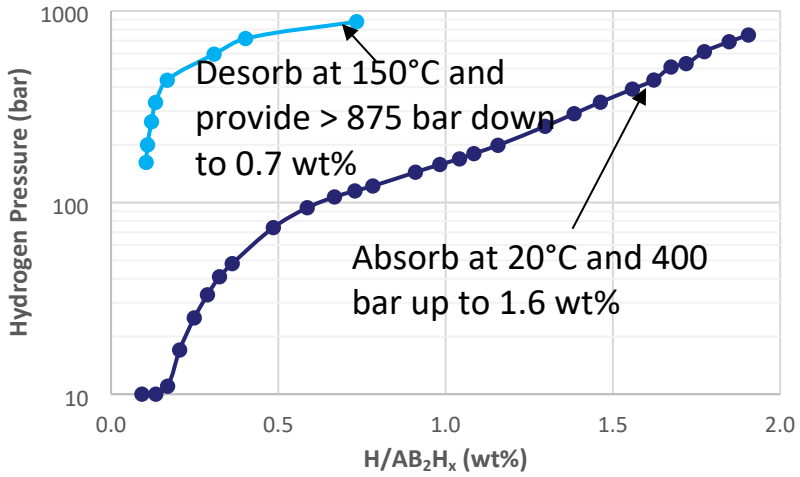


**Figure 2-13. Absorption isotherm at 20 ºC and desorption isotherm at 150 ºC for Ames #2 ($Ti_{0.8}Zr_{0.2}Fe_{1.6}V_{0.4}$).**

# 3. SYSTEM-LEVEL DESIGN AND ANALYSIS

## 3.1. System dynamic model

In parallel with the MH selection and characterization effort, a system-level dynamic model of the compressor design was developed using Matlab products Simulink and Stateflow, as shown in Figure 3-1**Error! Reference source not found.**. The objective of this modeling effort was to demonstrate the performance of the proposed design through simulation. The initial design of the prototype compressor targeted a hydrogen flow rate of 1 kg/hr from a two-stage compressor with two beds per stage. The model included heat and mass flow calculations for the two-stage compressor configuration using metal hydride properties (thermal, thermodynamic and kinetics) from literature. The model allowed for time-dependent simulations to determine appropriate cycle times and staging to achieve quasi-continuous hydrogen compression. The model was used to predict baseline performance based on an initial set of LP and HP hydrides and conceptual bed designs.

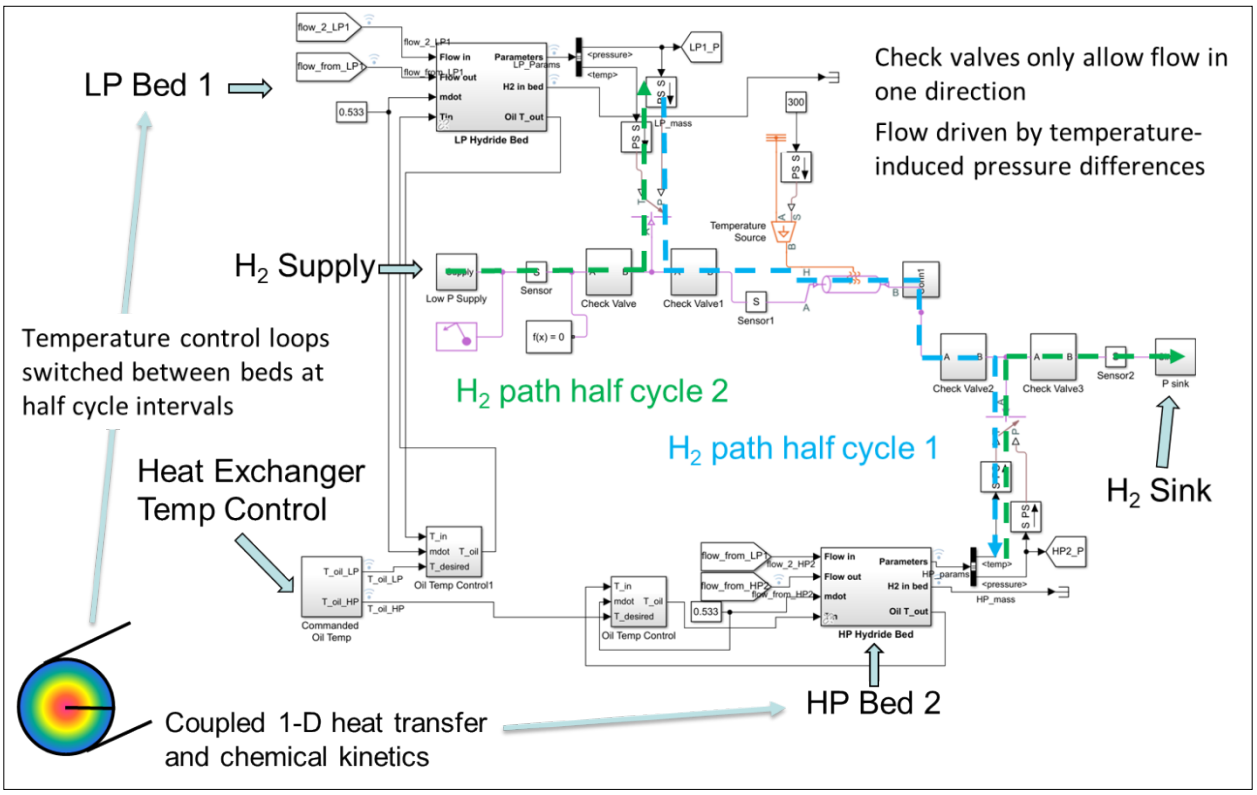


**Figure 3-1. Simulink model of two-stage MH Compressor.**

Initial simulations with the model used the LP and HP hydrides shown in Figure 3-2**Error! Reference source not found.**. Each bed was simulated with 25 kg of each Ti-based $AB_2$ alloy. Hydride properties are taken from the Purdue University Metal Hydride Toolbox [18], and include thermodynamics, kinetics and thermal material properties.

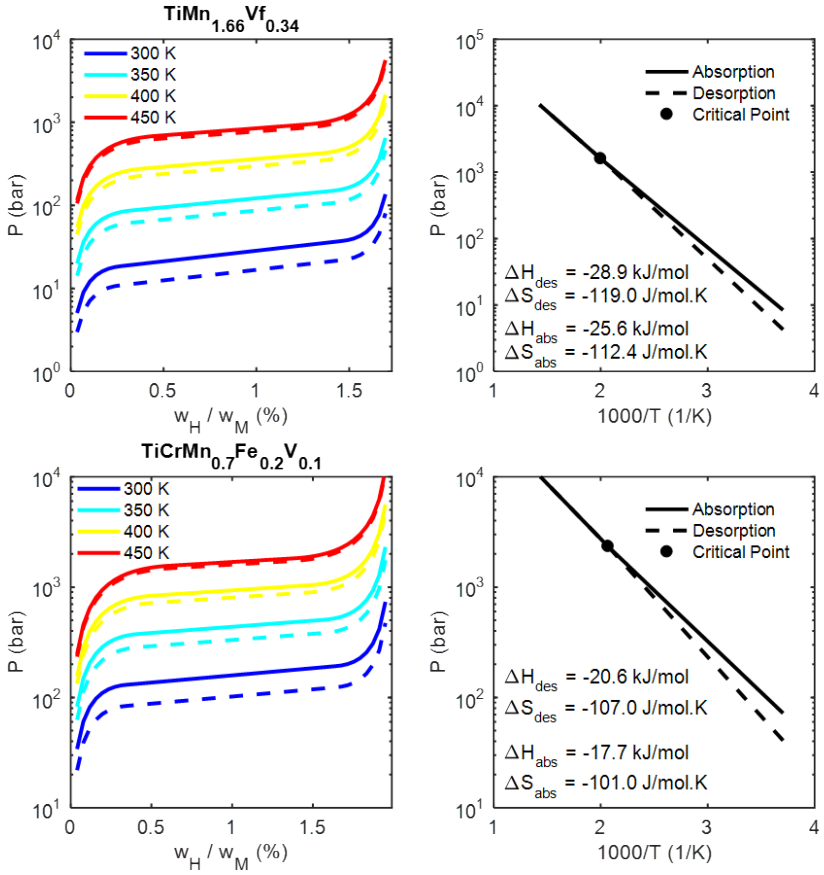


**Figure 3-2. Baseline LP and HP hydride thermodynamic properties.**

Two distinct half cycles were simulated. In the first half cycle, a heated LP bed desorbs into a cooled HP bed at an intermediate pressure between 100 and 875 bar. For the purpose of the baseline simulations, the beds were heated and cooled by fluid loops controlled by recirculating heat exchangers. The hot fluid loop operated at 175°C and the cold fluid loop operated at 10°C. A synthetic heat transfer fluid circulated at 30 gpm flow rate was assumed for each loop. Pressurization and flow of hydrogen is controlled by the temperature of the beds and check valves that connect the beds with each other and the low pressure hydrogen supply and high pressure hydrogen sink. Figure 3-3**Error! Reference source not found.** shows the simulation results for the first half cycle with a 12-minute interval.

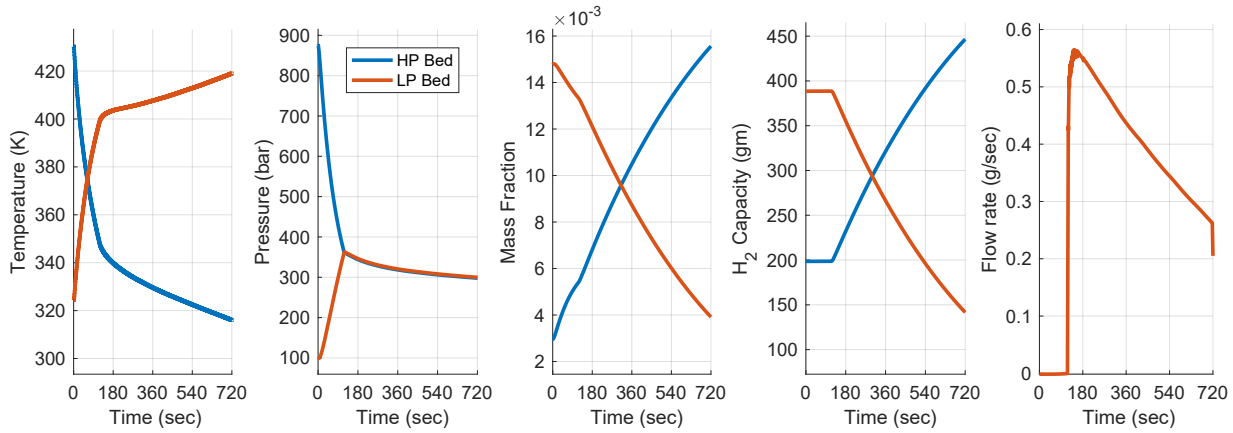


**Figure 3-3. Simulated half cycle in which a heated LP bed desorbs into a cooled HP bed.**

At the specified interval for the half cycles, the hot and cold fluid loops switch from a LP bed to a HP bed and vice versa. Thus, as the first half cycle ends, the hot LP bed has been emptied into the cooled HP bed and the fluid flow is switched. During the next half cycle, the heated HP bed delivers its hydrogen to the high pressure sink at 875 bar while the cooled LP bed is filled with hydrogen from the low-pressure supply at 100 bar. This is shown in Figure 3-4.

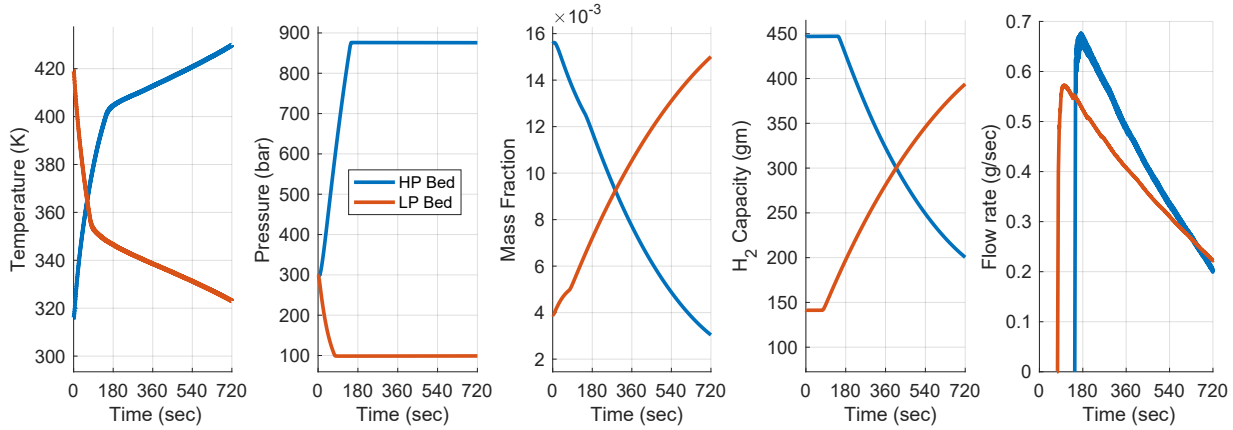


**Figure 3-4. Simulated half cycle in which a heated HP bed delivers hydrogen at 875 bar while a cooled LP bed is filled from the low pressure supply.**

Due to the symmetry of the system configuration, the results from the single bed pair can be used to estimate the performance of the full system. Figure 3-5**Error! Reference source not found.** shows the hydrogen flow rate at 875 bar produced by this baseline configuration with 12 minute half cycles. The figure shows a quasi-continuous flow over a one hour period that consists of alternating flow from each of the two HP beds. At the beginning of each 12 min interval, no flow is produced until the bed is hot enough to reach the 875 bar pressure. At that point, hydrogen flows from the bed at ~0.65 g/sec. This flow rate decreases as the bed is emptied of hydrogen. At the end of the half cycle, the bed is suddenly cooled and flow drops to zero. Simultaneously, the second HP bed is heated and the half cycles repeat. The ultimate result is ~1200 grams of hydrogen compressed from 100 bar to 875 bar in one hour or an average flow rate of 1.2 kg/hr.

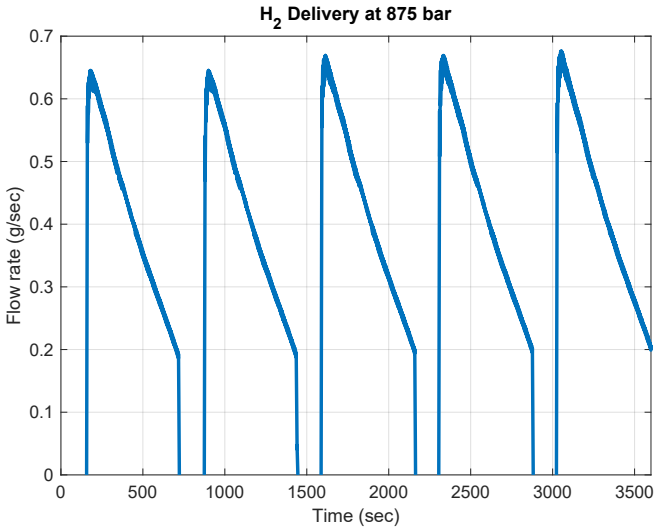


**Figure 3-5. Simulated hydrogen delivery at 875 bar from a two-stage MH compressor.**

The simulation thus demonstrated the feasibility of such a MH Compressor design using measured thermodynamic properties from real metal hydrides. The delivery flow rate of 1.2 kg/hr is directly proportional to the size of the MH beds. The 25 kg bed size used for these baseline simulations was chosen as a reasonable size for a laboratory prototype system. To achieve 100 kg/hr, as an ultimate performance goal, the beds would have to be scaled appropriately.

The system-level compressor model was then used for several design studies of different configurations to look at the effect on flow rate as well as energy consumption and bed utilization. For energy consumption, only the heat input to the system for desorption was considered in the analysis. This ignores how the heat is generated since any number of sources could be used. This is discussed in more detail in Section 3.2. Various combinations of alloys with different thermodynamic properties, cycle times, bed geometry, and supply pressure were investigated. Initially, the baseline configuration was refined which included placing a realistic limit on the heating/cooling rates as well as adjusting the mass of the high-pressure alloy based on its greater capacity. This resulted in an average flow rate of 1.07 kg/hr with a heating requirement of 12.5 kWh/kg. **Error! Reference source not found.**Table 3-1. shows this revised baseline case along with the results of seven other cases that were simulated. Two different low pressure alloys, three different cycle times, one different bed geometry, and a lower feed pressure were considered.

**Table 3-1. System-level parameter study results.**

| Configuration | LP Alloy – mass (kg) | HP Alloy – mass (kg) | Feed Pressure (bar) | Half Cycle Time (min) | Flow rate (kg/hr) | Energy (kWh/kg) |
|---|---|---|---|---|---|---|
| Baseline | $TiMn_{1.66}Vf_{0.34}$ 25 kg | $TiCrMn_{0.7}Fe_{0.2}V_{0.1}$ 21.7 kg | 100 | 12 | **1.07** | **12.5** |
| Increase cycle time | Baseline | Baseline | Baseline | 15 | **1.05** | **11.8** |
| New LP alloy | $Ti_{0.98}Zr_{0.02}V_{0.43}Fe_{0.09}Cr_{0.05}Mn_{1.5}$ - 25 kg | Baseline 24.4 kg | Baseline | Baseline | **0.995** | **13.8** |
| New LP alloy – AB5 | $MmNi_{4.6}Al_{0.4}$ 30 kg | Baseline | Baseline | Baseline | **0.45** | **23.3** |
| AB5 + cycle time | $MmNi_{4.6}Al_{0.4}$ 30 kg | Baseline | Baseline | 20 | **0.52** | **15.6** |
| AB5 + cycle time + reduced diameter | $MmNi_{4.6}Al_{0.4}$ 30 kg | Baseline | Baseline | Asymmetric 20/12 | **0.83** | **13.4** |
| AB5 + cycle time + reduced diameter + feed | $MmNi_{4.6}Al_{0.4}$ 30 kg | Baseline | 50 | Asymmetric 20/12 | **0.78** | **13.8** |
| AB2 + reduced diameter + feed | $Ti_{0.98}Zr_{0.02}V_{0.43}Fe_{0.09}Cr_{0.05}Mn_{1.5}$ - 25 kg | Baseline 24.4 kg | 50 | Baseline | **1.25** | **12.5** |

This design study revealed several insights from the system simulations. Firstly, energy efficiency can be improved with optimized cycle times, including the use of asymmetric cycle times (longer duration for desorption half cycles). Changing the low-pressure alloy from one $AB_2$ to another created a slight performance hit and changing to a lower pressure $AB_5$ alloy caused a large performance hit. However, changing to smaller tube diameter to improve heat transfer and using asymmetric half cycles allowed the $AB_5$ performance to approach that of the $AB_2$ alloys. Finally, the results showed that a 50 bar feed pressure could be used with good performance based on properties of metal hydrides from literature. In practice, experimental performance of the alloys tested differed from that found in literature, and alloys weren't identified that would achieve the target outlet pressure at an inlet pressure <150 bar.

Upon completion of the design trade study (see Section 4) and initial metal hydride characterization the system-level compressor model was updated to include measured properties of the low-pressure hydride alloy as well as the final design of the compressor beds. As will be discussed, an internal heat exchanger design provided a significant energy savings as compared to the baseline shell and tube concept. Simulations using the shell and tube configuration predicted a hydrogen flow rate of 0.86 kg/hr with an energy usage of 13.4 kWh/kg $H_2$ using the updated low-pressure alloy properties. Switching to the internal helical coil heat exchanger design increased the hydrogen flow rate to 1.2 kg/hr and reduced the energy usage to 10.3 kWh/kg $H_2$. These improvements can be attributed to the improved heat transfer and significantly decreased heat losses of this design.

The final configuration of the system dynamic model included updating the hydrides to Ames #3 and Ames #2 based on measured properties and updating the model to reflect the reduced-scale geometry of the prototype compressor. To accommodate the chosen hydride alloys two new parameter files were added to the database for Ames #2 and #3. The files were created based on the measured PCT data from GWE and ORNL. The material model parameters were selected to provide the best overall fit to the data given the limitations of the model form. The following graphs show a comparison of the thermodynamic models and the data for the two alloys. Figure 3-6**Error! Reference source not found.** shows the model that was fit to Ames #3 data. At room temperature the model shows a slightly higher plateau slope than the data and lower capacity. At 130 °C, the model has a lower slope and less taper at the low capacity. These differences primarily result in a conservative prediction since the actual material can be filled to higher capacity at room temperature and will produce higher pressure at high temperature down to about 0.6 wt%.

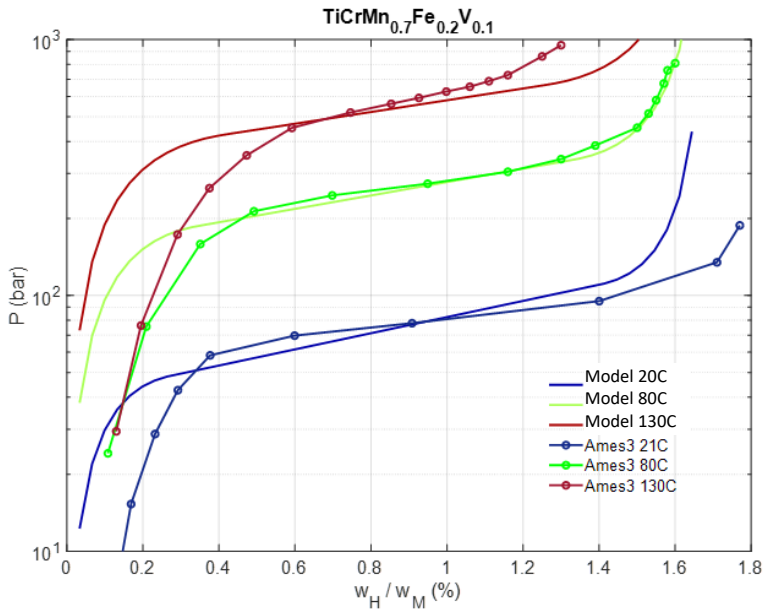


**Figure 3-6. Comparison of measured data with a material model for Ames #3.**

Figure 3-7**Error! Reference source not found.** shows the model that was fit to Ames #2 data. Overall, the thermodynamic model fits the data quite well with somewhat less tapering of pressure at capacities less than 0.4 wt%. This difference should have little impact on the system model performance predictions.

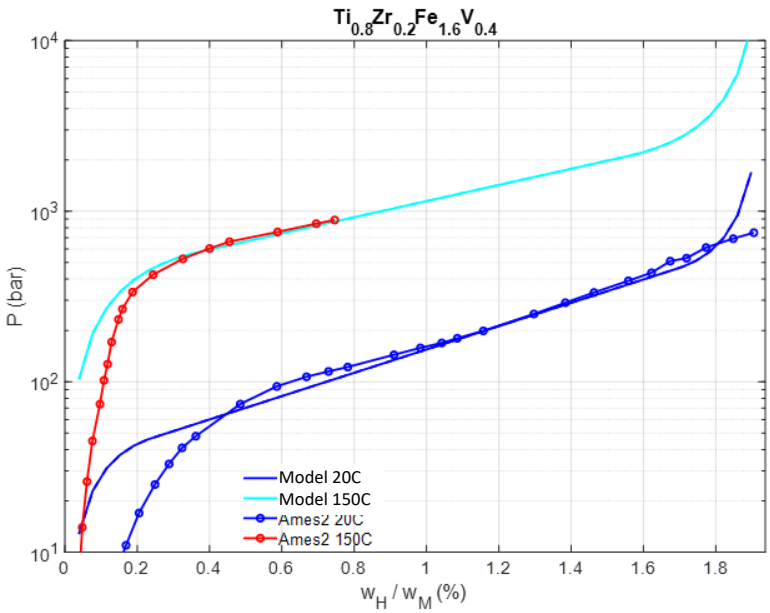


**Figure 3-7. Comparison of measured data with a material model for Ames #2.**

With these new hydride material models, the dynamic system model was run to determine the compressor performance. Given the limitations of the metal hydrides as discussed in Section **Error! Reference source not found.**, the source pressure was increased to 150 bar for 875 bar output. With 15-minute half cycles and oil recirculation loops at 20°C and 160°C, the simulation predicted utilization of 54% for all beds, 0.90 kg/hr average flow rate, and energy usage of 10.9 kWh/kg $H_2$[1].

## 3.2. Energy efficiency analysis

Several pathways for achieving energy efficiency with a metal hydride compressor design were investigated as part of the project. Waste heat sources for the metal hydride compressor were identified, but they are not likely to exist in the forecourt but at centralized hydrogen production facilities such as SMR plants and waste-to-energy systems. For example, discussions were carried out with HCATT/BESI on integration of the prototype system into the BESI waste-to-energy system in Pearl Harbor, HI or University Park, IL. The Pearl Harbor system at HCATT has 190 kW of steam at ~180 ˚C and cooling water available to couple to a metal hydride compressor requiring little additional energy.

However, with a goal of using the compressor at hydrogen stations, other configurations were investigated. Firstly, a heat recuperator design was conceptually identified that could reduce the sensible heat requirement of the system by ~40% bringing required heat down to ~10 kWh/kg for the baseline system. If this heat was provided by a natural gas burner (assuming natural gas costs $0.065/mm-btu, and burners are about 85% efficient) the operating cost would be $ 0.25/kg. This would be comparable to a conventional compressor using 2.3 kWh/kg at $0.11/kWh electricity cost.

Another option would be to couple the compressor to an energy efficient heat pump. Two heat pump options were considered: a vapor compression cycle (VCC) and an absorption heat pump (AHP) cycle. If the compressor heat was provided by a VCC system then the electrical energy requirement would

[1] This is only kWh-thermal

be (10kWh/kg)/COP_heat where COP_heat is the heating coefficient of performance of the heat pump. One possibility for a good working fluid for the refrigerant that works over the temperature range that we need is R21. A simple analysis of an ideal heat pump cycle shows that a VCC with R21 operating between 25 and 125 °C has a COP_heat of 2.7. That would result in a compressor energy requirement of 10/2.7 = 3.7 kWh/kg. Another possible VCC working fluid might be methanol. A VCC system with methanol could operate between 25 and 125 °C with a COP_heat of 3.2. This would give an energy efficiency of 3.1 kWh/kg. With compressor cooling it's possible these COP values could be improved somewhat.

For AHP cycles there is the possibility of driving the cycle with heat rather than electricity. This is favorable because it's less expensive to provide heat than electricity. So, a natural gas-fired AHP system might be advantageous. However, an AHP cycle operating over this temperature lift is not likely to produce a COP of > 1.4. At a COP of 1.4, the heat required for the compressor would be 7.1 kWh/kg. If this heat was provided by burning natural gas, then the cost would be $0.18/kg.

To further explore energy efficiency scenarios, several simulations were run using the properties of Hydralloy C5 for the low pressure alloy and the properties of $Ti_{0.95}Zr_{0.05}Cr_{1.20}Mn_{0.75}V_{0.05}$ for the high pressure alloy. Different operating parameters were tested to find the best combination to produce a reasonable hydrogen flow rate with high energy efficiency for these materials. Because of the thermodynamics of the high pressure alloy, the heating and cooling loop temperatures were shifted to higher temperatures than previous simulations. With a heating loop operating at 190 °C and a cooling loop at 60 °C, the simulated compressor could produce a hydrogen flow rate of 0.88 kg/hr with an energy efficiency of 10.7 kWh/kg under 100-875 bar operation. This is a slightly lower flow rate than the 1.0 kg/hr target, but the flow rate could be met with slightly larger beds with no decrease in efficiency. To achieve a target of 4.0 kWh/kg, the COP of the heat pump would need to be 2.675 over the temperature range of 60 °C to 190 °C. The COP of a heat pump is defined as the heat transferred from the condenser divided by the mechanical work of the heat pump compressor.

A simple thermodynamic analysis can be performed to calculate the theoretical COP of a heat pump given the condenser and evaporator temperatures and a candidate refrigerant. As mentioned previously, methanol has potentially attractive thermodynamics for this application. Figure 3-8**Error! Reference source not found.** shows the P-h and T-s diagrams for methanol along with traces representing a theoretical VCC cycle that could be used to pump heat between the low and high temperature compressor beds. The evaporator would operate at 60 °C and 12 psia while the condenser would operate at 190 °C and 482 psia. An idealized cycle assumes isenthalpic expansion of the saturated liquid and isentropic compression of the saturated vapor. With this basic cycle, the COP is calculated as COP = (h2-h3)/h2-1). For methanol at these conditions, the COP is 2.63. Note that this is very close to the required value of 2.675 and gives an energy consumption of 4.06 kWh/kg for the overall system.

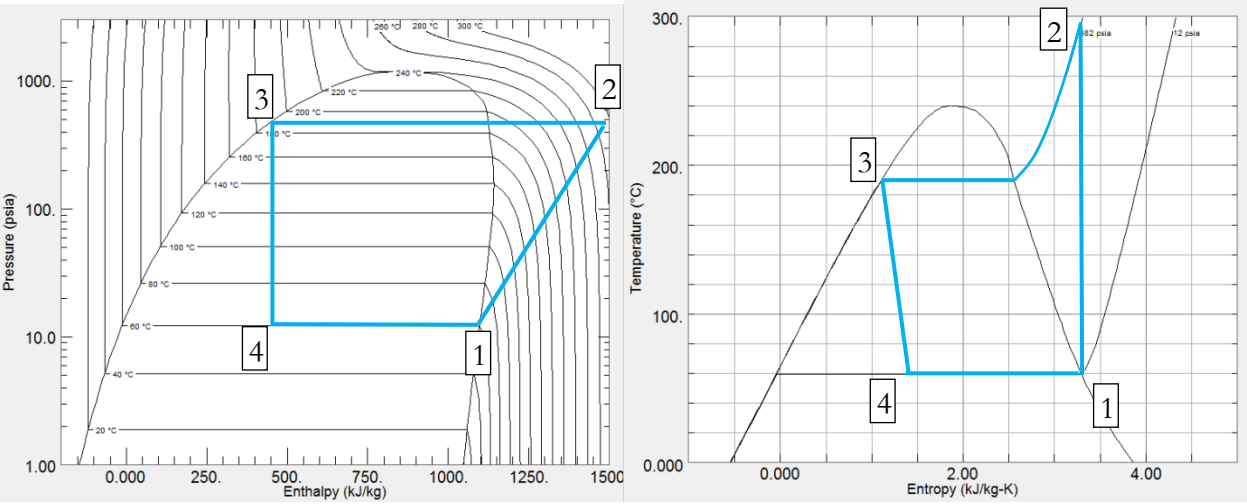


**Figure 3-8. P-h and T-s diagrams for methanol showing a theoretical heat pump cycle.**

There are several caveats to the preceding analysis, however. Firstly, the simple cycle assumes that the compressor has 100% isentropic efficiency with a compression ratio of 39.2, which is unattainable. While this heat pump would likely require a custom compressor design, the isentropic efficiency is likely to be lower than 70% and multiple stages would be required to achieve the high compression ratio. With 70% isentropic efficiency, the COP drops to 2.14 resulting in an energy consumption of 5.0 kWh/kg. In addition, methanol may not be a practical refrigerant. One issue is that the evaporator pressure is sub-ambient which is undesirable for compressor design.

Many other fluids exist or are being developed that may have greater potential for a high temperature heat pump than methanol, but developing a working VCC heat pump design with such a fluid is beyond the scope of this project. However, research into high temperature heat pumps has shown some promising recent developments. According to a review presentation at the recent European Heat Pump Summit [19], there is burgeoning interest in developing high temperature heat pumps (HTHP, 100-140 °C supply) and very high temperature heat pumps (VHTHP, up to 160 °C supply) to provide process heat for a number of processes in various industries including chemical, pharmaceutical, mineral, food and beverage, metal and paper. Heat pumps would serve as clean energy replacements for fossil fuel steam boilers in these industries.

There are a number of commercially available HTHPs on the market, including units produced by Ochsner, Hybrid Energy, Mayekawa, and Durr Thermea with supply temperatures from 110°C to 130°C. Figure 3-9**Error! Reference source not found.** (borrowed from [19]) shows COP as a function of temperature lift for a number of these systems based on a supply temperature of 140°C. Note that the efficiency of these systems is pushing toward 60% of the Carnot limit with one case showing greater than 60% Carnot efficiency. It might be expected that as this technology matures, higher efficiencies may be possible. There is also development of new refrigerants for HTHPs including several fluids developed by DuPont with very low global warming potential (GWP) that are non-flammable. One such fluid is R1336mzz-Z which has a critical temperature of over 170°C making it a promising working fluid for VHTHPs.

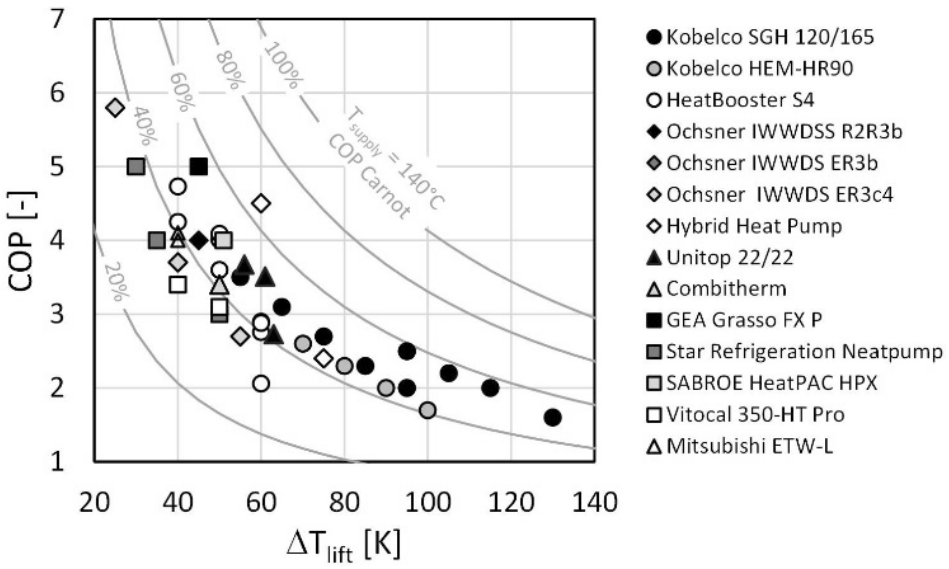


**Figure 3-9. COP vs. temperature lift for various commercial HTHPs (borrowed from [19]).**

VHTHP development is primarily at a low TRL level currently, but a significant amount of R&D is being carried out to develop these systems. Also, at least one commercial VHTHP exists. The Viking Heat Engines HeatBooster is a VHTHP that can supply up to 160 °C operating with R1335mzz-Z. Figure 3-10**Error! Reference source not found.** shows the performance of the HeatBooster based on Viking literature.

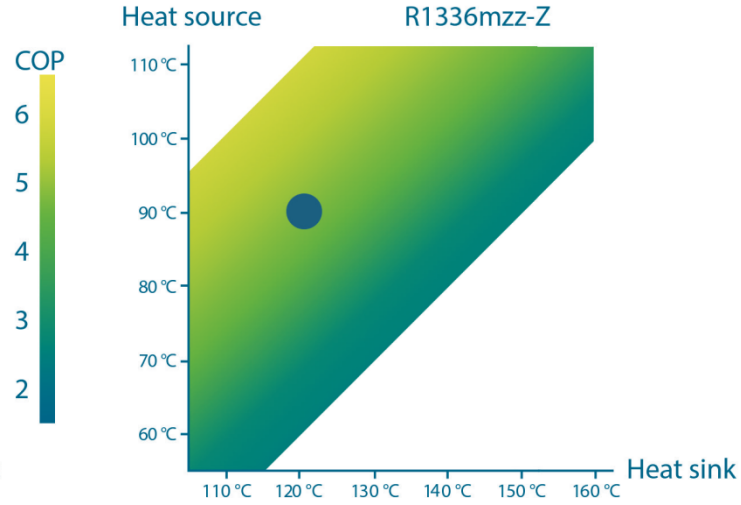


**Figure 3-10. Performance of the Viking Heat Engines HeatBooster VHTHP. The blue dot shows that a 90°C heat source and 120°C heat sink result in a COP of 5.**

While these results don't point to a VHTHP that can achieve a temperature lift from 60°C to 190°C with a COP greater than 2.675, they do show potential for this COP with a comparable lift. For example, an approach using a cascade heat pump system with two loops using different working fluids

might reach this target. For a cascade system, the net COP can be calculated based on the COPs of the individual cycles. The equation can be reduced to COP_tot = COP1*COP2/(COP1+COP2-1) where COP1 is the lower temperature cycle. A net COP of 2.675 can then be achieved with individual COPs of 4.79, for instance. Based on information in [19], Kobelco makes an HTHP that has a temperature lift from 35°C to 90°C with a COP of 5.8. If this was combined with a VHTHP with a temperature lift from 85°C to 135°C with a COP of 4.1, a net COP of 2.675 would be achieved with a net temperature lift of 100°C. The HeatBooster performance seems to be approaching this value based on **Error! Reference source not found.**Figure 3-10.

So, while it can't be shown conclusively that 4.0 kWh/kg can be achieved with a metal hydride compressor coupled to a VHTHP system, it appears that the value could be approached. Additionally, further investigation and/or research into better performing metal hydride alloys than considered here could result in lower temperature operation requiring a lower temperature lift from the heat pump and thus better energy efficiency.

# 4. COMPRESSOR BED DESIGN, FABRICATION AND ASSEMBLY

## 4.1. Design Trade Study

An extensive trade study was carried out for the compressor bed designs to determine the best design for each stage. Configurations considered include a shell and tube design with external heat exchange, a closed-ended vessel with internal heat exchange, and an open-ended vessel with internal heat exchange. Due to the more difficult requirements, the trade study focused on designs for the HP hydride beds and models for each concept were generated for comparison of manufacturability, thermal performance (kWh/kg), and mass and volume of the system. A down selection was made to a single design for both LP and HP compressor beds with the greatest potential to maximize heat transfer, minimize energy consumption, and meet the target pressure range. Scalability of the design and cost for high volume manufacturing were also considered.

The baseline concept for the compressor beds was the shell and tube design illustrated in Figure 4-1. In this design, the hydride is packed into tubular stainless-steel pressure vessels which are arranged in a staggered array in the shell and tube heat exchanger. Multiple baffles within the heat exchanger shell route the path of the heat transfer fluid across the tube bundle, maximizing heat transfer. A benefit of this design is that it is relatively easy to fabricate and assemble. Loading the hydride is enabled with removable end caps. A hydrogen distribution manifold constructed from high pressure tubing and fittings is then attached.

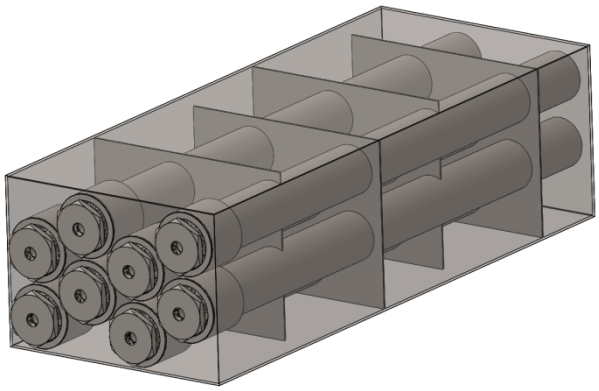

**Figure 4-1. Shell and tube configuration.**

Energy efficiency is the primary challenge for the shell and tube design for the compressor application. Because the tubes must be designed to contain high pressure, they must have thick walls which makes them relatively massive. While system mass is not a primary design consideration for the compressor, the energy required to heat and cool the system is important. Since heat is transferred to and from the metal hydride through the tube walls, the tubes are heated and cooled every half cycle of the compressor. The energy required to do so is a significant fraction of the total energy required to compress the hydrogen in this heat driven compressor. Using a high strength stainless steel alloy can minimize this energy burden, but analysis showed that it would still account for ~36% of the total energy used. Based on this assessment, the shell and tube configuration was abandoned.

Two options were considered in the trade study for an internal heat exchanger design: a closed ended vessel and an open-ended vessel. The closed ended design is shown in the upper left of Figure 4-2. This is a Type III vessel with a carbon fiber composite outer wall surrounding a metal shell containing

the metal hydride and heat exchanger. A metal end boss acts as the hydrogen inlet and outlet as well as the heat exchanger manifold. Initial analysis of the closed ended design demonstrated good energy efficiency due to the minimal mass of this design. However, further design work revealed that it was not feasible to load this option with metal hydride in a way that would achieve the required thermal conductivity. This led to an investigation of the open ended design option.

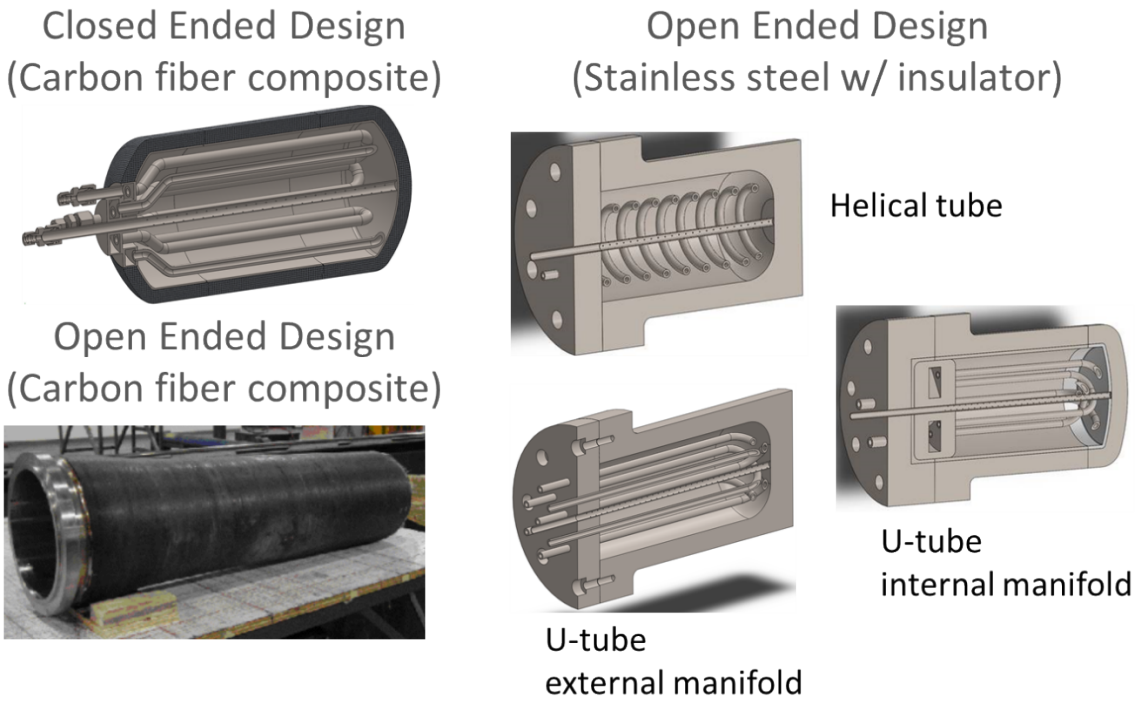


**Figure 4-2. Internal heat exchanger design options.**

For the open-ended design, several variants were analyzed as illustrated in Figure 4-2. For this design, the advantage of a carbon fiber composite pressure vessel, like that shown in the lower left image of Figure 4-2, is to minimize mass and thereby minimize energy usage. However, the disadvantages of using carbon fiber composite are high cost and manufacturability in commercial quantities. To circumvent these issues, an open ended design using a more standard metal pressure vessel was developed. The key to this design, shown with three options for the internal heat exchanger in Figure 4-2, is to insulate the heat exchanger and metal hydride from the pressure vessel using an insulating sleeve. Thermal analysis of this design option, depicted in Figure 4-3, demonstrated that heat loss to the vessel could be limited to a few percent of the total energy input using a closed cell foam insulation.

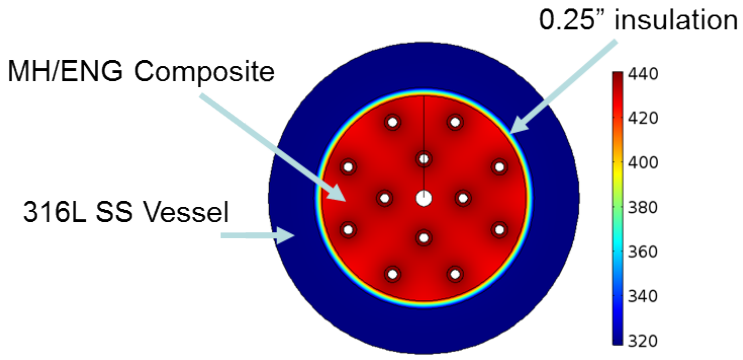


**Figure 4-3. Temperature profile of the internal heat exchanger design from a transient COMSOL model shows the efficacy of the insulating sleeve.**

The three different heat exchanger configurations for the open-ended design were developed to address competing requirements of the design including ease of loading the MH, minimizing high pressure seals, providing temperature uniformity, and addressing an unbalanced pressure load. The two U-tube designs both consist of the arrangement of twelve heat exchanger tubes shown in Figure 4-3. Pairs of tubes are connected with a U-shaped bend at the closed end of the vessel so that the inlet and return manifolds are at the open end. The difference between the two designs is the location of the manifolds. For the external manifold variant, all twelve tubes penetrate through the pressure vessel lid and the six inlets and six outlets are manifolded outside of the pressure vessel. One benefit of this design is the ease of loading and compacting the metal hydride. Another benefit is that the manifolds for the heat transfer fluid only need to be designed for the relatively low fluid pressure. The detriment of this design are the twelve high pressure seals required, the heat loss to the lid, and a large unbalanced pressure load on the tubing. This load with 900 bar internal pressure is over 30,000 lbf.

With the internal manifold, only a single inlet and outlet tube must penetrate the lid. This minimizes the high pressure seals and the heat loss to the lid. The challenge with this design is that the fluid manifold must now withstand up to 900 bar pressure. To meet this requirement, the manifold must be quite massive to meet allowable stress limits as shown in Figure 4-4. Heating and cooling this mass of stainless steel with every half cycle reduces the energy efficiency of this design. Another risk is that the manifold must be welded in place in an inert environment after the metal hydride is loaded. This complicates the design and fabrication procedure and risks contamination or thermal damage to the metal hydride.

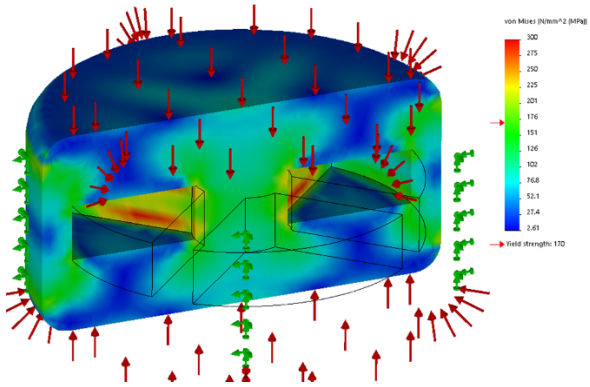

**Figure 4-4. von Mises stress in the internal manifold subjected to 900 bar external pressure.**

The final variant of the open ended internal heat exchanger design from Figure 4-2 is the helical tube design. With this version there is only one heat exchanger tube that enters through the pressure vessel lid, spirals through the metal hydride and returns along the vessel axis to exit through the lid. The helical shape of the tube provides optimal heat transfer distribution within the vessel and requires no manifolds, external or internal. Due to this fact, this heat exchanger design provides the lowest energy burden of the three options. This design is not without its challenges though. The single tube results in a significantly higher pressure drop for the heat transfer fluid. Additionally, a method for loading the vessel with metal hydride in and around the helical tube to the required packing density is required.

Table 4-1 summarizes a comparison of the design options being considered. As the table shows, each design has potential risks or issues. While easy to load and with good thermal management and pressure drop capabilities, the largest risk with the shell and tube design is the energy efficiency preventing it from meeting the Go/No-Go criteria for the project. As previously discussed, while good thermal management and energy efficiency could be achieved, the closed-ended composite vessel is potentially impossible to load with the density of MH required for good heat transfer. The three open-ended internal heat exchanger designs have good energy efficiency with the helical tube design achieving the highest value. The two u-tube designs achieve good thermal management and an obvious path for hydride loading, but several risks are associated with either the internal or external manifold designs. Given the thermal management advantage and the elimination of heat exchanger manifolds, the helical tube design was determined to be the most promising. The one downside of this design is the potentially high fluid-side pressure drop. However, it was determined that this risk could be mitigated with the proper design.

**Table 4-1. Summary of Trade Study Results**

| | **External Heat Exchange** | **Internal Heat Exchange** | | | |
|---|---|---|---|---|---|
| | Shell and Tube | Carbon Fiber Composite | External Manifold | Internal Manifold | Helical Coil |
| Energy Efficiency | | | | | |
| Manufacturability | | | | | |
| Hydride Loading | | | | | |
| Thermal Design | | | | | |
| HTF Pressure Drop | | | | | |
| Low Cost | | | | | |

## 4.2. Detailed Compressor Bed Design

The final helical tube design for the prototype compressor is depicted in Figure 4-5 and consists of a single heat exchanger tube that enters through the pressure vessel lid, spirals through the metal hydride and exits through the vessel bottom. The helical shape of the tube provides optimal heat transfer distribution within the vessel and requires no manifolds, external or internal. Due to this fact, this heat exchanger design provides the lowest energy burden of the options considered. In addition to the helical tube, the cross-sectional view in Figure 4-5 shows the hydrogen inlet/outlet at the vessel bottom with a hydrogen distribution tube running the length of the vessel. A Teflon liner, also shown

in Figure 4-5, surrounds the helical tube and metal hydride to thermally insulate the hydride from the vessel, improving energy efficiency. The vessel lid and seal consists of a two-piece design with the T-shaped piece providing the seal with a polymer or metal gasket and the large annular threaded nut providing the force to hold the seal in place. This is a standard design for suppliers of high-pressure reactors such as HiP and Parker/Autoclave, for example.

It was decided that the proof-of-concept compressor prototype would be demonstrated with one bed per stage. This would not allow for the quasi-continuous flow of hydrogen from the compressor and would cut the flow rate in half but would allow for the demonstration of all other aspects of the system. Additionally, instead of the 1 kg/hr flow rate targeted in the system-level model, the prototype beds were designed to contain 3 kg of metal hydride, targeting a hydrogen flow rate of 0.12 kg/hr to reduce the cost of the prototype significantly and still maintain all of the key design aspects.

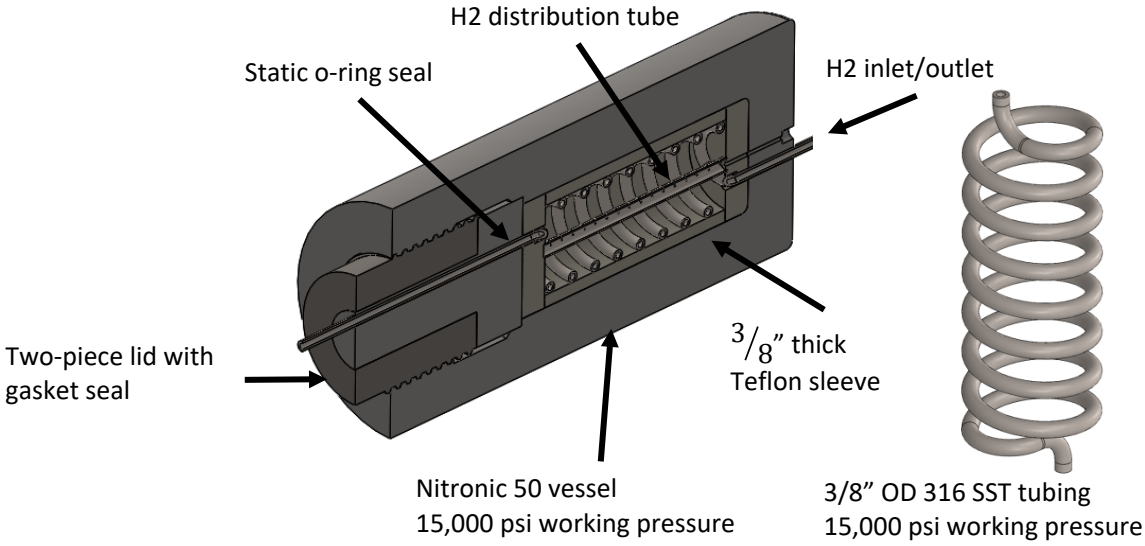


**Figure 4-5. Final helical tube design for the prototype compressor.**

### *4.2.1. Modeling and Analysis*

The compressor bed design focused on balancing energy efficiency and manufacturability with metal hydride capacity by studying the impact of internal bed dimensions, helical coil design, and Teflon liner thickness. Modeling and analysis was completed using a spreadsheet energy balance analysis paired with a COMSOL Multiphysics model of the compressor bed that included coupled heat transfer and chemical kinetics of the metal hydrides.

The COMSOL model geometry is shown in Figure 4-6**Error! Reference source not found.**. Half of the bed geometry was modelled with a symmetry boundary condition. The end of the vessel and lid assembly were not included for simplicity. However, separate models of these vessel sections were used for energy efficiency estimates of the final design.

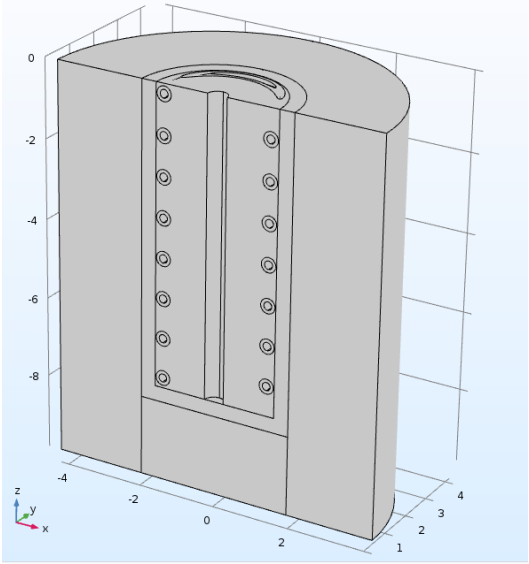


**Figure 4-6. COMSOL geometry.**

Rather than solve the conjugate heat transfer problem for the helical coil heat exchanger within the COMSOL model, the energy balance spreadsheet analysis included calculation of the fluid-side heat transfer coefficient (HTC) for flow through helical coils using Nusselt number correlations. The spreadsheet also included pressure drop calculations through the helical coil heat exchanger based on empirical correlations from literature. Each of these parameters were calculated for the various heat transfer fluids that were considered including Xceltherm 600, Syltherm 800, Xceltherm SST, Dowtherm G, and Paratherm MR. Thermophysical properties as a function of temperature of the fluids were input into the pressure drop and HTC correlations and the energy balance analysis was used to calculate the temperature drop through the helical coil. This was used to calculate an average fluid temperature and heat transfer coefficient for use in the COMSOL model. This was an iterative process with the COMSOL model as follows:

1. Calculate the inlet HTC
    a) Calculate inlet fluid properties based on prescribed inlet temperature and the selected heat transfer fluid (HTF).
    a) Assume a mass flow rate for the heat transfer fluid. Calculate pressure drop through the helical coil and adjust mass flow rate based on pump curves.
    b) With adjusted mass flow rate, calculate Reynolds number (Re) and Prandtl number (Pr) based on tubing diameter, flow rate, and HTF properties.
    c) Confirm turbulent flow and calculate Nusselt number (Nu).
    d) Calculate HTC for the inlet.
2. Calculate the outlet HTC
    a) Calculate $T_{outlet}$ based on $Q = \dot{m}c_p\Delta T$ where $c_p$ is HTF specific heat and Q is determined from the COMSOL model heat transfer analysis.
    a) Calculate outlet fluid properties based on $T_{outlet.}$
    b) Calculate Re and Pr.
    c) Confirm turbulent flow and calculate Nu.
    d) Calculate HTC for the outlet.
3. Calculate the average HTC
    a) Calculate $T_{ave}$ and average fluid properties

b) Calculate Re and Pr
c) Calculate Nu.
d) Calculate average HTC.

The average HTC was then used in the COMSOL model to calculate temperature gradients throughout the MH, volume averaged hydrogen concentration, and the total energy into the system from the heat transfer fluid. Metal hydride sorption rates are a function of the local temperature and hydrogen pressure. In a large-scale cylindrical vessel, the local temperature and pressure are functions of both axial and radial position which must be calculated using energy and mass balances that depend generally on heat and mass transport properties of the metal hydride. Here, hydrogen mass transport was neglected. Instead, a uniform hydrogen pressure was applied to the bed and the model calculated local temperature and MH species concentration. The hydrogenation (dehydrogenation) reactions contribute heat source (sink) terms to the energy balance. So, design of the compressor beds required a chemical kinetics model of the MH coupled with heat transport equations. Initial modeling used the properties of Hydralloy C5 to optimize the design. Since the standard entropy and enthalpy of hydride formation of titanium based $AB_2$ metal hydrides are similar, the resulting optimized design was assumed to apply to the final metal hydrides (Lototskyy).

Conservation of energy solved by the COMSOL model for the MH beds is given by Equation 1.

$$\rho c_p \frac{\partial T}{\partial t} = \nabla \cdot (k \nabla T) + R \Delta H \quad \textbf{(1)}$$

Here $\rho$, $c_p$ and k are the density, specific heat capacity, and effective thermal conductivity of the MH. The hydride material temperature, T, is assumed to be in thermal equilibrium with the gas temperature. The left-hand term in Equation 1 is the rate of change of temperature of the MH. Hydrogen advection is neglected in the model. The first term on the right-hand side accounts for heat conduction through the solid, where an effective conductivity of the hydride bed is used (see below for more detail). The second term on the right accounts for the chemical reaction rate, R, between the hydride and gas phase, which can be either exothermic (hydrogenation) or endothermic (dehydrogenation), where $\Delta H$ is the enthalpy of reaction. For Hydralloy C5 the absorption enthalpy is 19.5 kJ/mol while the desorption enthalpy is 24.6 kJ/mol. The solution to the energy equation relies on a convective boundary condition at the surface of the helical coil heat exchanger that is based on the heat transfer coefficient calculated from the spreadsheet analysis. The heat flux on the helical tubing is shown in Equation 2. See 4.2.7 for additional information on the heat transfer coefficient.

$$q\,(T, t) = h(t)(T_{ext}(t) - T)\ , \mathrm{W/m^2} \quad \textbf{(2)}$$

Where

h = heat transfer coefficient = $\begin{cases} h_{heating}, t \leq 900) \\ h_{cooling}, \text{otherwise} \end{cases}$

$T_{ext}$ = fluid temperature = $\begin{cases} T_{heating}, t \leq 900) \\ T_{cooling}, \text{otherwise} \end{cases}$

Species conservation for the MH is given by:

$$\frac{\partial c}{\partial t} = R \quad \textbf{(3)}$$

Where c is the MH hydrogen concentration in mol/m$^3$. The MH production rate, R, is given by the reaction rate according to the hydrogenation reaction M + ½ $H_2$ = MH. The conservation equation relies on the solution to the chemical rate equation. A chemical kinetics model was developed to provide this solution. The reaction rate equations for desorption and absorption are shown in Equation 4 and 5, respectively,

$$\mathrm{R_d\ (T, t, c) = C_d exp\left[-\frac{E_d}{RT}\right] ln\left[\frac{P(t) - P_{eq}\ (T)}{P_{eq}\ (T)}\right][C_i - C]},\ \mathrm{mol/m^3\text{-}s} \quad \textbf{(4)}$$

$$\mathrm{R_a\ (T, t, c) = C_a exp\left[-\frac{E_a}{RT}\right] ln\left[\frac{P(t)}{P_{eq}\ (T)}\right][C_i - C]},\ \mathrm{mol/m^3\text{-}s} \quad \textbf{(5)}$$

where

$C_d$ = 5000 s$^{-1}$, reaction constant for desorption
$C_a$ = 190 s$^{-1}$, reaction constant for absorption
$E_d$ = activation energy for desorption, J/mol
$E_a$ = activation energy for absorption, J/mol
R = universal gas constant, J/mol-K
T = temperature, K
P(t) = pressure profile shown in Figure 4-7
$P_{eq}(T)$ = equilibrium pressure, Pa
$C_i$ = 34325 mol/m$^3$, initial H2 concentration

In the above equations the equilibrium pressures $P_{eq}$ are modeled with Arrhenius expressions. The expressions for the equilibrium pressures of Hydralloy C5 are shown below in Equations 6 - 8.

$$P_{eq}(Abs) = \begin{cases} 101325 * \exp\left(-\frac{2653\ [K]}{T} + 11.727\right), & \text{if } T < \left(\frac{305}{0.782}\right) \\ P_{eq}(T), & \text{otherwise} \end{cases} \quad \textbf{(6)}$$

$$P_{eq}(Des) = \begin{cases} 101325 * \exp\left(-\frac{2348\ [K]}{T} + 10.945\right), & \text{if } T < \left(\frac{305}{0.782}\right) \\ P_{eq}(T), & \text{otherwise} \end{cases} \quad \textbf{(7)}$$

$$P_{eq}(T) = 101325 * \exp\left(-\frac{2500.5\ [K]}{T} + 11.336\right) \quad \textbf{(8)}$$

Simulations with the COMSOL model were run with the metal hydride fully absorbed as the initial condition. This is specified by the initial concentration of hydrogen in the MH bed. The model would then simulate a 15-minute desorption process followed by a 15-minute absorption process. As described above, a uniform hydrogen pressure was applied to the model. The imposed pressure curve P(t) shown in Figure 4-7 was based on the System dynamic model (see Section 3.1).

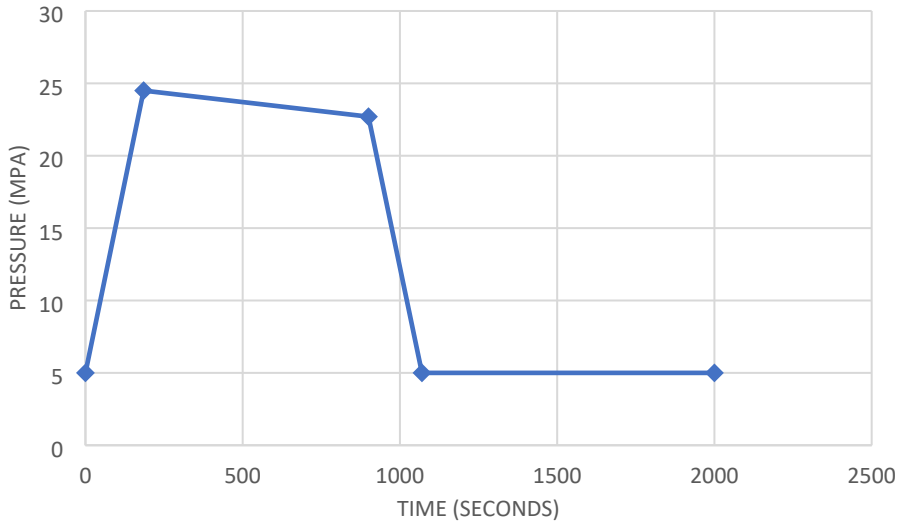


**Figure 4-7. Imposed pressure profile P(t) based on system dynamic model.**

The simulation results included the transient metal hydride temperature field and hydrogen concentration. Integration of the hydrogen concentration was used to calculate the amount of hydrogen absorbed and desorbed during the cycle. The total heat into the system was calculated two ways and compared to make sure the values agreed. First, the heat into the system through the helical coil tubing from the heat transfer fluid was integrated. This was then compared to the sum of the sensible heating from the tubing, the sensible heating from the metal hydride, the heat generated in the metal hydride, and the heat lost through the outer vessel wall. The total energy input into the system was compared to the value used in the energy balance analysis and the solutions were iterated until they converged.

This process was used to optimize the design of the compressor beds. The vessel optimization considered pressure vessels with 5" ID and 4" ID with lengths adjusted to maintain 3 kg of metal hydride. The helical coil design varied pitch, inner tube diameter, and design (with or without a tube through the center). The Teflon liner thickness was varied to accommodate both the helical coil and the vessel dimensions. An example of a few of the designs considered is shown in Figure 4-8.

| Design | 2 | 6 | 3a | 3b | 4 |
|---|---|---|---|---|---|
| Tube OD | 0.5” | 0.375” | 0.5” | 0.5” | 0.375” |
| Helix height | 6” | 6” | 6” | 12” | 12” |
| Tube length | 70” | 69” | 52” | 64” | 67” |
| Helix mass | 1.5 kg | 0.8 kg | 1 kg | 1.3 kg | 0.8 kg |
| Pressure drop (cooling) | 22 psi | 22 psi | 17 psi | 18 psi | 21 psi |
| Mass flow rate | 0.15 kg/s | 0.06 kg/s | 0.15 kg/s | 0.14 kg/s | 0.06 kg/s |
| Volumetric flow rate | 11 l/min | 4.2 l/min | 11 l/min | 10 l/min | 4.2 l/min |
| HTC, cooling | 1211 W/m2K | 1040 W/m2K | 1265 W/m2K | 1194 W/m2K | ~1200 W/m2K |
| HIP vessel | 5” ID, 6” long | 5” ID, 6” long | 4” ID, 6” long | 4” ID, 12” long | 4” ID, 12” long |
| Helix diameter | 3.75”, 1” pitch | 3.625”, 1” pitch | 2.75”, 1” pitch | 2.75”, 1.5” pitch | 2.625”, 1.5” pitch |
| MH mass | 3.0 kg | 3.0 kg | 3.0 kg | 3.0 kg | 3.0 kg |
| HTC, heating | 6383 W/m2K | 5405 W/m2K | 6608 W/m2K | 6236 W/m2K | 5405 W/m2K |

**Figure 4-8. COMSOL inputs.**

An example of the design outputs is shown in Figure 4-9. For all designs two key performance variables were compared - grams of $H_2$ desorbed and energy efficiency ($kWh/kg_{H2}$). Additionally, the heat transfer distance was calculated based on the furthest distance between the metal hydride and the heat transfer tubing. This metric was primarily used to predict the performance of a specific design. Generally, the lower the heat transfer distance, the more efficient the design. The images superimposed on each design in Figure 4-9 show the resulting hydrogen concentration at the end of desorption. The blue volume is completely desorbed while the red volume did not fully desorb. As designs 3a and 3b indicate, there is a balance between amount of H2 desorbed and energy efficiency as these designs still have some hydrogen remaining in the composite but have higher efficiency than other designs.

| | Design 2 | Design 6 | Design 3a | Design 3b | Design 4 |
|---|---|---|---|---|---|
| H2 rate | 48 g/15 min | 46.6 g/15min | 36 g/15 min | 38.7 g/15min | 46.4 g/15min |
| Energy efficiency | 7.1 kWh/kg | 6.4 kWh/kg | 6.9 kWh/kg | 8.1 kWh/kg | 6.9 kWh/kg |
| HT distance | 0.6875” | 0.71875” | 1.125” | 1.125” | 0.9375” |

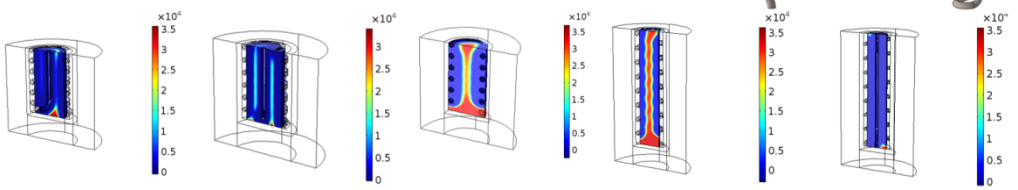

**Figure 4-9. Design outputs.**

### 4.2.2. Helical coil design

As shown in Figure 4-8 and Figure 4-9, two general designs were considered – with or without a straight section of tube through the center of the helical coil. The tube through the center would be required for a larger ID vessel to minimize the heat transfer distance and ensure efficient heat transfer. However, this design would result in unbalanced forces during pressure cycling and would require external support to oppose this force. It was decided to pursue a design without the center section of straight tube and to have the helical coil enter and exit through opposite ends of the vessel.

### 4.2.3. Helical coil tube diameter

The tubing used for the helical coil is rated to 20,000 psi. The bend radius of this medium pressure tubing is approximately 3*OD, so the 0.5" tubing has a 1.5" bend radius while the .375" tubing has a 1.125" bend radius. The bend radius was an important factor to ensure that the helix could be manufactured to exit the vessel. The smaller the OD, the easier it would be to bend into the design. However, a smaller OD also results in greater pressure drop through the system as further discussed in 4.2.7. In this design, the manufacturability concerns surpassed issues with the increased pressure drop so 0.375" OD tubing was selected.

### 4.2.4. Helix coil pitch

The helix pitch impacts the pressure drop, heat transfer, and mass of metal hydride. A study of various pitches suggested that 1.0" pitch for the .375" OD tubing optimized the energy efficiency and amount of hydrogen desorbed. Figure 4-8 and Figure 4-9 present a few of the designs considered.

### 4.2.5. Vessel ID and length

Once it was decided to not include a straight section of tube through the center, a 4" ID vessel was selected to ensure efficient heat transfer by minimizing the heat transfer distance. The length of the vessel was chosen to be 10" to enable 3 kg of material to be loaded into the vessel. This also was a common vessel design produced by HiP and was more economical than the 5" ID vessel.

### 4.2.6. Vessel seals

High pressure seals were required for each penetration through the vessel body or lid. The location of the seals for the helical coil heat exchanger impacts energy efficiency since it determines whether hydrogen or air fills the gap between the heat transfer tubing and the vessel body. The location of the seal on the bottom of the vessel was required to be on the outside due to manufacturability. However, the location of the seal in the cover of the vessel could be placed either near the surface that would face the inside of the vessel or the surface that would face the outside of the vessel. Analysis suggested that 2" of tubing surrounded by $H_2$ instead of air would result in 15% more energy lost to the cover, and so it was decided to place the seal on the inside surface as shown in Figure 4-10.

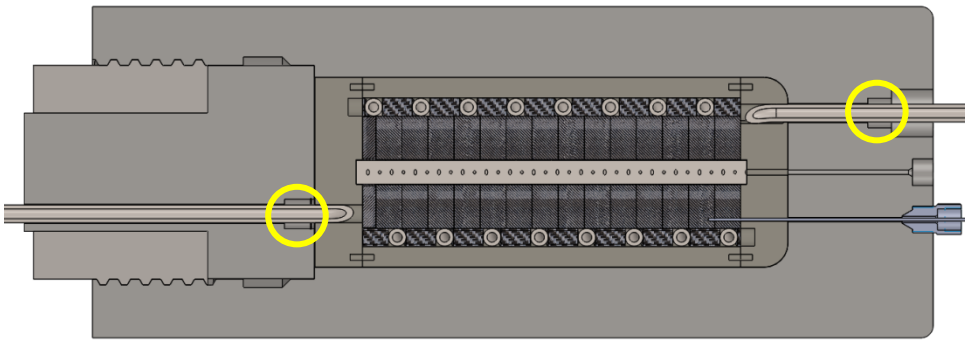

**Figure 4-10. Vessel cross-section showing seal locations**

### *4.2.7. Heat transfer fluid*

The choice of heat transfer fluid affects the heat transfer coefficient in the helical coil heat exchanger. In turn, HTC can affect the energy efficiency of the MH compressor. Several fluid properties affect HTC including thermal conductivity, heat capacity and viscosity. Viscosity affects HTC primarily through its effect on flow rate based on pressure drop. The pump sizes for the heating and cooling loops for the prototype system were fixed to pre-existing equipment, so there was a limit on how much the heat transfer coefficient could be varied in the design. However, to select the best heat transfer fluid for this application, the impact of heat transfer coefficient on compressor energy efficiency was explored.

Energy efficiency is calculated as the ratio of heat input into the system to the mass of hydrogen desorbed. This simple analysis ignores how the heat is provided to the system as this could be from any number of sources as discussed in Section 3.2. Using the COMSOL model, energy efficiency was calculated from simulations carried out over a range of HTC values from 1,000 to 10,000 $W/m^2K$. The results of this analysis are summarized in Figure 4-11. The figure shows that there is a minimum in the energy efficiency near 5,000 $W/m^2K$. This is due to a competing effect between hydrogen desorbed and heat input as a function of the heat transfer coefficient. For low heat transfer coefficients, the amount of hydrogen desorbed is limited and it dominates the equation, making the system inefficient. At high heat transfer coefficients, the amount of hydrogen desorbed begins to increase less than the amount of heat used to sensibly heat the system, so the system loses efficiency.

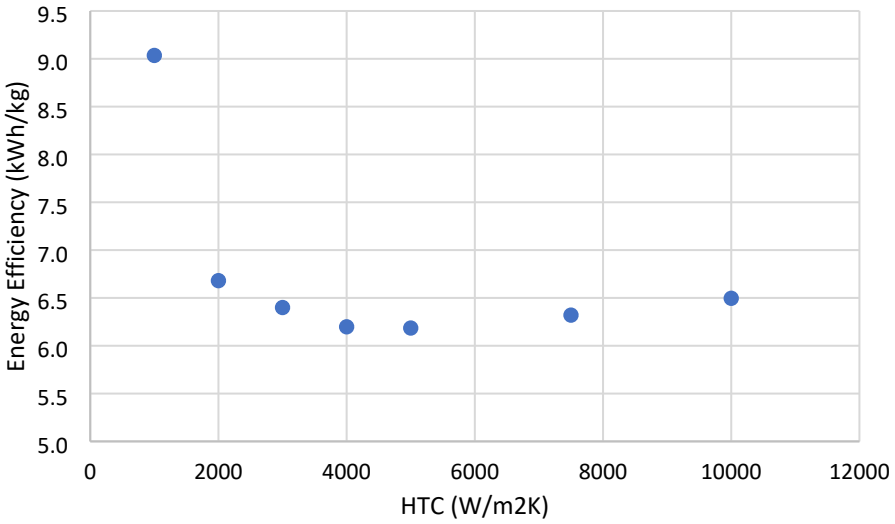


**Figure 4-11. Energy efficiency as a function of heat transfer coefficient.**

Various heat transfer fluids were considered based on the operating temperature limits for heating and the viscosity of the fluid during cooling. To estimate the pressure drop through the helical coil at various temperatures, the pressure drop was measured through a representative helical coil with water at room temperature and compared to the predictions of various published correlations as shown in Figure 4-12. Since the Ito correlation matched the measured pressure drop at low values and provided a conservative estimate at higher values, this correlation was used in further analysis.

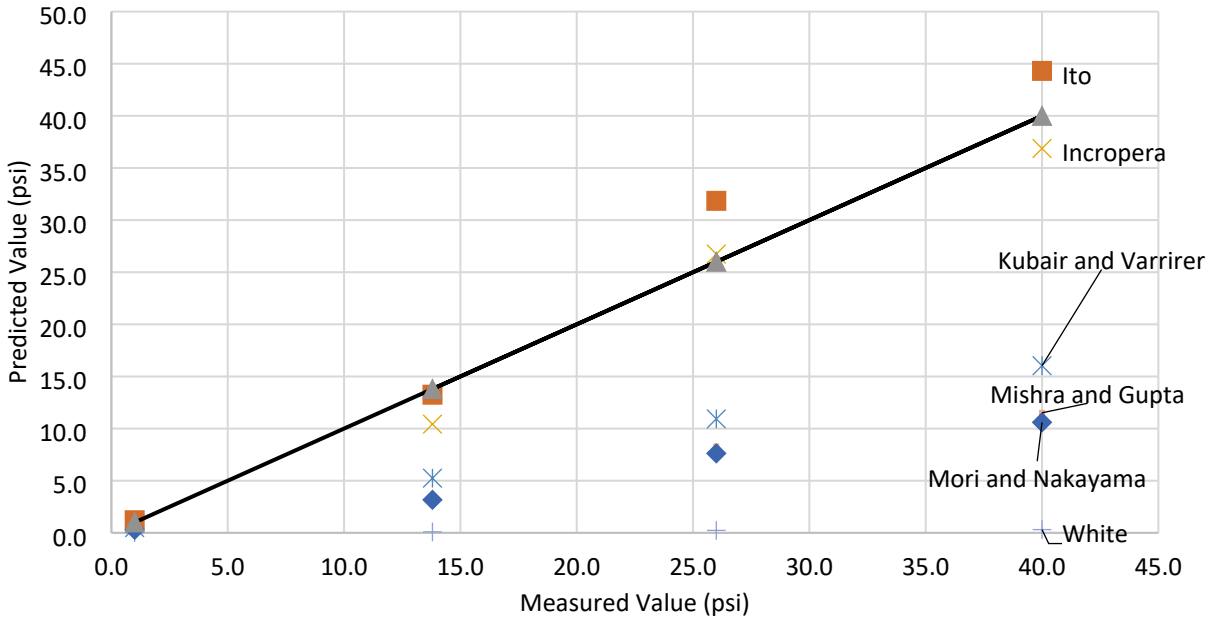


**Figure 4-12. Comparison of measured pressure drop with various literature correlations.**

The next step in this analysis was to compare the performance of the various heat transfer fluids. Performance comparison was based on heat transfer coefficient and pressure drop knowing their

thermophysical properties as a function of temperature. Figure 4-13 and Figure 4-14 show the predicted values for a fluid temperature of 15°C (cooling) and 177°C (heating), respectively, based on the Ito correlation.

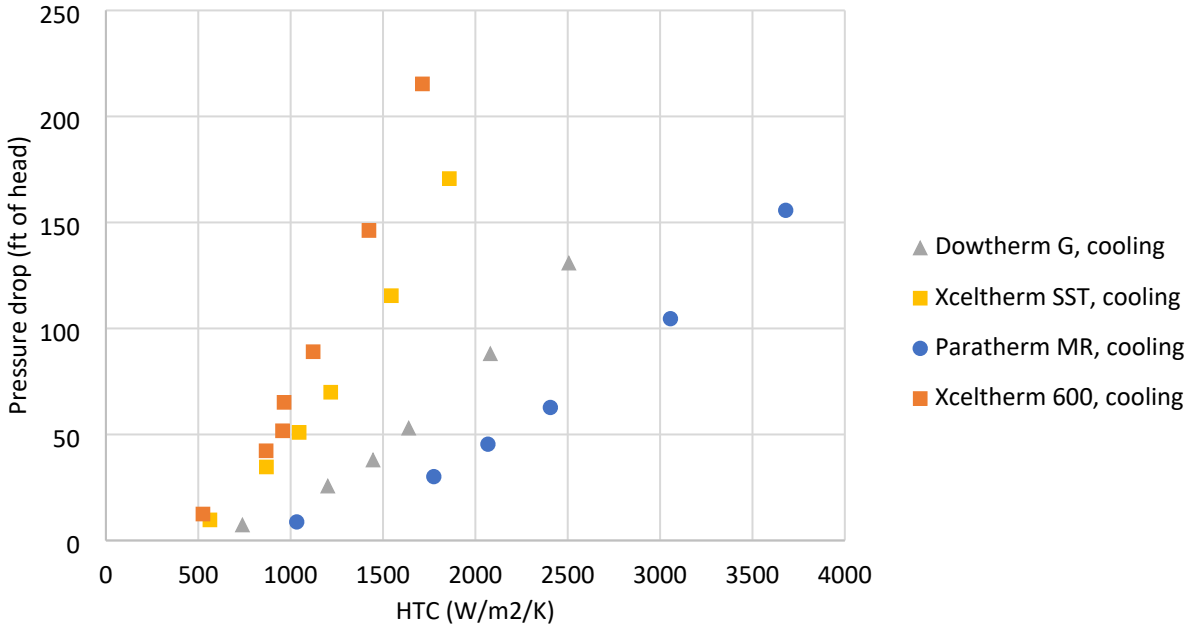


**Figure 4-13. Pressure drop as a function of HTC for cooling.**

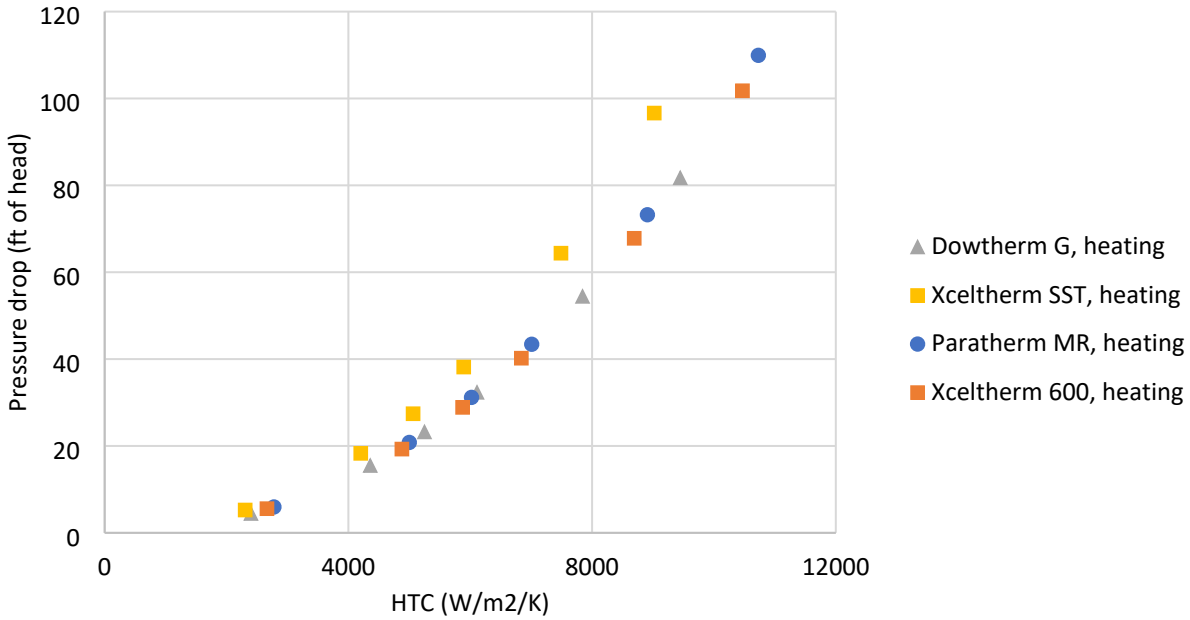


**Figure 4-14. Pressure drop as a function of HTC for heating.**

As Figure 4-13 and Figure 4-14 show, the heat transfer fluid has a greater impact on the heat transfer coefficient and pressure drop during cooling as compared to heating. This is primarily due to the larger

variation in viscosity at low temperature. At high temperature, the heat transfer fluids have similar viscosities.

An additional consideration for the choice of heat transfer fluid was the closed cup flash point as shown in Table 4-2. Based on pressure drop, Paratherm MR would have been chosen. However, since the final design is an open loop system, Xceltherm 600 was chosen as the heat transfer fluid due to the much higher closed cup flash point of 178°C. During initial testing, however, it was found that the viscosity of Xceltherm 600 was too high for the chiller pump, and so the fluid was replaced with Syltherm 800, which has similar properties to Dowtherm G. Due to the lower flash point of Syltherm 800, the final operating temperature was limited to 150 °C.

**Table 4-2. Flash points for selected heat transfer fluids.**

| Heat Transfer Fluid | Flash Point °C |
|---|---|
| Dowtherm G | 130 |
| Xceltherm 600 | 178 |
| XCELTHERM SST | 164 |
| Paratherm MR | 149 |
| Syltherm 800 | 160 |

### *4.2.8. Design Summary*

Based on the modeling and analysis to optimize the compressor bed geometry, a final design was arrived at for the prototype compressor. For the final design, each compressor bed was designed for a maximum allowable working pressure of 15,000 psig at room temperature with an internal cylindrical cavity 4" in diameter and 10" long (see section 4.4.4). The helical coil heat exchanger was made of .375" diameter tubing with a 2.75" helix diameter, 1.0" pitch, and 7.5" height (see section 4.4.1). The insulation sleeve is 0.45" thick Teflon (see section 4.4.3).

The final model assumed a radial effective thermal conductivity of 15 W/mK and an axial effective thermal conductivity of 7.5 W/mK. An MH/graphite composite density of 4,000 kg/m3 was assumed resulting in 2.8 kg of MH per bed. The fluid-side HTC in the helical coil was 5,000 W/m2K for heating and 1,100 W/m2K for cooling based on the heat transfer fluid analysis.

Figure 4-15 shows the resulting COMSOL model prediction for this design. Hydrogen concentration at the end of the 15-min desorption is shown in units of mol/$m^3$. Dark blue indicates fully desorbed MH, while red indicates MH that has not desorbed. This data is used to calculate the amount of hydrogen desorbed by subtracting the volume averaged concentration at the end of the cycle from the initial concentration. Figure 4-15 indicates that a large fraction of the MH is nearly fully desorbed except for small areas near the termination of the helical coil where it exits the ends of the pressure vessel. This is due to an increased heat transfer distance due to the curvature of the tubing at these locations.

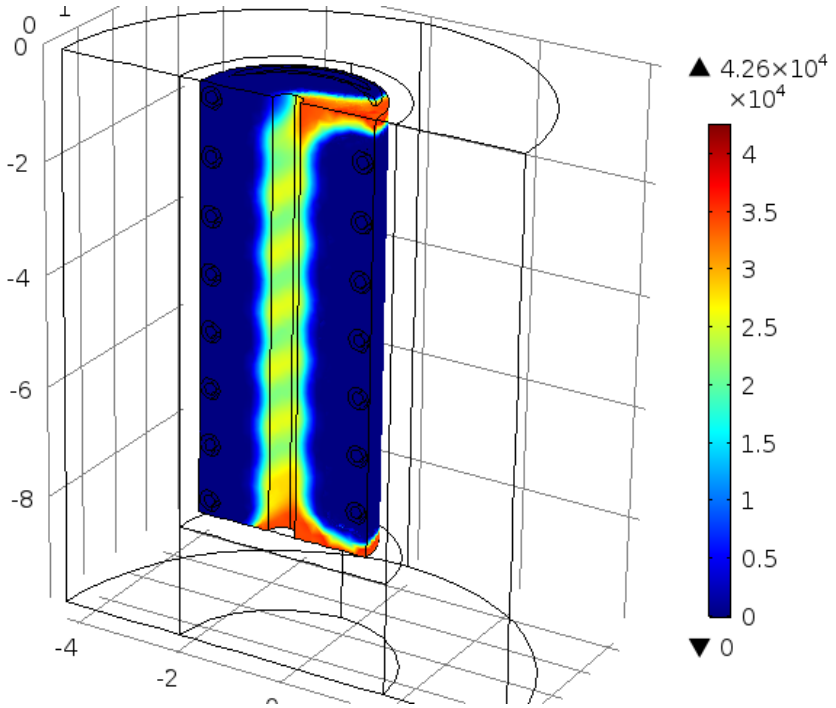


**Figure 4-15. Volume concentration of hydrogen at the end of desorption with kx, ky = 15 W/m²-K.**

## 4.3. Thermal Conductivity Enhancement

The bulk thermal conductivity of $AB_2$ metal hydrides is typically around 1 W/(mK) [20]. Enhanced thermal conductivity is necessary to achieve good performance from the compressor beds which must be alternately heated and cooled to drive the thermodynamic cycles of the metal hydrides. Methods of increasing thermal conductivity include densification of the metal hydride and the use of high conductivity additives. In this project we chose to use expanded natural graphite and form compacted pellets to aid in assembly as well as thermal conductivity enhancement.

Expanded natural graphite (ENG) has been found to be an effective thermal conductivity enhancement material due to its low density and high thermal conductivity [21]. The general pellet formation process begins with particle size reduction of the metal hydride by either chopping or ball-milling. Once combined with the reduced metal hydride powder, this mixture can be compacted into a stable pellet to increase the volumetric storage capacity and effective thermal conductivity. Furthermore, anisotropy resulting from the compaction of ENG can be used to tailor heat flow in the heat exchanger design.

The impact of graphite weight percentage and compaction pressure on the composite thermal conductivity, mechanical stability, and permeability has been studied by various research teams [21, 22]. Studies with Hydralloy C5 mixed with ENG show that an increase in graphite weight percentage is associated with an increase in radial thermal conductivity. When compacted with 75 MPa, radial thermal conductivities measured with 2.5 wt%, 5 wt%, and 12.5 wt% were 3.7 W/(mK), 14.4 W/(mK), and 60 W/(mK), respectively [21]. Cyclic hydrogenation has been shown to decrease the radial effective thermal conductivity by more than 50% of the uncycled composite [22]. However, expansion of the composite during hydrogenation has been shown to improve the heat transfer by closing the gap between MHC and the heat transfer surface [23]. A strong degree of anisotropy between heat

conduction perpendicular (radial) and parallel (axial) to the direction of compression has been found as axial thermal conductivity remained less than 10 W/(mK) [22].

Compaction pressure has been shown to have less of an impact on the effective thermal conductivity than graphite weight percentage. For example, the difference in the radial thermal conductivity between 75 MPa and 600 MPa for the 5.0 wt% was 8.5 W/(mK). Similar measurements for 2.5 wt% and 12.5 wt%, report the difference as 5.3 W/(mK) and 1.5 W/(mK), respectively.

Graphite weight percentage and compaction pressure also impact the porosity and permeability as well as the mechanical stability of the composite. The combination of 5 wt% ENG and 75 MPa is commonly the lowest value of each variable found in literature, suggesting the lower limit of stable composites. Selection of ENG wt% and compaction pressure is impacted by the desired porosity and maximum internal stresses permittable in the system in addition to the target effective thermal conductivity. Porosity directly impacts the gas permeability of the composite. Permeabilities below $1x10^{-16}$ $m^2$ become rate-determining for the overall hydrogenation dynamics of the reaction bed [22]. The permeability is dependent on graphite wt%, but generally, this permeability threshold is between 300 MPa – 600 MPa or a porosity of less than 18-22%.

Generally, the addition of ENG increases compressibility which results in lower porosities at equal compaction pressures [22]. The stress of confined MH composites during hydrogen absorption and desorption has also been studied [24]. These mechanical stresses are due to the lattice expansion of the hydrogen absorbing phase during hydrogen uptake. It has been found that the MH composite composition has a strong influence on the axial stresses. Specifically, increasing porosity and higher ENG-content lead to lower maximum stresses. Higher ENG content decreases the axial stress because the volume of metal hydride is reduced with increasing ENG-content [24].

Following this literature review, it was decided to focus on 10 wt% and 15 wt% ENG composites compacted between 75 MPa and 220 MPa. Initial investigation was completed with Hydralloy C5/graphite composites. Hydralloy C5 was delivered in granular form. The granules were reduced by ball milling in argon for 5 min. The MH powder was combined with 10 wt% and 15 wt% ENG in a tubular mixer (Turbula T2F) for 10 minutes at 110 RPM. Small test pellets (1-inch diameter, 0.25-inch thick) were pressed using a hydraulic press in an Argon glove box as shown in Figure 4-16. These compacts were then measured to verify the thermal conductivity enhancement of the graphite additive. The effective density of each pellet was calculated based on the height and weight of each pellet as well as knowledge of the theoretical density of graphite (2.14 g/cc) and Hydralloy C5 (6.1 g/cc, [22]). Thermal conductivity measurements were made using the Transient Plane Source (TPS) method with a Hot Disk Thermal Analyzer (ThermTest, Inc. TPS2500). This instrument allows for the measurement of anisotropic thermal conductivity (radial and through-thickness) which is expected from compacted ENG, and graphite flake to a lesser degree. As shown in Figure 4-17, compacts made from Hydralloy C5 and 15% by weight ENG have shown radial conductivity up to 29 W/mK prior to cycling. Data labelled 'iso' was measured assuming isotropic properties of the composite. Data labelled 'radial' and 'axial' was measured perpendicular and parallel to the axis of compression, respectively. As previously reported in literature, the radial thermal conductivity was much higher than the axial thermal conductivity and the radial values were more sensitive to compaction pressure than the axial values. This data is compared to previously published data by Pohlmann in Figure 4-18. For a similar compaction pressure and graphite weight percent, measurements were lower than the published data. This may be attributed to surface roughness of the pellets or distribution of the metal hydride and graphite within the pellet.

Based on literature data and tests performed on cycled compacts at SNL, the thermal conductivity is expected to drop by 50% or more after 10 to 20 cycles before stabilizing. This is also supported by the 10 wt% measurements taken before and after hydrogenation and cycling in Figure 4-17. It was decided to focus on 15 wt% SGL Carbon composites compacted to 150 MPa to aim for 15 W/(mK) after cycling. The benefit of high conductivity composites is supported by the COMSOL results shown in Figure 4-19. The figure shows desorption results for two HTC values (5,000 and 7,500 W/(m$^2$K)) and three radial thermal conductivity values (7.5, 10, and 15 W/(mK)). The results show that both parameters increase desorption performance. Over the range of thermal conductivity from 7.5 to 15 W/(mK), the mass of hydrogen desorbed was increased 20 to 25%.

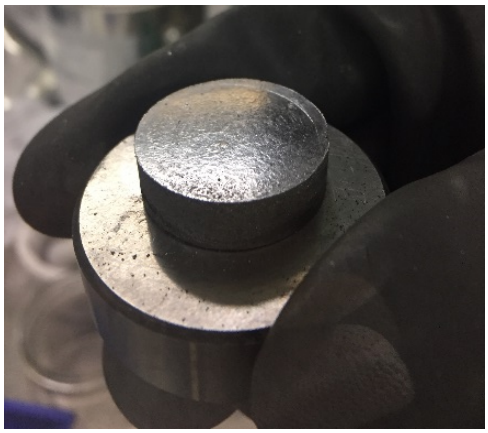

**Figure 4-16. Example of a test pellet used in thermal conductiivty measurements**

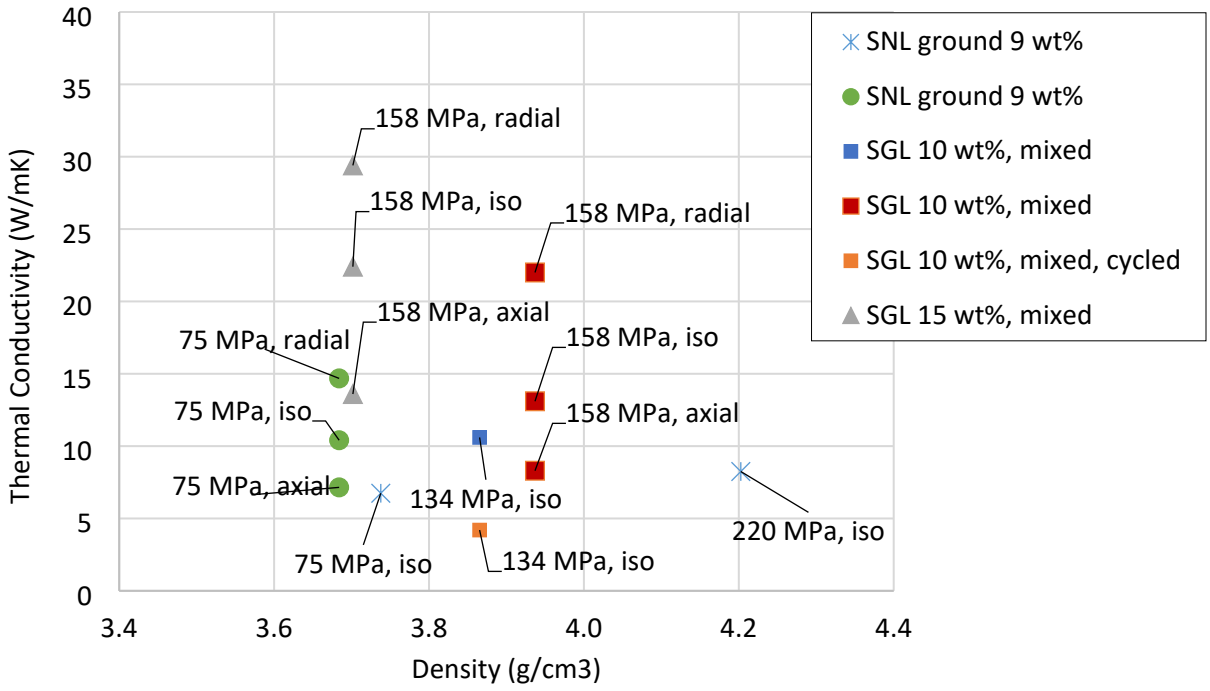


**Figure 4-17. Thermal conductivity values measured by SNL for ground and expanded graphite.**

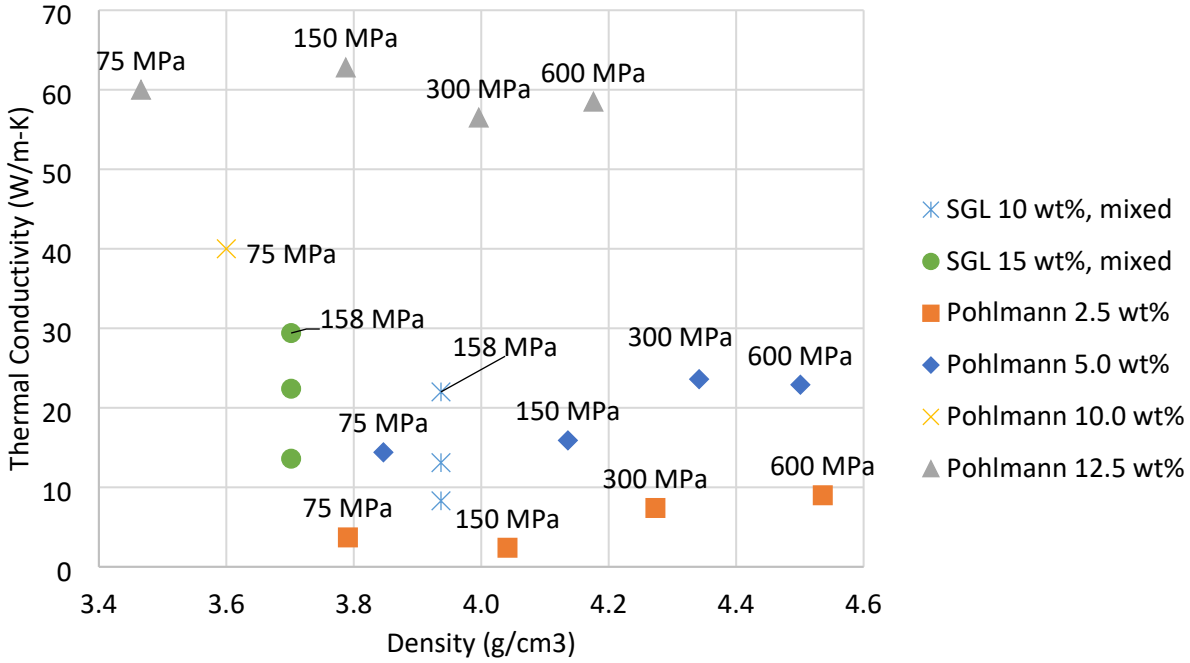


**Figure 4-18. SNL thermal conductivity values compared to values published values [22].**

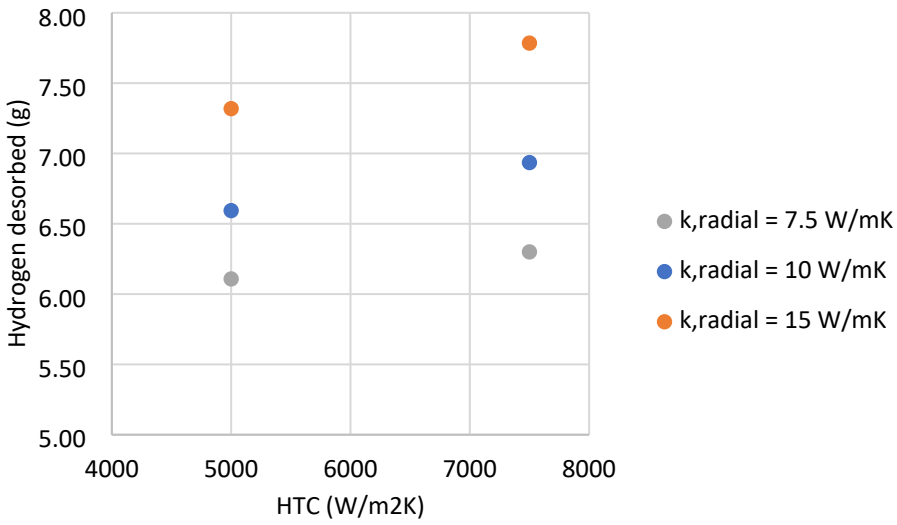


**Figure 4-19. Impact of composite thermal conductivity and heat transfer coefficient on amount of hydrogen desorbed as predicted by the COMSOL model.**

### *4.3.1. Pellet and Pellet Die Design*

As Figure 4-20 illustrates, two compressed pellet shapes were required to pack the helical coil design with metal hydride/graphite compacts. A pie shaped pellet would be used to fill the inner cylindrical space of the helical coil leaving space on axis for the hydrogen distribution tube. A ring-shaped pellet would be used to fill in the space between the helical coils. Based on the initial thermal conductivity

development work it was determined that the pellets would consist of 15% graphite and 85% metal hydride by weight. This mixture would be compacted to up to 150 MPa to achieve a density of 4 g/cc.

To fill the inside space of the helical coil, 56 pie shaped pellets were required with an OD of 2.375", an ID of 0.525", and a height of 0.55". The OD was based on the nominal helix diameter, the ID based on the hydrogen distribution tube diameter, and the height based on the helix pitch so that the pellets could fit between coils. At the desired density of 4 g/cc, each pellet would have a mass of 37.9 grams.

To fill the space between helical coils, 26 ring-shaped pellets were used with an OD of 3.145", an ID of 2.375", and a height of 0.625". The OD was based on the ID of the Teflon liner, the ID based on the nominal helix diameter, and the height based on helix pitch. At the desired density of 4 g/cc, each pellet would have a mass of 45.6 grams.

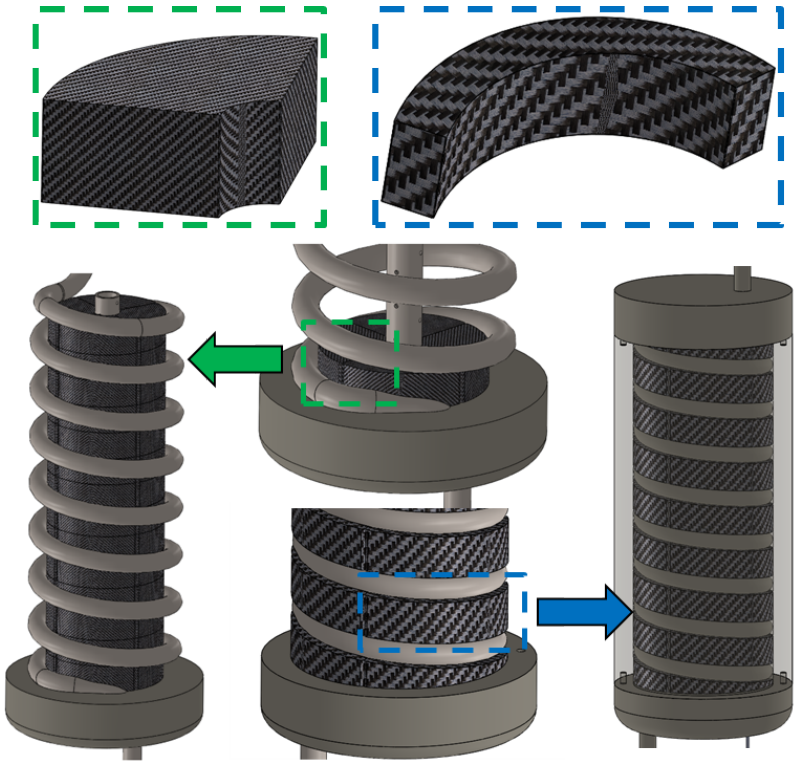

**Figure 4-20. Pre-compressed pellets will be loaded in/around the helical coil and gas distribution tube within the Teflon liner.**

Because of the odd shapes of the pellets, an off-the-shelf pellet die did not exist and a custom design was required. The design of the two pellet die sets was based on commercial die set designs in terms of configuration, material choice and processing for strength and hardness, and surface finish. A structural analysis was performed for both designs to accommodate the desired compression forces with a reasonable factor of safety.

The pellet die sets were fabricated by Header Die and Tool, Rockford, IL. The parts were made from 440C stainless steel heat treated to a Rockwell C hardness of 58. As Figure 4-21 shows, each set

included a base with an integral raised anvil in the shape of the pellet, a sleeve that would attach to the base, and a plunger. It was decided not to use separate anvils like commercial die sets because of the potential difficulty of aligning the small insert in the semi-circular shape in a glove box and confidence by the manufacturer that the required tolerance could be met.

This proved fine for the pie shaped pellets, but problematic for the ring shapes. Without an anvil, the entire length of the plunger is tightly toleranced to the sleeve. Thus, when metal hydride particles slip in the small space between the plunger and sleeve, a large frictional force is exerted over the full length of the plunger as it is used to eject the pellet. While the pie shaped plunger was able to be successfully pressed through the sleeve and removed, the ring-shaped plunger would bind. This required us to change to an anvil arrangement. We had anticipated this potential problem and purchased an anvil for this purpose. However, to get the benefit, we needed a plunger that fit more loosely within the sleeve so it wouldn't bind. Since the plunger now did not need to be tightly toleranced, and it would be expensive and timely to have Header Die and Tool fabricate a second one, we decided to use additive manufacturing. A new plunger was fabricated at Sandia using additive manufacturing with 304 stainless steel. To increase the factor of safety for the ring-pellet die set, it was decided to compress the ring pellet with 15,000 lbs instead of 25,000 lbs. The updated ring shape pellet die set is shown in Figure 4-22.


**Figure 4-21. Custom die sets for producing metal hydride/graphite compacts.**

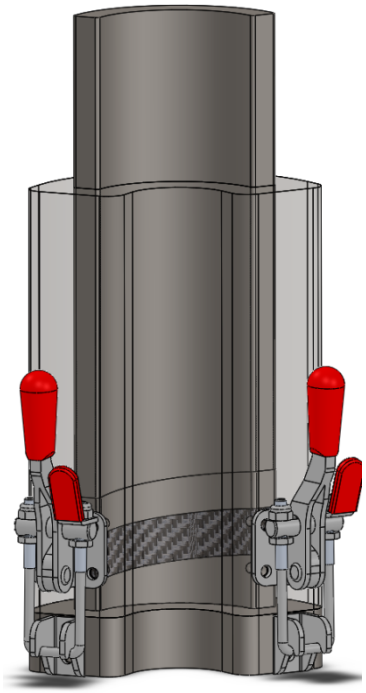

**Figure 4-22. Updated ring pellet design with anvil.**

## 4.4. Compressor Bed Fabrication and Assembly

### *4.4.1. Helical Coil*

The helical coil was designed to maximize heat transfer and minimize volume within the internal cavity of the pressure vessel while also keeping manufacturability and pressure rating at the forefront of the design. Two outer diameters of tubing were considered, .375" and .500". Design variables included the pitch of the coils, the OD of the helix, and the outlet tube location through the ends of the vessel since this is informed by the minimum bend radius.

The final design was based on a tubing OD of .375" rated to 20 ksi, a pitch of 1.00", and a helix OD of 3.125" and ID of 2.750" As shown in Figure 4-23 and Figure 4-24, the helical section was 7.5" in length with an inlet and outlet transition region of 1.25". The straight sections of the tubing were designed to penetrate each end of the vessel and connect to the heat transfer fluid manifold. The helical coils were manufactured by Tube Bending, Inc. A fixture was designed as shown in Figure 4-25 to represent the Teflon liner and outlet locations through the vessel and used to accept the helical coils once manufactured.

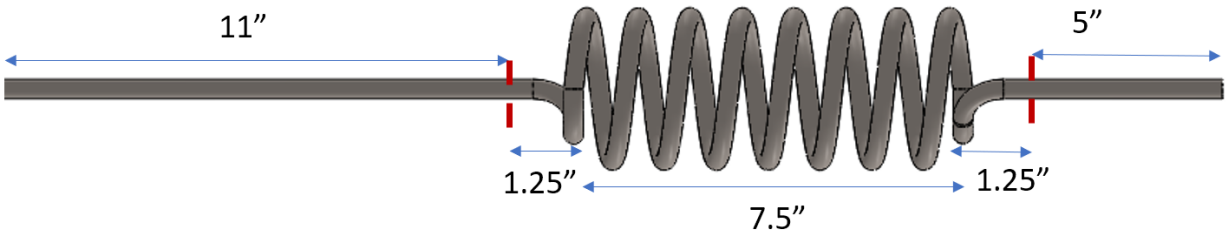


**Figure 4-23. CAD image of the helical coil.**

**Figure 4-24. As-built helical coil.**

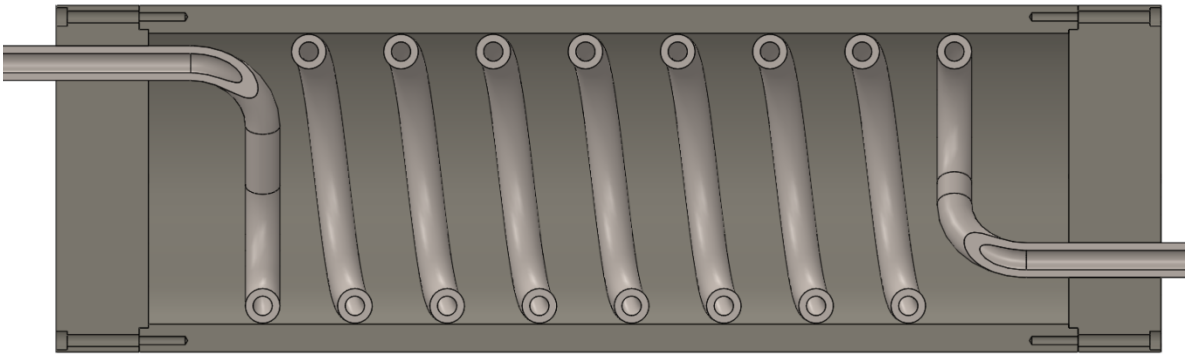

**Figure 4-25. Helical coil acceptance fixture.**

One concern with the fabrication of the helical coils was ovaling of the tube near the straight sections due to the bend in the coil. A non-circular cross-section would prevent good contact between the tubing and the seal and could result in a leak. This was particularly an issue in the section that exited the cover of the vessel due to the proximity of the bend to the vessel seal as shown previously in Figure 4-10. This challenge was realized and resulted in re-machining each cover to move the seal further away from the helix where the tube cross-section was not impacted by the bend.

### *4.4.2. Gas Distribution Tube*

To enhance hydrogen distribution in the compressor beds and minimize pressure drop during absorption and desorption cycles a hydrogen distribution tube was included in the bed designs. For this purpose, a porous sintered metal sparge tube from Mott Corporation was used. The ½" diameter 8.25" long porous tube has a 3/8" inside diameter and is installed on the axis of the bed and fits into recesses in the end caps of the Teflon liner. The sparge tube is aligned with the gas inlet of the bed and has a solid end cap. Thus, during absorption, hydrogen flows to the end of the sparge tube and then permeates the bed radially outward minimizing any axial pressure gradients. As an added benefit, the sparge tube also acts as a secondary filter to prevent metal hydride from migrating into the hydrogen manifold.

A Mott 2300 series seamless 316 stainless steel sparge tube was used for this purpose. Based on the Mott permeability guide and guidance from an applications engineer, media grade 2 porosity was selected to limit pressure drop. A picture of one of the Mott spargers used in the compressor beds is shown in Figure 4-26.

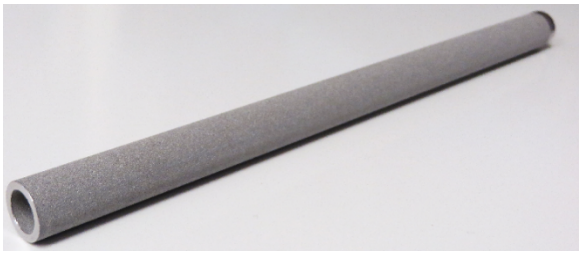

**Figure 4-26. Hydrogen distribution tube.**

### *4.4.3. Teflon Liner*

To minimize heat loss to the vessel, a liner was designed that would fit around the helical coil and MH composites and slide into the pressure vessel as shown in Figure 4-27. The main body was .45" thick while the end caps were 1.0" thick. Teflon was chosen as the material for the liner as a compromise between insulating properties and compatibility with the high-pressure hydrogen environment. Foams were initially considered for the liner that would be much better insulators. However, there was concern that a closed-cell foam would crush under the hydrogen pressure and an open-cell foam would allow hydrogen permeation which would negate the low thermal conductivity of the foam.

**Figure 4-27. Teflon insulating liner.**

### 4.4.4. Pressure Vessels

Several suppliers were contacted to provide quotes for the fabrication of the pressure vessels for our initial prototype design. High Pressure Equipment (HiP) was chosen as the supplier for several reasons: ability to fabricate the vessels from Nitronic 50, ability to meet specifications for temperature and pressure, lowest cost, and previous experience.

Once the vessel geometry was defined for the scaled-down version, HiP was contacted for a quote. The following requirements for the vessel were provided:

- 4.0 inch inner diameter and 10.0 inch inner length
- Design pressure of 15,000 psi
- Design temperature from 10°C up to 175°C
- Wetted material Nitronic 50
- Lid and bottom penetrations with seals to accommodate 0.375 inch diameter tubing of the helical coil
- Hydrogen inlet with high pressure fitting
- One thermocouple feedthrough at a specified location

Through several iterations between HiP and Sandia, a final design drawing was produced and approved as shown in Figure 4-28. The vessel consists of a Nitronic 50 body and cover with a 4340 steel nut to hold the cover in place. The overall dimensions of the vessels are 7.0 inches in diameter and 19.19 inches in length (not accounting for the feedthroughs in the bottom) with a weight of 165 pounds. The cover is sealed with a Viton o-ring that has a 4340 steel backup ring to prevent extrusion. The cover has one penetration for the helical coil heat exchanger inlet. A 13/32 inch through hole was provided for the 0.375 inch tubing. The tubing seal design consists of dual Parker Polypak u-cup seals held within their gland by a 316 stainless steel retaining ring. There are three penetrations through the bottom of the vessel: one for a thermocouple feedthrough, one for the hydrogen inlet and one for the exit of the helical coil heat exchanger. The thermocouple feedthrough uses a standard 60,000 psi rated ¼ inch high pressure fitting with a 1/16 inch sheathed K-type thermocouple. The hydrogen inlet, which is an 1/8 inch hole on the axis of the vessel, also uses a 60,000 psi rated ¼ inch high pressure fitting to mate to ¼ inch high pressure tubing. Finally, the penetration for the heat exchanger tubing consists of dual Parker Polypak u-cup seals like the cover, but has a slightly different configuration with a packing gland and washer holding the seals in place.

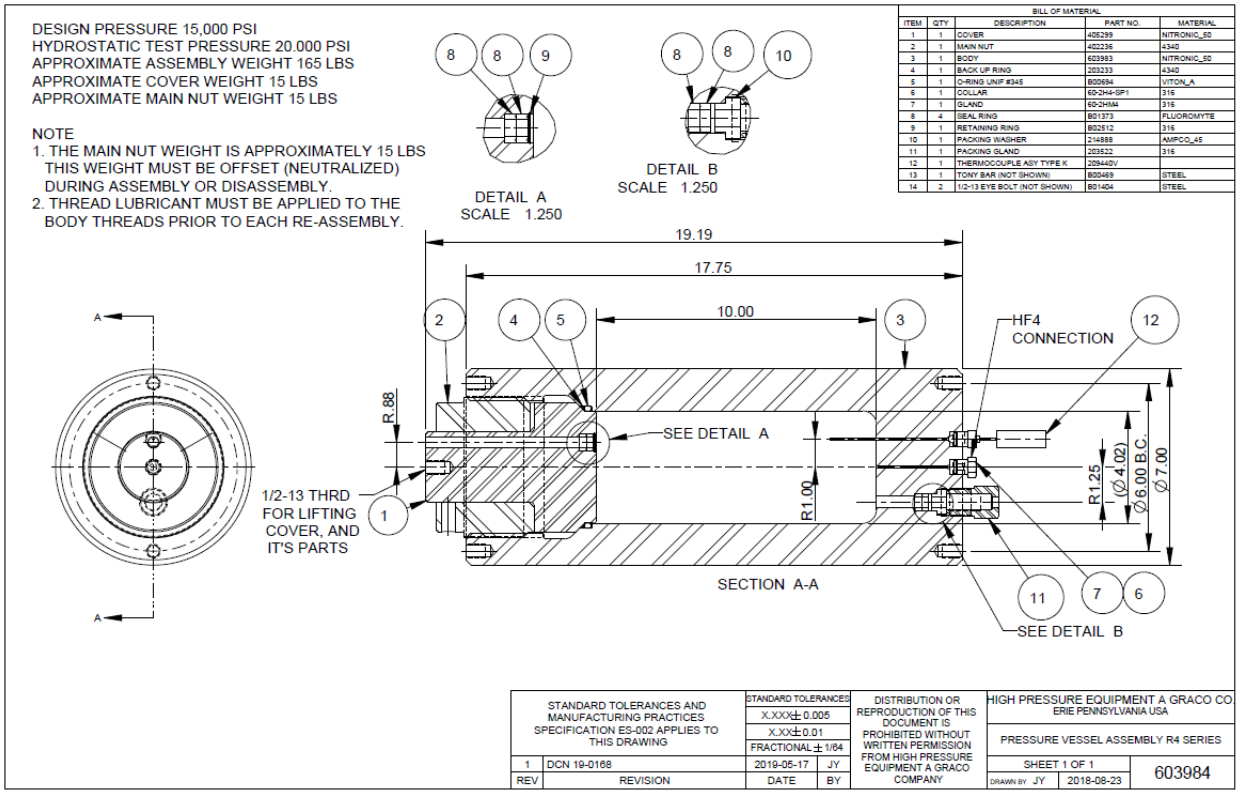


**Figure 4-28. Final approved drawing for HiP pressure vessels.**

The expected delivery of the compressor beds was initially delayed due to an error made during fabrication. Nitronic 50 was specified as the material for the vessel bodies and lid. Unfortunately, the subcontractor fabricated the parts from 4340 steel. Nitronic 50 billets were sourced and the vessel parts were machined again. In parallel, the 4340 vessels were used to perform a leak and pressure test with the helical coil heat exchangers. The vessels were assembled with the heat exchangers and successfully leak checked to 15,000 psi with helium. This provided initial confidence in the design of the vessel seals and the helical coils were shipped to Sandia to begin the assembly of the metal hydride subassemblies.

### *4.4.5. Assembly*

The first step of assembly involved making the center pellets and helix pellets for both the low pressure and high-pressure beds. Ames Lab produced 4 kg each of Ti-based $AB_2$ alloys for the compressor beds. This material was pretreated via high-energy ball milling under argon by HHC. Final particle size was between 10-100 microns.

Graphite and metal hydride powder was loaded into a small plastic container with two mixing balls within a glove box. The sealed containers were removed from the glovebox and mixed in a tubular mixer (Turbula T2F) for 10 minutes at 110 RPM. Each container had enough mixture to form 5-6 center pellets or 3-4 helix pellets. Once mixing was completed, the containers were moved back into the glovebox and the material was poured into the die press. Two manual compressions were performed to fill the die for each pellet. After all material was added to the die, it was placed on the hydraulic press and uniaxially compressed to the final density. The final pellets are shown in Figure 4-29.

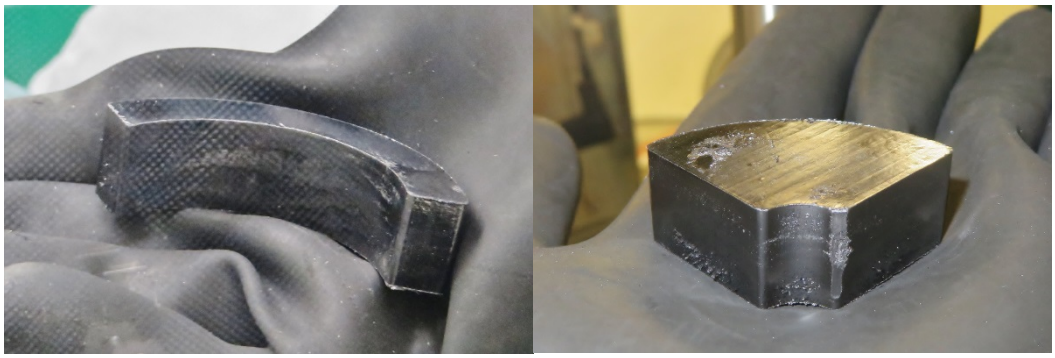

**Figure 4-29. Helix pellet (left) and center pellet (right) examples.**

In all, 56 center pellets and 26 helical pellets were fabricated per bed. As shown in Figure 4-30, these pellets were then loaded into the helical coil heat exchangers for the low pressure and high pressure beds. The figure also shows the hydrogen distribution tube that runs down the center of the bed. This assembly was then inserted into the Teflon sleeves that are used to insulate the metal hydride from the massive pressure vessels. Based on measurements before and after loading, the LP bed was loaded with 2.8 kg of material and the HP bed was loaded with 2.9 kg of material. Given that the mixture was 15% graphite and 85% metal hydride, each bed was loaded with about 2.4 kg of metal hydride. The maximum volume of void space within the Teflon liner was 864.7 cc, so the effective density of the LP material was 3.23 g/cc and the effective density of the HP material was 3.35 g/cc. These values are 16 to 19% lower than the goal density of 4.0 g/cc. In part this was due to the inability of the die press operation to achieve the desired density with the applied compaction pressure. In addition, some void space remained once all of the pellets were fit in the helical coil heat exchanger.

**Figure 4-30. Helical coil being filled with center pellets (left) and then helix pellets (right).**

Figure 4-31 shows one of the vessels being assembled in the Sandia glove box. The Teflon sleeve subassembly was inserted into the vessel body with the heat exchanger tubing protruding through the mating vessel penetrations. Seals were then installed in glands surrounding the tubing. A single thermocouple was inserted into a pre-drilled hole in the end of the compressor to monitor the metal hydride temperature during operation and sealed with a high pressure fitting. The hydrogen inlet valve assembly was also attached to the end of the vessel with a high pressure fitting. This assembly includes a needle valve and an inline filter assembly consisting of one 35 μm and one 5 μm filter. The filters are used to prevent metal hydride powder from contaminating any downstream components (valves and seals). Finally the gasket, lid and nut were installed to seal the vessel body.

**Figure 4-31. Prepping the inner subassembly to be inserted into the pressure vessel.**

Sealed vessels were then removed from the glove box and pressure tested as shown in Figure 4-32. The figure shows the LP vessel attached to a Helium source at ~1000 psi to check for leaks prior to transporting the completed beds to the test facility. The bed thermocouple was also checked to ensure it was operational. Neither bed showed a measurable decrease in pressure during the leak check and a portable He leak detector found no leaks at any of the fittings or seals.

**Figure 4-32. LP bed during He leak check and thermocouple verification.**

# 5. TEST FACILITY DESIGN AND ASSEMBLY

A test facility was designed and assembled at Sandia to permit performance testing of the prototype 2-stage compressor. The test facility consists of three primary systems: a high-pressure hydrogen manifold, a temperature control system with hot and cold oil recirculation loops, and a data acquisition and control system. These systems were assembled in a test cell at Sandia's Hydrogen Effects on Materials Laboratory (HEML).

## 5.1. Hazards Analysis

Operation of the MHC system includes a number of hazards such as high pressure, high temperature, air sensitive metal alloys, a combustible liquid, and combustible gases. To ensure the operational safety of the system a Failure Modes, Effects, and Criticality Analysis (FMECA) was carried out to examine the system for potential failure modes, their associated effects, and to analyze their relative criticality and risk with respect to safety and programmatic impact. Results from the analysis were used to improve and finalize the MHC test facility design and associated testing procedures.

Overall, 346 failure mode effects were identified for the MHC system. Out of those, 266 were identified as being negligible in terms of severity. Of the other 70 failure mode effects, one was identified as catastrophic but improbable and 37 were identified as critical. The critical failure modes were considered further, but none had greater than a remote chance of occurring. In all cases, procedures and both passive and active controls and safeguards were put in place to insure safe operations. A list of procedures and safeguards was developed based on this analysis. Procedures were documented and all trained operators are required to read, understand, and follow these procedures. Safeguards will be fully tested prior to operating the system.

## 5.2. Hydrogen manifold

A piping and instrumentation diagram (P&ID) for the high-pressure hydrogen manifold is shown in Figure 5-1. The completed manifold is shown in Figure 5-2. The high- pressure hydrogen manifold was designed to allow for supply of hydrogen to the prototype compressor at 50 to 150 bar, compression of hydrogen from the low pressure to the high pressure stage, delivery of hydrogen from the high pressure stage at 875 bar, and closed-loop recirculation of the hydrogen back to the supply volumes. The system makes use of existing infrastructure at Sandia's HEML facility including the supply volumes and associated manifold and the manifold and test stand within the high- pressure test cell.

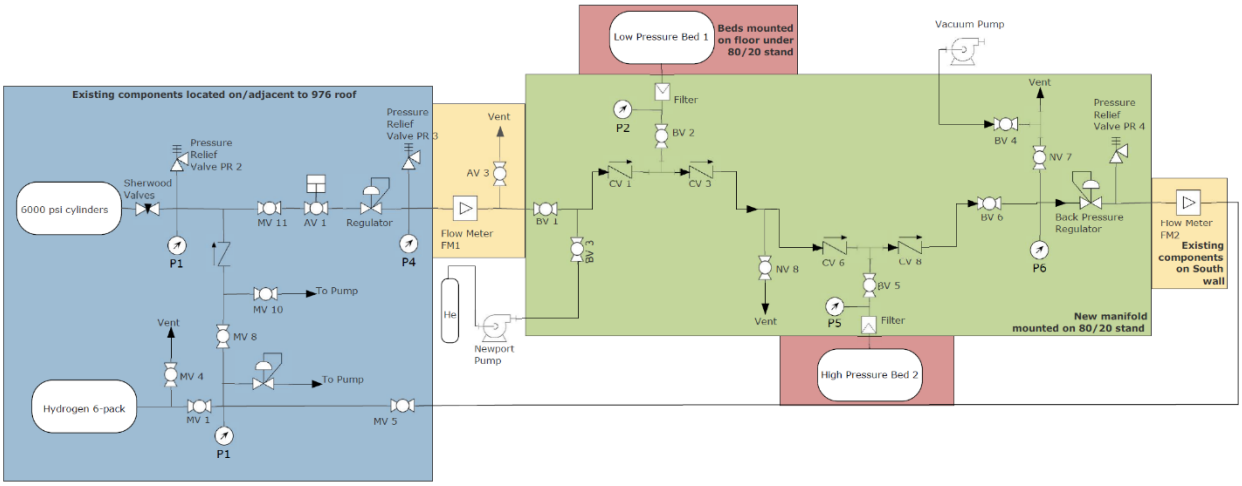


**Figure 5-1. P&ID of the MH compressor hydrogen manifold.**

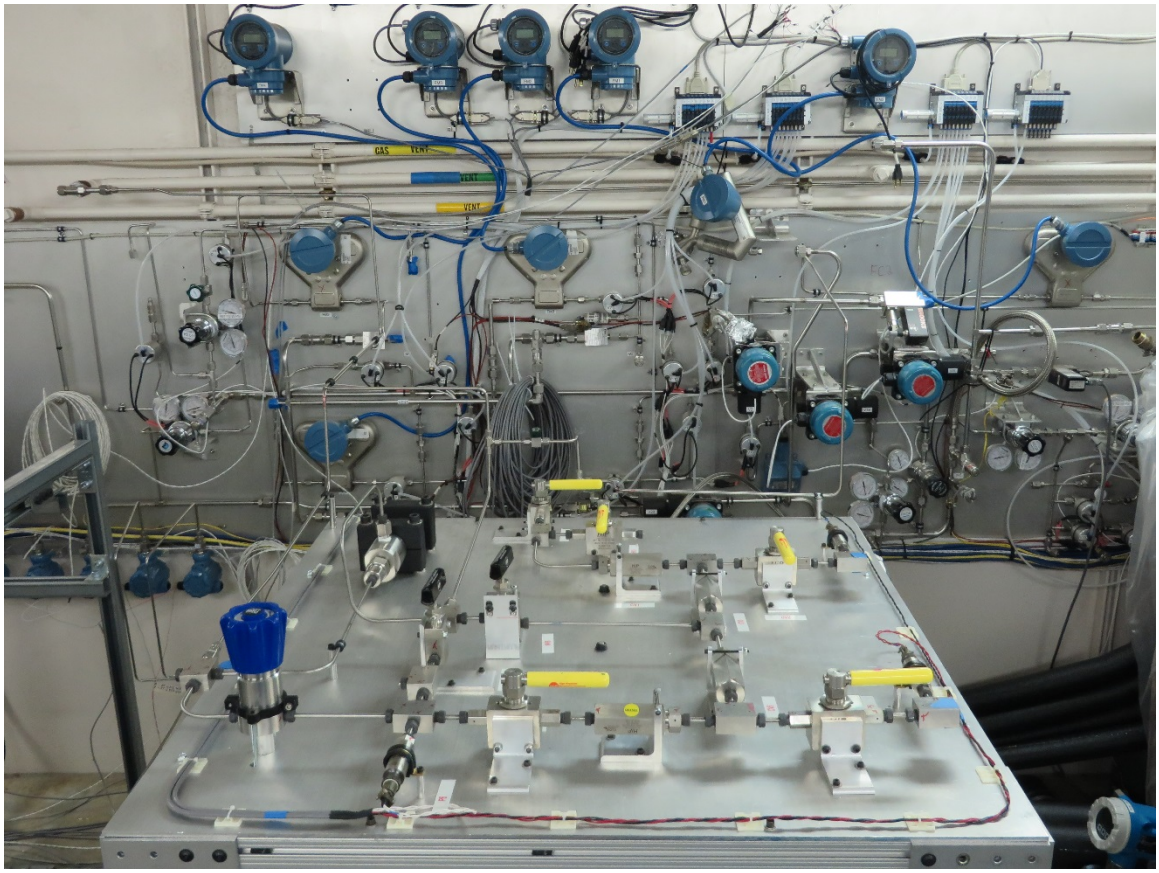

**Figure 5-2. High pressure hydrogen manifold (near) connected to medium pressure manifold (far).**

Control of hydrogen flow through the compressor is achieved through the pressure differences across a set of check valves between the supply and the low pressure bed, the low and high pressure beds, and the high pressure bed and the back pressure regulator set to 875 bar. The pressure of the beds is, in turn, controlled by the temperature of the beds which is achieved by directing the flow of the two fluid loops using a series of pneumatically actuated valves. These valves are controlled by a timer and

relay circuit that triggers valves to open or close at preset time intervals chosen based on the desired cycle time of the compressor.

During MH compressor operation, the low pressure (LP) bed will be cooled to 20°C to initate absorption within the metal hydride. The regulator will maintain a source pressure of 2,175 psig. Once the LP bed is fully absorbed, the LP bed will be heated to 150°C to initiate hydrogen desportion at 8,000 psig. Simultaneoulsy, the high pressure (HP) bed will be cooled to 20°C to inititate hydrogen absorption with the source pressure of 8,000 psig from the LP bed. Once the HP bed is fully absorbed, the HP bed will be heated to 150°C to initiate desorption at 13,000 psig. The back pressure regulator will manage hydrogen flow back to the source cylinders through control of the mainifold pressure at >12,700 psig.

The gas manifold will recirculate hydrogen from gas cylinders on the roof of the test facility through the two MH beds, terminating in the original cylinders. A Newport compressor is also connected to the gas manifold for helium leak checking prior to hydrogen service. All materials of construction for the gas manifold are hydrogen and helium compatible. The manifold is divided into a low-pressure section and a high pressure section. All components are rated above the cylinder source pressure of 3,000 psig: low pressure section components are rated to a Maximum Allowable Working Pressure (MAWP) > 3,500 psig, and high-pressure section components are rated to an MAWP > 15,000 psig. Overpressure protection measures prevent gas manifold components in the system from seeing pressures above their respective MAWP, regardless of the test conditions. Two pressure relief valves installed in the manifold prevent the MAWP of the low-pressure manifold from being exceeded. All relief devices are vented to atmosphere through vent lines. Additionally, regulators control the inlet and outlet gas pressure. Also, an emergency stop button is installed to isolate the hydrogen source from the system by closing the pneumatic valve (AV1).

## 5.3. Oil recirculation system

The oil recirculation system for the compressor prototype consists of two oil recirculation loops that circulate hot and cold oil through the MH compressor as shown in Figure 5-3. Oil temperature will alternate between 20°C and 150°C. The low temperature loop consists of a Thermonics chiller with self-contained pump and heat exchanger. The chiller circulates heat transfer fluid at 20°C through the oil manifold and has a cooling capacity of 3 kW. The high temperature loop is operated with a Thermal Care heater with an internal pump and 6 kW resistive heater. The unit also has an internal tank to allow for expansion of the fluid at high temperature.

Flow from the two oil loops is directed to either the low or high- pressure bed through a series of 3-way valves for heating and cooling. The 3-way oil valves consist of Bonomi 365N (L-port) brass valves, Valbia pneumatic double-acting actuators, and a NAMUR 4-port 110VAC solenoid valve. With double-acting actuators, it takes air to open the valve, and air to close it thus, a 4-way solenoid valve is used to control the states and dual airlines are used for double acting actuation. Each heat exchanger is connected to the oil manifold with a 3-way valve which allows the units to run in a bypass mode. This mode allows the loops to be pre-conditioned to the selected temperature prior to running a test. When a test is initiated, these valves are switched out of bypass and allow the heat transfer fluid to enter the manifold. Four additional 3-way valves are used to direct the hot and cold oil to the compressor beds. These valves are operated in tandem such that either the cold oil is directed to the low-pressure bed and back to the Thermonics chiller while the hot oil is directed to the high pressure

bed and back to the Thermal Care heater or vice versa. This is an engineered safety feature to prevent inadvertently directing both oil streams to one loop.

The heat transfer fluid used in the system was selected based on an analysis of competing criteria and constraints. The fluid had to operate over the desired temperature range without too large of a pressure drop while staying below the flash point at high temperature and above the freezing point at the low temperature. Several synthetic heat transfer fluids were considered.

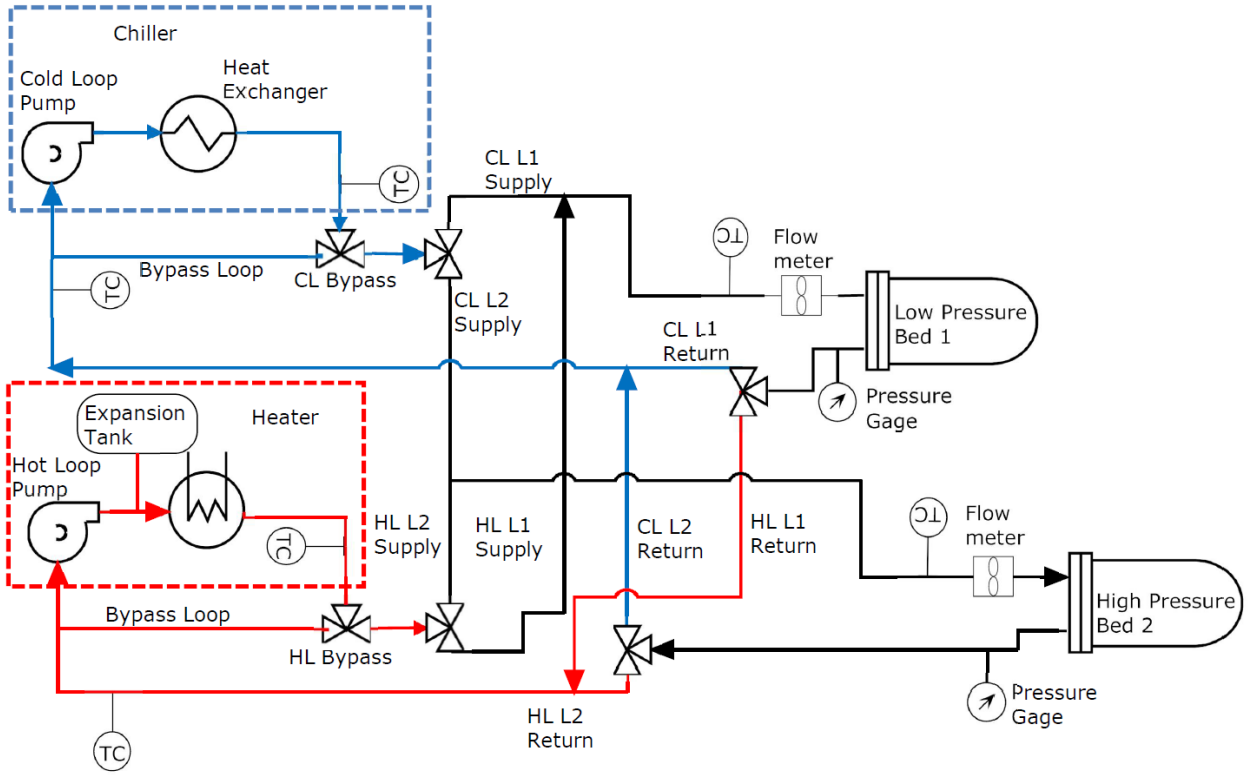


**Figure 5-3. P&ID for the oil recirculation system.**

A CAD model of the oil recirculation system was used to facilitate the layout and assembly of the system as shown in Figure 5-4. The final layout of the system is shown in the photos in Figure 5-5.

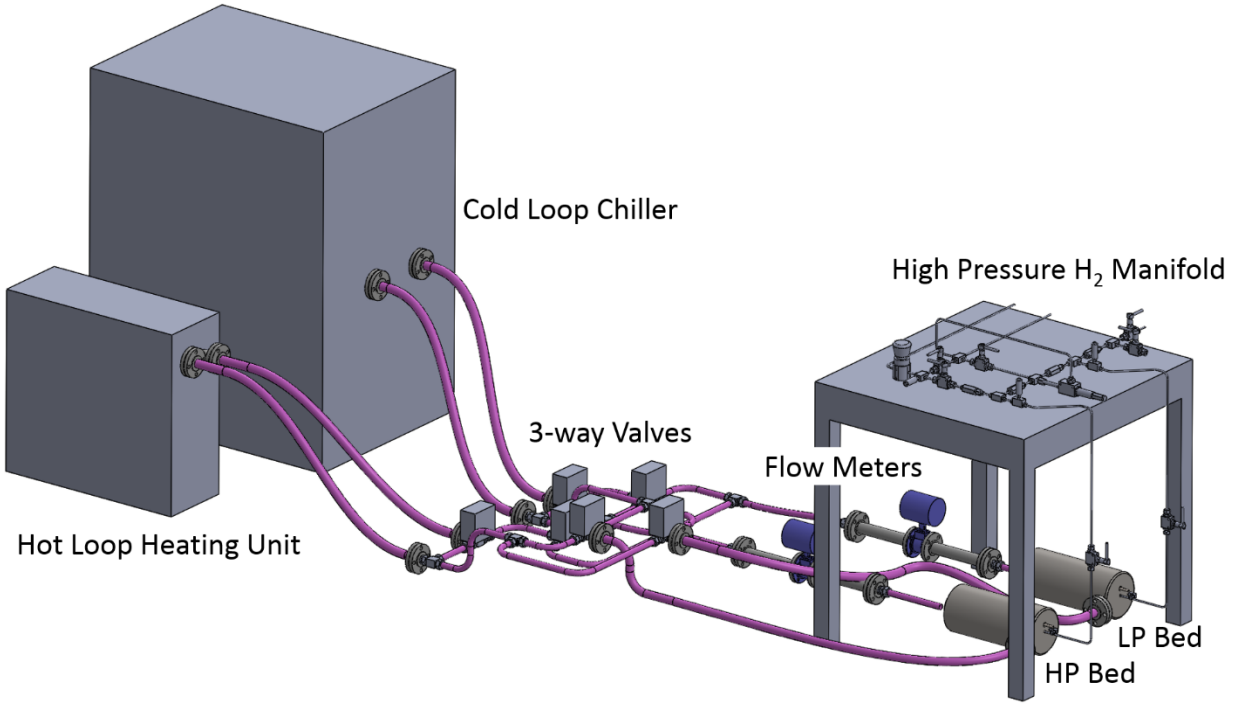


**Figure 5-4. CAD layout of oil recirculation system.**

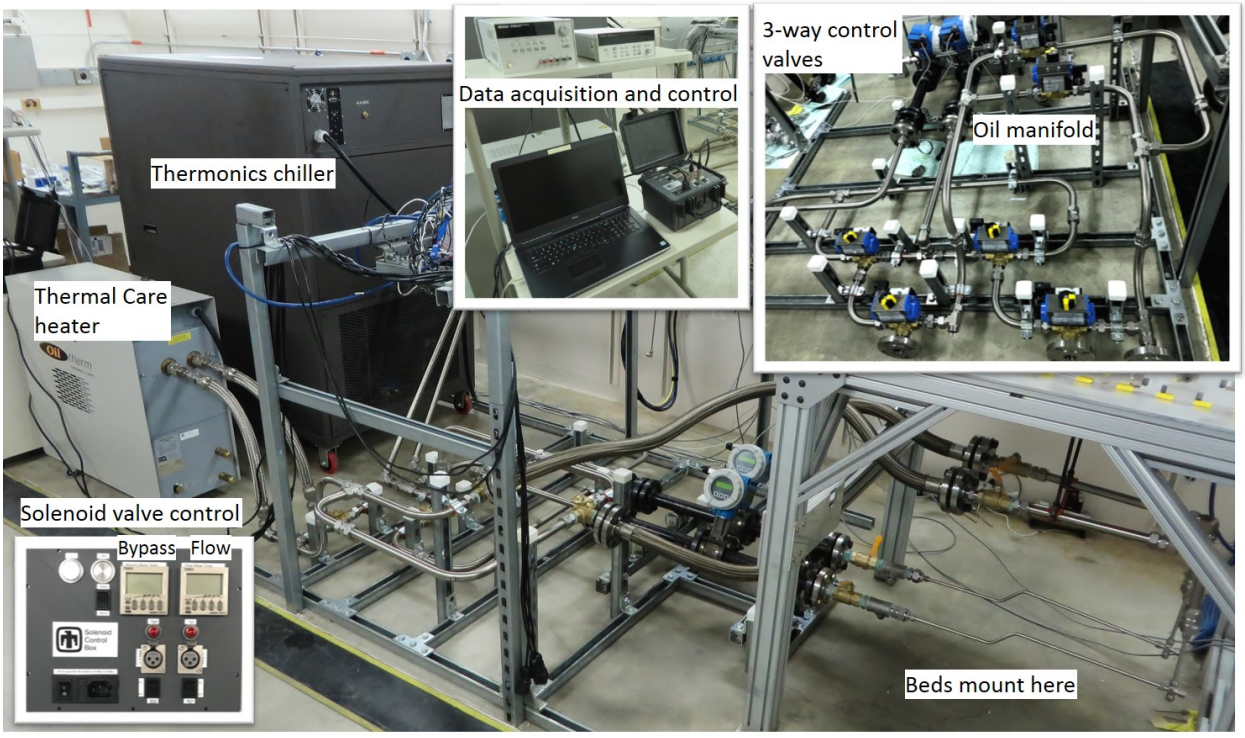


**Figure 5-5. Photos off the oil recirculation manifold, data acquisition and control system.**

## 5.4. Data acquisition and control system

A simple data acquisition (DAQ) was assembled for the MHC system. Data collected consists of the flow rate and temperature of the two oil loops, supply pressure, intermediate pressure, and delivery pressure of the compressor, internal and external temperatures of the two compressor beds, and delivered hydrogen flow rate. An Agilent DAQ unit is used to collect these signals and transmit them to a laptop. Agilent software is used to interface to the DAQ and save data to text files for postprocessing.

Control of hydrogen flow through the compressor is achieved through the pressure differences across a set of check valves between the supply and the low-pressure bed, the low- and high-pressure beds, and the high-pressure bed and the back pressure regulator set to 875 bar. The pressure of the beds is, in turn, controlled by the temperature of the two hydride beds.

The oil recirculation system described above directs the flow of the two fluid loops using a series of pneumatically actuated valves. These valves are controlled by a timer and relay circuit that triggers valves to open or close at preset time intervals chosen based on the desired cycle time of the compressor. The control circuit was also designed to allow for manual operation of the 3-way valves. The controller was designed such that one signal controls the two bypass valves simultaneously while another signal controls the four flow valves simultaneously. The bypass valves have two states, bypass and flow. The flow valves also have two states. The first state directs cold oil to the low-pressure bed and back to the chiller while hot oil is directed to the high-pressure bed and back to the heater. The second state directs the oil loops to and from the opposite beds. In manual mode, these states are controlled by buttons on the controller. In automatic mode, these states are controlled by two timer-relays.

Following the conceptual design for the timer relay control system the final engineering and fabrication of the controller and cables was completed by Sandia electrical engineering and fabrication groups. Figure 5-6 shows the programmable digital timing relay from Allen Bradley that was used for the control system and Figure 5-7 shows the conceptual design of the controller. Photos of the completed controller are shown in Figure 5-5.


**Figure 5-6. 700-HX Multifunction Digital Timing Relays.**

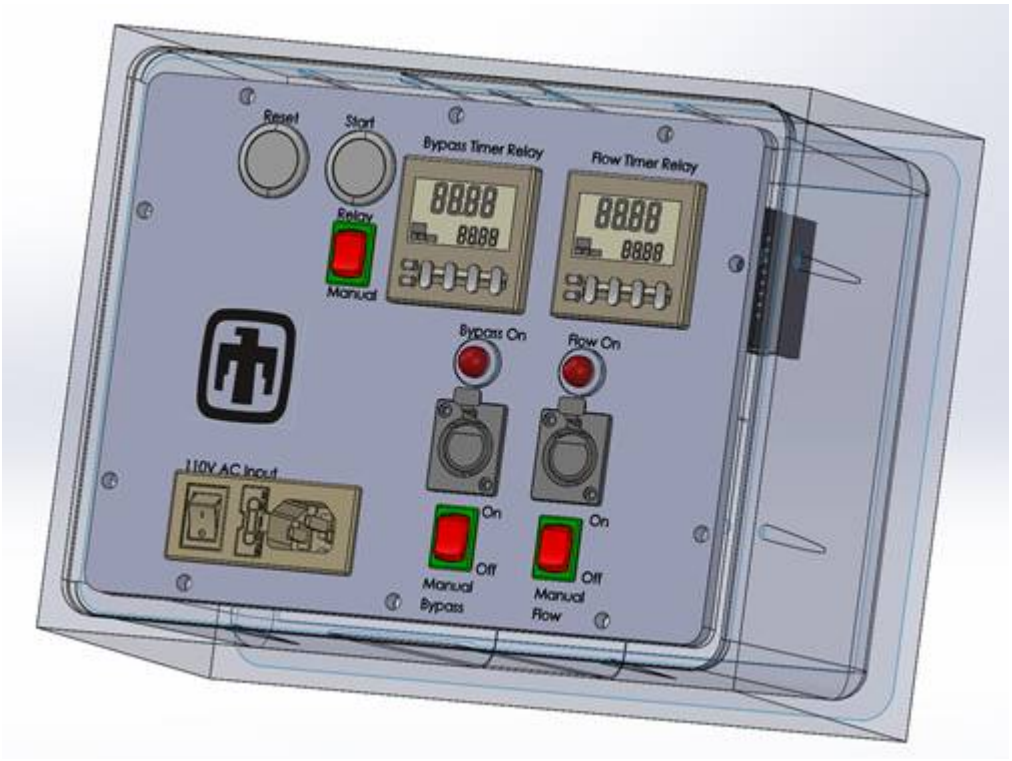


**Figure 5-7. Conceptual layout for the timer relay control system.**

# 6. PERFORMANCE ASSESSMENT RESULTS AND DISCUSSION

## 6.1. Helium pressure checks and temperature cycling

### *6.1.1. Initial Checkout*

Once the compressor beds were integrated with the temperature control system and hydrogen manifold, the next step was to purge and leak check the hydrogen system. For this commissioning process, it was planned to perform all leak and pressure checks with helium before switching the manifold over to hydrogen. Once the manifold was purged, the manifold and beds were leak checked at room temperature up to 10,000 psi with no detectable leaks. The final step in the process was to temperature cycle the beds between the operating temperatures of 20°C and 150°C while at 10,000 psi before switching to hydrogen. During this process, the seals on both beds failed at 10,000 psi at a temperature of 150 °C.

The seals that failed are Parker polypak seals which are u-cup type seals similar to other ones used on various other high-pressure vessels in the HEML at Sandia. These are used to seal around the heat exchanger tubing where it enters and exits the pressure vessels. These seals were recommended by HiP for our application and should have been rated to 15,000 psi hydrogen and temperature cycling between 20 and 175 °C. These seals are used on other HiP systems for dynamic sealing at up to 20 ksi. Since our application is a static seal, HiP engineers were confident that these would work well. The seals were also over-pressure tested hydraulically at HiP at up to 22,000 psi and then leak checked with helium at 15,000 psi with no issues. However, they were only tested at room temperature.

Following the seal failures, the beds were removed from the hydrogen and oil manifolds, the oil was drained from the heat exchanger tubes, they were transported back to the glove box lab, and loaded into the glove box to diagnose the failure. It was confirmed that the seals had extruded out of the gland as the result of the combination of pressure and elevated temperature. Investigation into the failure by HiP revealed two mistakes in the design of the seals and glands. Firstly, the polypak seal material was not rated to the operating pressure at a temperature of 150 °C. Secondly, the gland for the seals was designed incorrectly, allowing a much larger gap between the tubing and the gland inside diameter than prescribed by Parker's design guide. The combination of these two mistakes resulted in the seal failure.

To fix the design mistakes, HiP contacted two seal suppliers to design replacement seals. Bal Seal and Gallagher Seal both designed new seals to meet the appropriate dimensions, pressure rating, temperature rating and the hydrogen requirements for our application. The goal was to have replacement seals that didn't require any modification to the vessels themselves. Based on a joint review of the two seal designs by Sandia and HiP, the Bal Seal design was chosen for the redesign. HIP procured the new seals from Bal Seal that were rated for the pressure and temperature and compatible with the vessel gland dimensions with minor modification. HiP completed the modifications to the pressure vessel glands, installed the new seals and carried out a room temperature helium leak check at 15,000 psi before shipping the vessels back to Sandia. Once received, the metal hydride pellet subassemblies were reassembled in the glove box into the pressure vessels along with seals and thermocouples. The reassembled compressor beds were then removed from the glove box and pressure checked at ~1000 psi with helium.

### 6.1.2. Checkout with new seal design

Following the initial helium leak check of the compressor beds with the new seals installed, the beds were integrated with the test facility. Integration included connection to the hydrogen manifold, low and high temperature heat exchangers, and control and data acquisition system. Helium was then used to purge the entire gas system (low- and high-pressure manifolds, hydrogen supply cylinders, and compressor beds) and then to leak check the system.

The low-pressure manifold and hydrogen supply cylinders were leak checked with helium at up to 2000 psi. A mechanical compressor was then connected to the high-pressure manifold and used to leak check the manifold at up to 10,000 psi. Next, the compressor beds were leak checked.

During the process of leak checking the first compressor bed, we found that the cover seal leaked at higher pressure (> 3,000 psi). However, the seal at the base of the body held pressure at > 10,000 psi. The seals in the cover and base are identical. Additional leak checking was carried out with the second vessel to determine if this issue was specific to the first vessel or occurred at the cover seal on the second vessel. This testing revealed that the cover seal on the second vessel also leaked at ~10,000 psi at room temperature. Leaks were more pronounced at elevated temperature and rapid leaks were experienced during temperature changes from hot to cold and cold to hot.

While the Bal Seal seals and the machined seal glands are identical at the cover and base of the vessels, there are some differences that may indicate why the cover seals leak when the base seals do not. The two seal locations are shown in Figure 6-1. The cover seal is held in place by a shoulder with an inside diameter of 0.406" while the base seal is held in place by a packing washer and packing gland with an inside diameter of 0.376". The base design could provide a slightly more robust backing for the seal but isn't expected to be a major contributor to the leak.

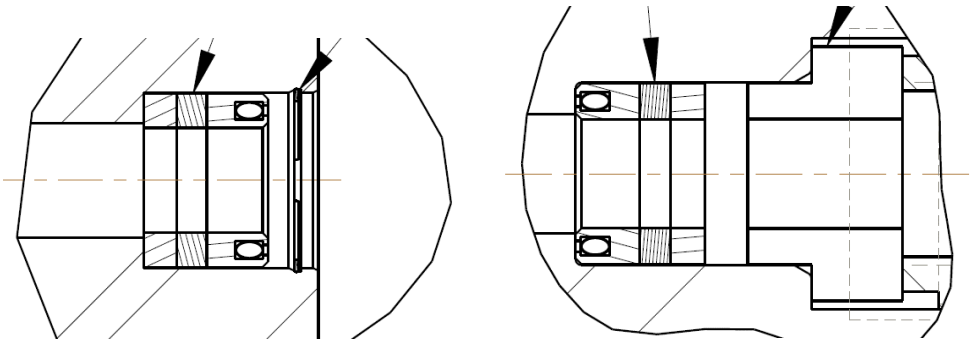

**Figure 6-1. Cover seal (left) and base seal (right).**

As shown in Figure 6-2, the cover seal distance from the tubing bend is 0.44" while the bottom seal distance from the tubing bend is 1.93". The additional distance may provide more flexibility in the tubing to allow for side loading. Another difference is that the cover seal is opposite the gas inlet/outlet while the base seal is on the same end as the gas inlet/outlet. When gas enters the vessel through the base of the vessel, it is possible that it forces metal hydride particles into the seal gland. Finally, the helical tubing assembly was installed first into the base seal and then the cover was installed. This could cause an issue since the tubing doesn't line up perfectly with the cover penetration. Thus, installing the cover may introduce side loading on the seal that damages the sealing surface.

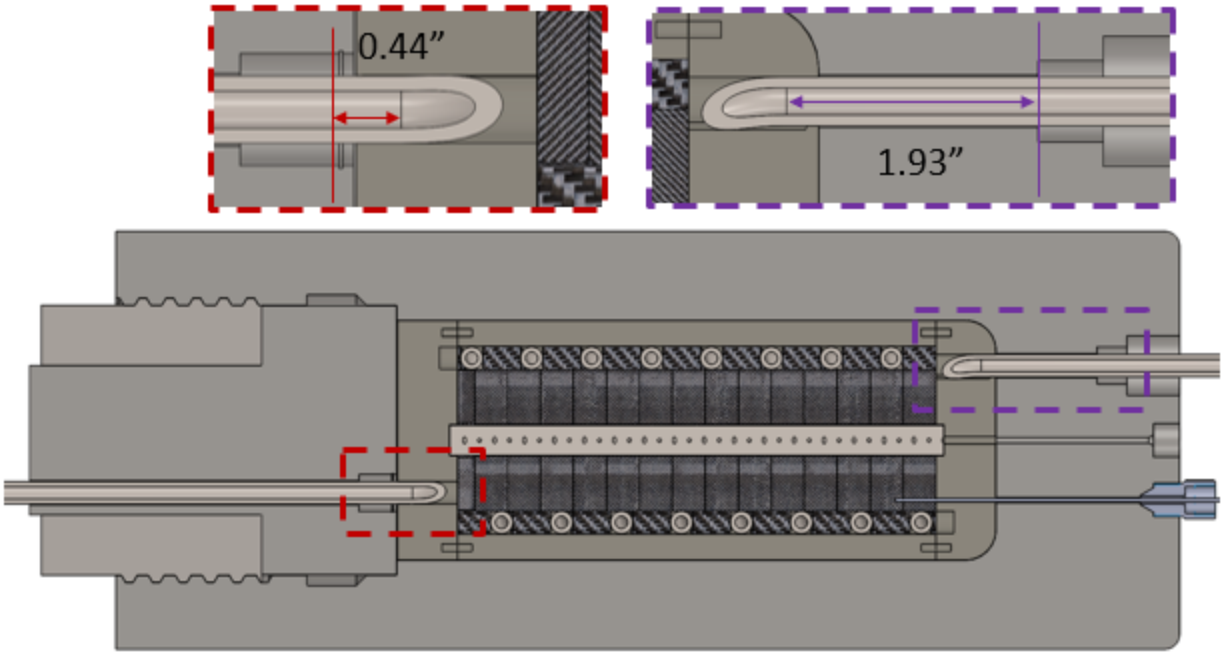


**Figure 6-2. Cover and base seal locations.**

These differences point to some possible causes of the cover seal leaks. Side loading of the seal due to proximity to the heat exchanger coil bend could introduce a leak path. There is imperfect alignment between the helical coil tube and the vessel ports which creates an initial side load. The base seal which doesn't leak has a longer section of straight tubing allowing for more flexibility. The base seal also has a packing washer which keeps the tube straight as it passes through the seal. Shimming the inlet tubes on both vessels to center them in the cover penetration lowered the leak rates, indicating that this was at least a partial cause of the leaks.

Additional side loading of the cover seals could be caused by thermal expansion and contraction of the helical coil. The tubing will expand and contract axially with temperature but being constrained by the vessel may cause bending or twisting. Also, the external heat exchanger tubing leading to the vessel inlets will expand and contract with temperature. The lack of strain relief on this section of tubing results in force on the tubing potentially causing it to bend.

Tube surface finish or defects could contribute to the cover seal leaks. The tubing could be damaged during cover installation because of the mismatch in the vessel penetrations and the helical coil tubing. An example of this was witnessed following the cover installation on the high-pressure vessel. The inlet tubing was slightly crimped after initial installation. The surface was then polished, and the cover was re-installed, and leak checked successfully.

Metal hydride powder contamination is another potential cause of the cover seal leaks. The metal hydride is compacted into pellets for assembly, but the powder is pervasive in the vessel. The hydride particle size is 10 to 200 microns. Every effort is made to ensure that the metal hydride does not contaminate the sealing surface during installation. Also, the base seal is as susceptible to powder contamination during installation as the cover seal. However, the cover seal is opposite the gas inlet and powder may be carried into the seal upon pressurization. According to Bal Seal, this should not

be a problem because the seal is spring energized such that powder should not be able to encroach on the sealing surface.

Combinations of the above could also explain the leaks witnessed with the cover seals. For example, side loading due to proximity to the tubing bend creates a small gap for a leak and then initial pressurization forces particles into the gap creating a larger leak. This could also happen due to side loading from thermal expansion and contraction.

In order to assess several of these potential causes, the vessel covers were disassembled and the seals were removed and inspected. This required uninstalling the vessel from the test facility, transporting to another building, installing into a glove box, and performing the disassembly and inspection in the glove box. The vessel covers were removed, and the covers, seals, and tubing were examined. A few issues were found:

1. Both seals showed powder on the inner diameter surface indicating that powder was forced between the seal surface and the tube during the gas leaks
2. The high-pressure vessel plastic backup ring showed signs of extrusion
3. The low-pressure vessel seal had a small axial scratch with embedded powder

In parallel with this action, a meeting was held between Sandia, HHC, HiP and Bal Seal to discuss the issue and develop a solution(s). It was agreed that one solution would be to redesign the cover seal gland to mirror the geometry of the base seal. This involves a modification to the covers to move the gland further away from the bend in the heat exchanger tubing. HiP agreed to complete this redesign and add a packing washer to the cover seal. Possible modifications to the seal design were also discussed but Bal Seal confirmed that the seal as designed should work for this application and cited the fact the bottom seals worked as evidence. Several modifications to the test facility configuration were also discussed relative to reducing the thermal expansion issues.

Following the meeting, HiP developed a new design for the cover seal glands. Figure 6-3 below shows the new design. The cover dimensions were modified so that the distance to the seal in the cover matches the distance to the seal in the body. This increased distance gives the tubing extra flexibility and stability in order to reduce the amount of side loading that the seal encounters. The addition of a packing washer also helps align the tube with the seal and absorb any side loading rather than transferring that load to the seal. HiP also added a 0.015-0.020" inside radius to the cover where the seal sits that requires the metal back up ring of the Bal Seal seal to have a chamfer. Bal Seal subsequently added this feature to their seal design and Sandia ordered new seals.

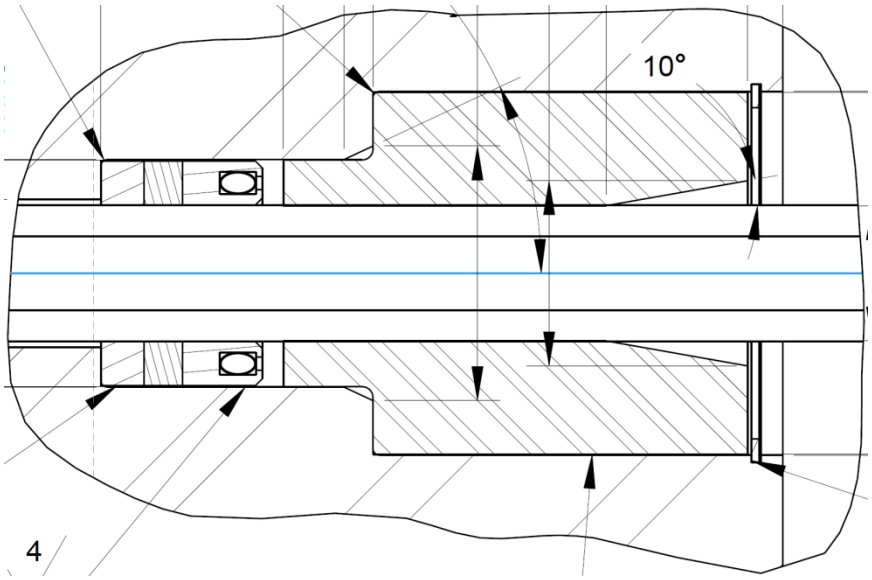


**Figure 6-3. New cover seal design**

### *6.1.3. Final checkout with redesigned cover seals*

The covers of both vessels were removed and shipped to HiP for modification. Several modifications to the test facility configuration were also completed to reduce thermal expansion issues of the oil manifold. The modified covers and seals were then shipped back to Sandia. The vessels were re-assembled, leak checked, and installed back in the test cell.

Room temperature helium leak checks to ~10,000 psi were completed on both beds with no detected leaks. The beds were then heated and cooled simultaneously from 20°C to 150°C while helium pressure fluctuated from about 7,000 psi to about 10,000 psi due to the change in temperature. The beds were temperature cycled 4-5 times over a period of several hours and no leaks were detected.

Based on these results, it was determined the system could be switched from helium to hydrogen operation.

## 6.2. Hydride activation and initial cycling

### *6.2.1. Low-pressure bed Cycle #1*

The low-pressure bed was activated and cycled first. For reference in the following discussion, the low-pressure bed contains 2.38 kg of the Ames #3 alloy ($TiCrMn_{0.7}Fe_{0.2}V_{0.1}$) which, based on small sample testing, has a maximum capacity of about 1.75 wt%. This equates to a maximum hydrogen capacity of 41.7 grams for the low-pressure bed. Prior to hydrogen activation, the bed was purged with helium at high temperature to remove any potential contaminants. Then, once the gas manifold was switched to hydrogen, the bed was purged five times with hydrogen from 1500 psi to 100 psi while heated to 150°C. The low-pressure bed was then pressurized to 2000 psi at temperature and allowed to cool under hydrogen pressure overnight. A small hydrogen leak in the hydrogen manifold prevented an estimate of the hydrogen absorbed, but the data suggested a nearly full absorption occurred on this first cycle.

The first desorption cycle was performed first by heating the bed with the valve to the manifold closed. The heater temperature was set to 100°C and as the temperature of the bed increased to about 95°C, the bed pressure increased to about 5,900 psi (407 bar) which is consistent with about 1.4 wt% capacity. The bed was then desorbed into a large volume with an initial pressure of 70 psi with the back-pressure regulator set to about 2000 psi. The desorption volume pressure increased to 151 psi while the bed temperature dropped to 70°C and then increased back up to 88°C. The temperature drop is consistent with rapid desorption as the release of hydrogen from the metal hydride has a heat of formation of about 20 kJ/g-$H_2$. As the equilibrium pressure of the metal hydride reached the pressure setpoint, the desorption rate slowed and heat input from the helical coil heat exchanger increased the temperature.

The BP regulator pressure was then reduced to 950 psi and the desorption volume pressure increased to 193 psi while the bed temp dropped again to 72°C and then climbed back up to 91°C. A third drop in the back pressure to just under 500 psi allowed more hydrogen to desorb and the desorption volume pressure increased to 210 psi. The heater setpoint was then increased to 150°C and as the bed heated, the desorption volume pressure increased to a final pressure of 222 psi.

The desorption volume has a reported volume of 37.44 liters. Based on a pressure change from 70 psi to 222 psi, this equates to 33 grams of $H_2$ desorbed or 1.38 wt%. Note that this is quite close to the 1.4 wt% estimated based on the initial equilibrium pressure achieved.

### *6.2.2. Low-pressure bed Cycle #2*

Immediately following Desorption #1, the desorption volume was isolated, and the low-pressure bed was pressurized to 2,154 psi with the hydrogen 6-pack while still hot. The heater was then turned off and the chiller was used to cool the LP bed. As the bed temperature dropped the source pressure dropped as the bed absorbed hydrogen. The source pressure dropped to a final value of 1,975 psi at a bed temperature of 14°C. As with the first cycle, the small leak in the manifold prevented an accurate estimate of the total hydrogen absorbed. Assuming a leak rate consistent with other data, the estimated capacity was 31.5 grams or 1.32 wt%.

Following the absorption, the low-pressure bed was left overnight and was not isolated from the manifold. Due to the leak in the manifold, an unknown amount of hydrogen escaped the bed. Thus, the desorption data showed a limited bed capacity. The cycle was started by isolating the bed and heating to first 100°C and then 150°C allowing for pressure equilibrium at each temperature. Pressure reached about 4,300 psi with a bed temperature of 95 °C and then 7,728 psi with a bed temperature of 142 °C.

The bed was then subsequently desorbed into two desorption volumes. The pressure of the first volume started at 2,012 psi and increased to 2,121 psi as the bed desorbed. The bed temperature dropped from about 140°C to below 110°C initially and then recovered to about 135°C. This first desorption step took about 10 minutes. The pressure change equates to 20 grams or 0.8 wt% hydrogen desorbed.

The bed was then desorbed into a second volume at lower pressure. The pressure started at 424 psi and ended at 453 psi indicating another 6 grams or 0.25 wt% capacity. The second desorption step also lasted about 10 minutes.

Following this cycle, the small leak in the hydrogen manifold was identified and fixed so that subsequent test data would be unaffected.

### 6.2.3. *Low-pressure bed Cycle #3*

Absorption #3 started with a source pressure of 2,246 psi and with the bed temperature maintained at 12°C. The pressure regulator upstream of the high-pressure manifold was set to about 1,980 psi for this cycle. The manifold was pressurized up to the LP bed valve and then the valve was opened. As shown in Figure 6-4, the source volume pressure (yellow curve) dropped immediately to ~2,165 psi and bed temperature (green curve) increased rapidly to 64°C. This is consistent with the rapid kinetics of a fully activated interstitial metal hydride of this type. Although most of the hydrogen was absorbed in the first 15 minutes, the bed was allowed to cool for about 35 minutes while it continued to absorb hydrogen and the source pressure dropped to 2,093 psi. The bed pressure was held constant throughout the absorption cycle by the upstream regulator. The total source volume pressure drop equates to about 33 grams of hydrogen or 1.37 wt%. The sawtooth pattern of the heat transfer fluid inlet and outlet temperatures (light blue and maroon curves) is due to the chiller feedback control attempting to maintain a 12°C setpoint.

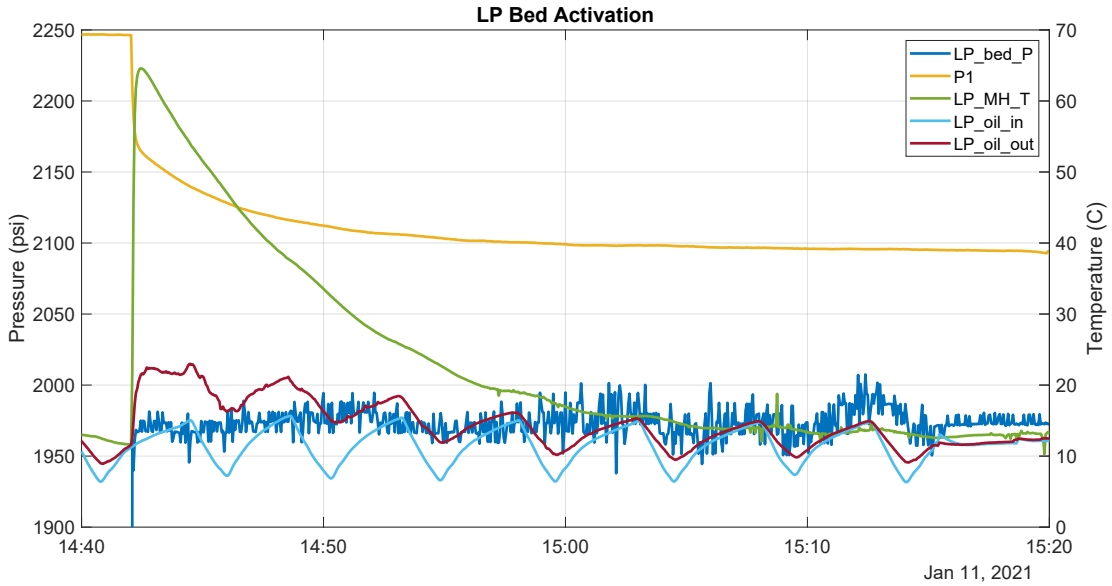


**Figure 6-4. Low pressure bed Absorption #3.**

The measured hydrogen flow rate for Absorption #3 is shown below in Figure 6-5. Note that the large spike in flow (> 1.8 g/sec) correlates to the rapid pressure drop in the source pressure as the valve is opened to the low-pressure bed. Note also that the flow meter doesn't capture flow after about 14:50 even though the pressure curve in Figure 6-4 continues to drop. The flow rate at this point is below the resolution of the meter.

Integration of the flow rate gave a total of about 28.6 grams absorbed up to 15:00. Comparing to the capacity calculated based on the source pressure, the pressure change up to 15:00 also gave 28.6 grams. So, although the flow meter did not capture the final 4.4 grams of hydrogen absorption, it matches closely with the pressure-based capacity calculation.

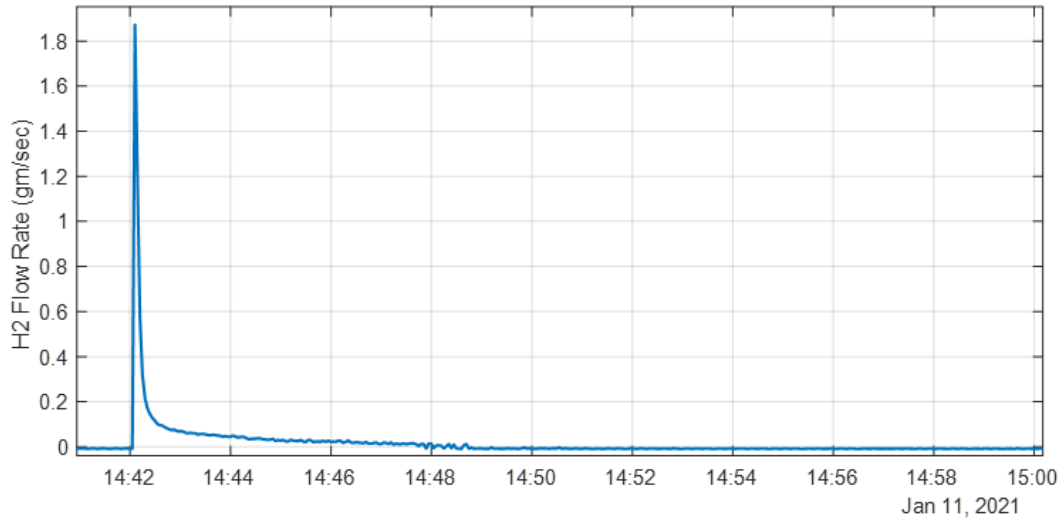


**Figure 6-5. Hydrogen flow rate for Absorption #3.**

Desorption #3 was carried out by first isolating the low-pressure bed and heating with a setpoint of 150°C. The measured pressures and temperatures for this cycle are shown in Figure 6-6. The light blue curve is the temperature of the heat transfer fluid as it enters the helical coil heat exchanger and the maroon curve is the exit temperature. As the bed heated, the pressure (blue curve – bed pressure; orange curve – BP regulator pressure) rose to 9,193 psi while temperature rose to 139°C in the bed (green curve). The BP regulator pressure was then lowered in steps to ultimately allow the bed to equilibrate with the desorption volume. The bed temperature dropped to 106°C as it desorbed. The sink pressure (yellow and purple curves) started at 2,108 psi and increased to 2,245 psi which equates to 25 grams of hydrogen and 1.05 wt%. The bed was then opened to a second desorption volume in which the pressure started at 618 psi and increased to 646 psi which equates to an additional 6 grams of hydrogen or 0.25 wt% for a total of 1.30 wt% desorbed. The whole volume was then vented down to 267 psi to further reduce the bed capacity prior to the fourth cycle. The duration of the desorption process was approximately 20 minutes once the bed was at temperature.

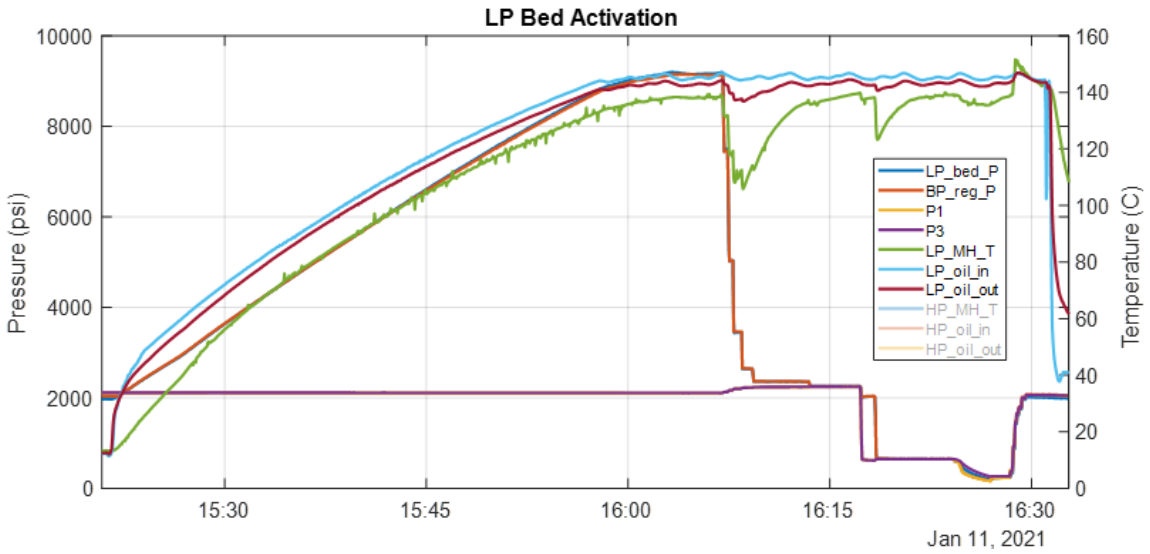


**Figure 6-6. Low-pressure bed Desorption #3.**

Figure 6-7 shows the flow meter data for Desorption #3. For the data up to 16:14, the integral of the flow meter gave about 36 grams desorbed. Based on the scale factor determined for this flow meter, the value is 26.3 grams. The pressure-based capacity calculation for this time period showed 25 grams desorbed which is quite close. From 16:16 to 16:20 the flow meter integral gave another 7 grams desorbed which again is close to the pressure-based value of 6 grams.

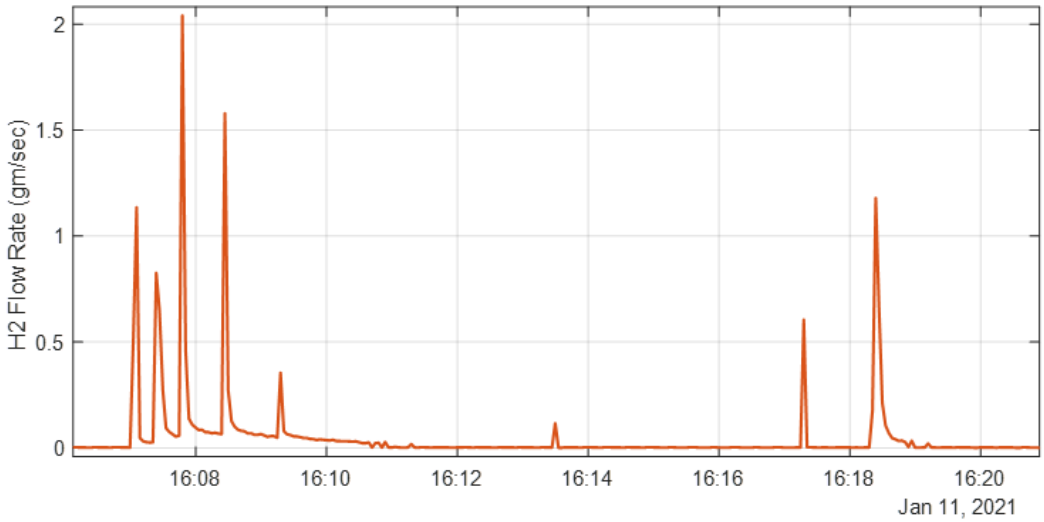


**Figure 6-7. Hydrogen flow rate for Desorption #3.**

The rapid absorption and desorption kinetics and good capacity demonstrated in this cycle indicated that the low-pressure bed was fully activated.

### *6.2.4. High-pressure bed Cycle #1*

For reference in the following discussion, the high-pressure bed was loaded with 2.47 kg of Ames #2 alloy ($Ti_{0.8}Zr_{0.2}Fe_{1.6}V_{0.4}$), which, based on small sample testing, has a maximum capacity of about 1.8 wt%. This equates to a maximum hydrogen capacity of 44.5 grams for the high-pressure bed. Like the

LP bed, prior to hydrogen activation, the bed was purged with helium at high temperature to remove any potential contaminants. Then, once the gas manifold was switched to hydrogen, the bed was purged five times with hydrogen from 1,500 psi to 100 psi while heated to 150°C.

For the activation of the high-pressure bed, the LP bed was used to provide the required hydrogen pressure because of the high equilibrium pressure of the HP bed. During transfer of hydrogen from the LP bed (desorbing at ~145°C) to the HP bed (absorbing at 15-20°C) there is no diagnostic to calculate hydrogen capacity. However, when the HP bed is desorbed, the capacity can be calculated through the pressure increase in the storage volume as well as through the integration of the measured hydrogen flow rate.

The first cycle of the HP bed corresponded to Desorption #7 of the LP bed. Before heating the LP bed, the HP bed valve was opened to the manifold connected to the LP source volume and some hydrogen was absorbed. The high-pressure bed temperature increased to over 30°C when the pressure was increased to 2,200 psi. The source volume pressure drop indicated about 10 grams or about 0.4 wt% absorbed. The flow meter indicated about 12 grams absorbed. This is consistent with the room temperature isotherm for the Ames #2 material (see Figure 2-10).

As the LP bed was then heated the pressure in the two beds rose to over 4,000 psi as more hydrogen was exchanged. As previously discussed, there is no flow or pressure measurement to indicate how much hydrogen is exchanged during this step. The low-pressure bed reached and maintained a temperature of about 145°C. The pressure of the two beds peaked and then dropped slightly over the remaining 10 minutes of the cycle.

It should be noted that a small hydrogen leak was identified in the HP bed at the oil inlet during this half cycle. A handheld hydrogen leak detector was used to isolate the leak to the cover seal, but there was insufficient data to determine the leak rate. The leak was not substantial enough to prevent further testing.

Following the absorption, the HP bed was immediately desorbed. Before switching the heating and cooling of the two beds, the manifold was isolated from the low-pressure source volumes. The flow of hot and cold heat transfer fluid from the heater and chiller to the beds was then switched and the LP bed cooled and absorbed the gas in the upstream manifold while the HP bed heated and drove the pressure downstream up to about 5,000 psi before the BP regulator opened and hydrogen started to flow to the desorption volume. The high-pressure bed continued to heat and desorb for about 15 minutes until the temperature reached about 140°C. At this point, the BP regulator was adjusted until the HP bed was equilibrated with the desorption volume. The desorption volume pressure started at 2,290 psi and ended at 2,341 psi corresponding to 18.5 grams or 0.77 wt% desorbed. Integration of the gas flow meter gave a scaled value of 16.8 grams.

### *6.2.5. High-pressure bed Cycle #2*

The second absorption cycle of the HP bed was performed in two steps and corresponded to Desorption #8 and #9 of the LP bed. Two steps were used to further increase the capacity of the HP bed compared to Cycle #1. For the first step, as with Absorption #1, before heating the LP bed, the HP bed valve was opened to the manifold connected to the LP source volume and some hydrogen was absorbed. The high-pressure bed temperature increased to over 35°C when the pressure was increased to 2,200 psi. The source volume pressure drop indicated about 10 grams or about 0.4 wt% absorbed.

The LP bed was then heated to about 145°C as the HP bed cooled to about 17°C and the bed pressures increased to about 4,300 psi before decreasing over the last 10 minutes of the 25-minute cycle. Following this exchange, the LP bed was filled (Absorption #9) at a pressure of 2,200 psi and absorbed 13 grams of hydrogen.

The second step of Absorption #2 for the HP bed was then performed with the LP bed heated again to 145°C and the HP bed cooled to 16°C. Over the 25-minute cycle, the bed pressures reached 5,841 psi. This higher equilibrium pressure indicated that the HP bed had absorbed more hydrogen.

Desorption #2 of the HP bed began with BP regulator set to a high (unknown) pressure to determine that the bed could produce greater than 700 bar (10,150 psi) pressure. As the HP bed was heated, the pressure in the manifold increased to over 10,000 psi and reached a peak of 10,281 psi when the bed temperature was just 77°C. This demonstrated the pressure capability of the Ames #2 material that was expected. At this point the BP regulator was then adjusted to about 9,900 psi and the bed desorbed to the sink volume over a 10-minute period as the temperature increased to 133°C. The pressure increase in the desorption volume indicated up to 7 grams desorbed at this pressure.

The BP regulator was then adjusted in steps to drop the pressure ultimately to equilibrate with the desorption volume at 2,281 psi with a bed temperature of 145°C. The total hydrogen desorbed was estimated at 22.5 grams or 0.91 wt%. Note that much of the hydrogen desorbed was at a pressure below the desired operation pressure of the compressor. This is due to the highly sloped equilibrium pressure of the Ames #2 alloy as will be discussed later in the performance section.

### *6.2.6. High-pressure bed Cycle #3*

Cycle #3 of the HP bed immediately followed Cycle #2 and was performed with just a single fill from the LP bed. While the HP bed was maintained at 145°C, the LP bed was cooled and filled (Absorption #10) at a pressure of 2,200 psi over about 15 minutes. Heating and cooling was then switched to the beds, and hydrogen was exchanged from the LP bed to the HP bed over a 30 minute period. The bed pressures peaked and then dropped to a final pressure of 3400 psi as the LP bed temperature increased to 145°C and the HP bed temperature decreased to 20°C. This equilibrium pressure indicated that the HP bed was filled to a lower capacity than the previous two cycles.

Desorption #3 of the HP bed reflected this lower capacity. The bed was heated to about 140°C, but desorbed very little hydrogen at a BP regulator setting of 9,000 psi. A total of 16.4 grams (0.67 wt%) was desorbed by decreasing the desorption pressure to equilibrate with the desorption volume at 2,290 psi. As with Desorption #2, this indicated that the HP bed has limited capacity above 700 bar at a temperature of 145°C.

### *6.2.7. High-pressure bed Cycle #4*

A fourth cycle on the HP bed was carried out as a final activation cycle to reach the maximum capacity of the bed. Three fill cycles from the LP bed were used to 'top off' the HP bed and measure the capability to desorb at greater than 700 bar. These were cycles 11-13 of the LP bed and bed temperatures during the exchanges were generally 140-145°C (LP Bed) and 17°C (HP bed). Absorption #11 of the LP bed was performed at 2,132 psi and a temperature of 17°C. The bed absorbed 13.6 grams of hydrogen. Transfer to the HP bed (Absorption #4a) was over a 20 minute duration and the bed pressures reached 3,800 psi. The subsequent fill of the LP bed (Absorption #12) was also 20 minutes at a pressure of 2,075 psi and showed 14.4 grams absorbed. The second transfer to the HP bed (Absorption #4b) was 18 minutes and the bed pressures reached 5,325 psi. The final fill of the LP bed was at 2,053 psi and achieved 7.4 grams. Transfer to the HP bed (Absorption #4c)

was 22 minutes and the bed pressures reached 6,150 psi. This was the highest transfer pressure achieved thus far and indicated additional capacity achieved as compared to Cycle #2. A capacity of 35 grams (1.42 wt%) was estimated for the HP bed during this 3-step process based on the LP bed fills following the exchange cycles.

Desorption #4 of the HP bed was performed by initially heating the bed in steps to determine the pressure achieved prior to desorbing to the sink volume. The temperature and pressure combinations are shown in Table 6-1. As with Desorption #2, this result shows the high-pressure capability of the HP bed achieving 700 bar at a temperature of just 70 °C.

**Table 6-1. HP Bed Equilibrium Pressure at 'Full' Capacity**

| HP Bed Temperature (°C) | Manifold Pressure (psig) |
|---|---|
| 26 | 6,720 |
| 44 | 8,000 |
| 59 | 9,250 |
| 70 | 10,150 |

The BP regulator was then adjusted to about 10,000 psi and the HP bed was heated continuously. As the HP bed temperature increased to about 140°C, the bed desorbed and started filling the desorption volume. Unfortunately, the valve to isolate the LP bed was left open, so once the LP bed pressure dropped to the desorption volume pressure, some of the HP bed gas was absorbed by the LP bed. The valve was subsequently closed, but the pressure rise in the desorption volume was rendered inaccurate to estimate the HP bed capacity. However, the flow meter indicated 8.8 grams (0.36 wt%) desorbed at this pressure setpoint.

The BP regulator was then adjusted in steps to drop the desorption pressure to finally equilibrate with the desorption volume at 2,110 psi. The pressure-based capacity calculation showed 19.2 grams desorbed between 10,000 and 2,110 psi for a total estimate of 28 grams desorbed or 1.13 wt%.

Given the relatively good cycle capacity (1.42 wt% absorbed, 1.13 wt% desorbed) the HP bed was considered fully activated at this point.

## 6.3. Low pressure bed performance

### *6.3.1. Capacity*

The total capacity of the LP bed is somewhat uncertain, but up to 1.7 wt% was initially absorbed. With an absorption pressure of 132-136 bar and desorption to 28-44 bar, a capacity of 1.4 - 1.45 wt% has been calculated. Also, two cycles desorbing to about 160 bar showed a capacity of about 1.0 wt%. This cycling capacity is consistent with, if somewhat lower than, the small sample PCT measurements made earlier in the program shown in Figure 2-12.

Ultimately, the goal for the LP bed is to act as the first stage of the compressor and transfer gas to the high pressure bed. Modeling suggests that the LP bed should be able to transfer up to 1.0 wt% of

hydrogen to the HP bed at a pressure of 400 to 450 bar. During the initial cycling, the pressure capability of the LP bed was checked once. The bed was heated to about 140°C while isolated from the manifold and demonstrated compression from 132 bar (1924 psi) absorption up to 634 bar (9,194 psi). Comparing to Figure 2-12, this pressure is somewhat lower than what would be expected for a 'full' bed. Although, some capacity is used just to pressurize the void volume of the bed and manifold.

### *6.3.2. Cycling performance*

To characterize the cycling performance of the LP stage of the prototype compressor, cycles were run with various fill pressures, desorption pressures, and cycle times. Following Cycles 7-13 which were used to perform activation of the HP bed, Cycles 14-18 were performed to estimate the cycling capacity as a function of fill pressure and desorption pressure combinations. Cycle times for these tests were fixed at 20 minutes. Fill pressures of ~2,175 psi (150 bar) and ~1,934 psi (133 bar) were used along with desorption pressures of 450 bar and 400 bar.

Cycles #14 and #15 were carried out with the 150 bar/450 bar combination. The first cycle was run to get a consistent state in the bed and the second cycle was used to gage the performance. Both cycles were run with a chiller setpoint of 15°C for absorption and a heater setpoint of 150°C for desorption. Absorption #14 showed about 11 grams absorbed as the bed temperature cooled to about 17 °C. Desorption #14 showed about 8.5 grams desorbed to the sink volume with the BP regulator set to about 6,500 psi (448 bar).

The cycle was then repeated. This time the absorption started with the LP bed hot, so the bed had to cool before starting to absorb. It took about 4 minutes for the bed to cool and the pressure to drop to the absorption pressure of about 150 bar. The bed then absorbed for the remaining 16 minutes as it cooled to about 25°C. The capacity was estimated at 10.3 grams or 0.43 wt%.

Desorption #15 was quite similar to #14. The bed heated to about 100°C before the pressure reached 6,500 psi and hydrogen flow to the desorption volume started. About 8.1 grams of hydrogen (0.34 wt%) were desorbed.

These cycles demonstrated that even with a 150 bar fill, desorbing to 450 bar at a temperature of 145°C results in a low delivery capacity. The next cycles investigated the capacity improvement of desorbing to 400 bar (1,934 psi) pressure.

Cycles #16 and #17 were performed with the 150 bar/400 bar combination. As before, the first cycles were run to get a consistent capacity state in the bed. The chiller and heater setpoints for these cycles were the same as the previous cycles and the cycle times were fixed at 20 minutes. Both absorption cycles were run with the bed pressure close to 2,175 psi or 150 bar. Desorption #16 began with the BP regulator set to 6,500 psi from the previous cycle. As the bed heated and the manifold pressure increased above 6,000 psi, the BP regulator was adjusted to 5,800 psi (400 bar). This first desorption cycle delivered 15.9 grams of hydrogen (0.67 wt%). Desorption #17 showed close to the same response as #16. The bed heated to about 90°C in about 3 minutes before the pressure reached 5,800 psi and hydrogen flowed to the desorption volume. A capacity of 15.5 grams of hydrogen (0.65 wt%) was desorbed based on the pressure increase.

These cycles demonstrated that almost twice as much hydrogen was delivered from the LP bed at 400 bar than at 450 bar. However, the capacity delivered (about 2/3 of a weight percent) was lower than the 1.0 wt% targeted for this pressure swing.

To determine the effect of pressure swing versus capacity, Cycle #18 was carried out with a pressure combination of 133 bar/400 bar. Because the same desorption pressure was used as the previous

cycles, only one cycle was run to characterize this pressure combination. Absorption #18 was carried out with the LP bed at 1,934 psi (133 bar) with all other parameters the same as #16 and #17. A slightly lower capacity was observed. Desorption #18 was then run with the same parameters as #16 and #17. The bed heated for about 3 minutes before the pressure reached 5,800 psi (400 bar) and hydrogen began to flow to the desorption volume. A pressure increase in the desorption volume of 41 psi was measured compared to 46 psi in Desorption #17. This equates to 13.8 grams of hydrogen desorbed or 0.58 wt%. So, the capacity dropped by about 11% due to the drop in fill pressure. This information can be used to inform system-level design trades. The 150 bar/400 bar combination provides a 2.67:1 compression ratio with an average flow rate of 0.78 g/min while the 133 bar/400 bar combination provides a 3:1 compression ratio with an average flow rate of 0.69 g/min.

## 6.4. High pressure bed performance

### *6.4.1. Capacity*

The overall capacity of the HP bed is also somewhat uncertain. The best estimate can be made based on Cycle #4 where three fills from the LP bed were used to reach maximum capacity. While a direct measurement was not possible, a capacity of 35 grams (1.42 wt%) was estimated for the HP bed during this 3-step process based on the LP bed fills following the exchange cycles. This fill was completed with a maximum pressure of 6,150 psi (424 bar) with the HP bed temperature near 20°C. The PCT data shown in Figure 2-13 indicates that the capacity at this pressure/temperature combination should be 1.6 wt%. The estimated capacity of the HP bed is about 11% lower.

The subsequent desorption of the HP bed indicated a total of 28 grams (1.13 wt%) desorbed to a pressure of 2,110 psi. This indicates that the remaining 7 grams (0.3 wt%) that was absorbed would be released at a pressure below 2,110 psi. This is consistent with the PCT data shown in Figure 2-13 which indicates a sharp drop in equilibrium pressure at low capacity. However, the pressure is much lower than that indicated in the figure for a capacity of 0.3 wt% and a temperature of 150°C. As will be discussed, additional data from the HP bed indicates that the plateau pressure does not match the high temperature isotherm shown in Figure 2-13.

### *6.4.2. Cycling performance*

The cycling performance of the HP bed was tested over a more limited range of parameters than the LP bed. Due to the highly sloped equilibrium pressure of the HP bed material, the hydrogen capacity at pressures greater than 700 bar was limited. Thus, cycles were only carried out with a desorption pressure of 700 bar. Two different fill pressures for the LP bed were used, however, to assess the tradeoff between overall compression ratio and cycle capacity. To this end, tests were carried out with 133 bar and 150 bar fills of the LP bed. The LP bed was filled and then used to transfer hydrogen to the HP bed which was subsequently desorbed to check capacity. All cycles (LP bed fills, transfers, HP bed desorptions) were carried out with a nominal 20-minute duration for this performance assessment. Heater and chiller setpoints of 150°C and 12°C respectively were used for these cycles. For each fill pressure, two repeats were completed to check repeatability.

Cycles 19-21 of the LP bed were used to fill the HP bed for Cycles 5 and 6. These cycles used 133 bar fill pressure for the LP bed. Two fills from the LP bed were used for Cycle 5 of the HP bed because it was initially empty. During the first transfer from the LP bed to the HP bed, the pressure reached about 3,450 psi with the LP bed temperature at about 145°C and the HP bed temperature at about 25 °C. The LP bed was then filled a second time. The second transfer to the HP bed reached a pressure of about 5,300 psi with approximately the same bed temperatures. This completed the HP bed Cycle

5 absorption and the bed was then desorbed with BP regulator set to 700 bar. As it was heated, the HP Bed started desorbing when it reached 105°C. The sink volume pressure started at 2,837 psi and increased to 2,862 psi which equates to about 8.4 grams or 0.34 wt% delivered at 700 bar.

The cycle was then repeated with 133 bar fill pressure for the LP bed (Cycle 21) and 700 bar desorption pressure for the HP bed (Cycle 6). During the transfer between beds, the pressure ended at 5,640 psi, slightly higher than the Cycle 5 transfer. Temperatures of the beds were comparable to the previous cycle. The Cycle 6 desorption of the HP bed was then carried out. The pressure-based capacity calculation again showed about 8.4 grams or 0.34 wt% delivered at 700 bar.

The next set of cycles were performed with a fill pressure of 150 bar for the LP bed to determine the effect on the 700 bar delivery capacity of the HP bed. A slightly different approach was used for these cycles. Three cycles were performed in series with each including a LP bed fill, a transfer between beds and a HP bed desorption at 700 bar. These were Cycles 22-24 for the LP bed and Cycles 7-9 for the HP bed. The first of these cycles (HP bed Cycle 7) was used to get the HP bed capacity set for the subsequent two cycles. The transfer between beds during this cycle ended with a pressure of about 4,400 psi indicating an incomplete fill, as expected. A small amount of hydrogen was delivered from the HP bed at 700 bar during the Cycle 7 desorption.

Cycle 23/Cycle 8 (LP bed/HP bed) was then performed with a 150 bar fill and a subsequent exchange between beds that ended with a pressure of about 5,900 psi. Note that this pressure is higher than the Cycle 5 and 6 transfers indicating a higher capacity of the HP bed due to the higher fill pressure of the LP bed. During the subsequent desorption of the HP bed, the bed reached 700 bar at a temperature of 87 °C and began desorbing. The capacity calculations indicated 10.2 grams (0.43 wt%) desorbed at 700 bar during the 20 min cycle.

A third cycle was then performed to assess cycle repeatability. The transfer between beds was nearly identical to the previous cycle with a final pressure of 5,940 psi. Cycle 9 desorption of the HP bed was also nearly identical to Cycle 8 with the bed reaching 700 bar at 87°C and desorbing about 10 grams of hydrogen at this delivery pressure.

These cycles demonstrated two compression ratios for the prototype system: 133 bar to 700 bar (5.3:1) and 150 bar to 700 bar (4.7:1) with cycle capacities of 8.4 grams and 10.2 grams. The cycles were carried out with 20-minute durations. Thus a 2-stage compressor of this design would have achieved 25.2 g/hr and 30.6 g/hr respectively. This performance and the effect of cycle time will be discussed in the next section.

## 6.5. Overall Compressor performance

### *6.5.1. Hydrogen Compression and Throughput*

Cycles 19-24 of the LP bed and the corresponding HP bed cycles (Cycles 5-9) were used to assess the HP bed cycling performance with a delivery pressure of 700 bar. These cycles were carried out with 20-minute cycle times and demonstrated overall compressor performance from 133 bar and 150 bar source pressures. The results showed a tradeoff between compression ratio and hydrogen throughput. One other compressor process variable, cycle time, was then investigated. Based on the previous performance testing, a 15-minute cycle time was investigated with the fill/delivery pressure combination of 150 bar/700 bar. It was expected that the reduction in cycle time would reduce the hydrogen throughput per cycle, but might increase the overall compressor throughput by allowing four cycles per hour (15-minute cycles) as compared to three cycles per hour (20 min cycles).

Cycles 25-28 of the LP bed and Cycles 10-13 of the HP bed were used to assess the compressor performance with 15-minute cycles. These four cycles were the first cycles carried out with simultaneous absorption/desorption cycles of the two beds. As the LP bed was filled at 150 bar, the HP bed was desorbed at 700 bar. Then, a transfer between beds was carried out and the cycle was repeated. To carry out the cycles this way a separate sink volume was added to the pressure manifold so that the HP bed wasn't filling the same volume that was used to fill the LP bed. A cylinder with a calibrated volume of 11.2 liters was used for the sink volume. This allowed for accurate capacity estimates of the HP bed cycles.

The first of these cycles started with the Cycle 25 LP bed absorption at 150 bar. The subsequent transfer (LP bed desorption #25/HP bed absorption #10) was used to get the HP bed capacity set for the subsequent three cycles. The transfer between beds during this cycle ended with a pressure of about 5,500 psi indicating a somewhat incomplete fill, as expected. About 7 grams of hydrogen was delivered from the HP bed at 700 bar during the Cycle 10 desorption while the LP bed Cycle 26 absorption took place at 150 bar.

Cycle 26/Cycle 11 (LP bed/HP bed) transfer was then performed between beds that ended with a pressure of about 5,900 psi (407 bar). During the subsequent desorption of the HP bed, the bed reached 700 bar at a temperature of 94 °C and began desorbing. The capacity calculations indicated 8.7 grams (0.36 wt%) desorbed at 700 bar during the 15-minute cycle. The HP bed temperature reached 140 °C when the cycle ended. As before, the LP bed was filled at 150 bar simultaneously with the HP bed delivery.

The third and fourth cycles in this series were then performed to assess cycle repeatability. The transfers between beds was very similar to the previous cycle with final pressures of 5,900 and 5,805 psi (407 and 400 bar) respectively. Cycle 12 and 13 desorptions of the HP bed were also similar to Cycle 11 with the bed reaching 700 bar at 94°C and 95°C and desorbing 8.4 and 8.1 grams of hydrogen, respectively.

As expected, the 15-minute cycles reduced the cycling capacity of the beds compared to 20-minute cycles. With 150 bar fills of the LP bed, the 20-minute cycles resulted in a little over 10 grams of hydrogen delivered from the HP bed at 700 bar. The 15-minute cycles reduced this capacity to a little over 8 grams of hydrogen delivered on average. This capacity reduction is most likely driven by the limited time the beds have to transition from hot to cold temperature and vice versa. For example, during the hydrogen transfers between beds the LP bed heated to 142 °C and the HP bed cooled to 27°C for the 20-minute cycles. The temperatures reached during the transfers for the 15-minute cycles were 138°C and 32°C for the LP and HP beds respectively. This reduced range of bed temperatures directly impacts the equilibrium pressures of the beds effectively reducing the driving pressure difference for hydrogen transfer.

Despite the reduced capacity, however, the 15-minute cycles allow the prototype compressor to cycle four times per hour compared to three times per hour with 20-minute cycles. The net result is that with 15-minute cycles, the compressor delivers more hydrogen per hour. This effect is summarized in Table 6-2. The effective performance of the prototype compressor is 33.6 g/hr with the shorter cycle time as compared to 30.6 g/hr with 20-minute cycles for the same fill and delivery pressures, a 10% increase.

**Table 6-2. Performance Summary for the Prototype Compressor.**

| Fill Pressure (bar) | Delivery Pressure (bar) | Compression Ratio | Heater Temperature (°C) | Chiller Temperature (°C) | Cycle Time (min) | Hydrogen delivered (g) | Flow Rate (g/hr) |
|---|---|---|---|---|---|---|---|
| 133 | 700 | 5.3 | 150 | 12 | 20 | 8.4 | 25.2 |
| 150 | 700 | 4.7 | 150 | 12 | 20 | 10.2 | 30.6 |
| 150 | 700 | 4.7 | 150 | 12 | 15 | 8.4 | 33.6 |

### *6.5.2. Thermal Management and Energy Efficiency*

As described in Section 4.1, the compressor beds were designed based on a trade study to achieve the greatest potential to maximize heat transfer, minimize energy consumption, and meet the target hydrogen pressure range. The combination of the internal helical coil heat exchanger, Teflon sleeve insulation, and ENG thermal conductivity enhancement were chosen to achieve maximum heat transfer and minimum energy use to deliver compressed hydrogen. To assess the performance of this thermal management design, several metrics can be examined. For heat transfer performance the effectiveness of the helical coil heat exchanger and thermal conductivity enhancement can be assessed by considering the temperature response in the metal hydride beds compared to the inlet and outlet temperatures of the heat transfer fluid. The other performance aspect of the helical coil heat exchanger is the relationship between pressure drop, fluid flow rate, and fluid side heat transfer coefficient. To assess energy consumption, heat input to the compressor beds can be examined and compared to hydrogen output to determine energy efficiency.

#### 6.5.2.1. Helical coil oil flow rate and pressure drop

Section 4.2 described the development of the helical coil heat exchanger design. One concern with this design versus other options was the tradeoff between pressure drop and flow rate for the heat transfer fluid. A high flow rate was desired to provide high convective heat transfer to the tube wall to maximize the effectiveness of the heat exchanger. A high flow rate would also result in a low temperature increase of the fluid from inlet to outlet providing a uniform boundary condition throughout the bed. However, the higher the flow rate the higher the pressure and pump power required to pump the fluid through the helical coil.

This tradeoff was considered in choosing the tube diameter for the helical coil for the prototype compressor system. As described in Section 4.2, prototype helical coils were fabricated early in the design phase and laboratory experiments were conducted to measure pressure drop as a function of flow rate. These tests were carried out with water at room temperature. The results of these tests were then compared to a number of literature correlations for pressure drop for helical flow paths. The correlation that best matched the experimental data was then used for design calculations for the prototype compressor. In addition, Nu number correlations for flow through helical tubing were used to estimate the convective heat transfer coefficient for a given heat transfer fluid and flow rate.

For the prototype system, the oil flow system was constrained by the two heat exchangers that were available. Design calculations were carried out to determine the flow rate the heater and chiller could produce provided the properties of the heat transfer fluid and the geometry of the helical coil heat exchanger. The Nu number correlations were then used to determine the resulting heat transfer

coefficient, and this was compared to Comsol simulations to determine the effect on bed performance. This was an iterative process that resulted in the final choice of helical coil geometry, specifically tube diameter.

Comparisons between the predicted oil flow rate and pressure drop to measured values from the prototype compressor system have been carried out. One notable difference from design calculations is that the heat transfer fluid used in the prototype system was changed from Xceltherm 600 to Syltherm 800. The Syltherm fluid has a higher viscosity, especially at cold temperatures, which affected the realized flow rate. Oil pressure and temperature was measured near the inlet and outlet of the helical coil heat exchanger during all performance assessment tests. Oil flow rate was measured during a subset of these tests and was found to be consistent as a function of pressure and temperature. Nominally, the flow rate with hot fluid (> 120 °C) was about 1.8 gpm and with cold fluid (< 25 °C) it was around 0.6 gpm. Table 6-3 shows a comparison of the measured pressure drop, flow rate and oil temperature to that predicted by the correlation that best matched lab data. Syltherm 800 properties were used in the calculation.

**Table 6-3. Measured vs. predicted oil flow rate and pressure drop**

| T_ave_oil (C) | ΔP measured (psi) | Flow rate measured (gpm) | ΔP predicted (psi) | Flow rate predicted (gpm) |
|---|---|---|---|---|
| 145 | 29.5 | 1.8 | 20.9 | - |
| 145 | 29.5 | 1.8 | - | 2.18 |
| 14.5 | 16.5 | 0.54 | 4.5 | - |
| 14.5 | 16.5 | 0.54 | - | 1.15 |

For the hot fluid (145 °C) the predicted pressure drop was about 30% lower than measured for the hot fluid. Alternatively, for the same pressure drop the predicted flow rate was about 20% higher. These comparisons seem reasonable given possible measurement error and accuracy of literature correlations. However, for the cold fluid the predicted pressure drop was over 70% lower and for the same pressure drop the predicted flow rate was about double. This discrepancy between measured and predicted values is perhaps not surprising. Research showed that there was a large range of pressure drop predictions for correlations found in the literature for flow through helical tubes. The correlation that most closely matched lab tests may not be accurate for the range of fluid properties exhibited by Syltherm 800 over the tested temperature range. For example, the viscosity of Syltherm 800 is an order of magnitude greater than water at 20 °C. This result indicates that caution should be taken in using literature correlations for design calculations. Regardless, the flow rate and pressure drop achieved are less important in this application than the heat transfer to the compressor bed, which is discussed in the next section.

#### 6.5.2.2. Helical coil heat transfer coefficient

As mentioned above, convective heat transfer coefficients in the helical coil were predicted using literature Nu number correlations during the design phase. As Section 4.2 describes, the heat transfer coefficients used for the final design calculations were constant values of 5000 $W/m^2K$ and 1000 $W/m^2K$ for heating and cooling respectively. HTCs were also estimated from test data by two methods. Firstly, the measured flow rates and temperatures and Syltherm 800 properties were used to calculate the heat transfer coefficient achieved using the Nu correlations. Secondly, the heat transfer coefficient was estimated using the measured heat input into the helical coil divided by the helical coil surface area to get the average heat flux ($W/m^2$). The heat input to the helical coil was calculated from measured oil flow rate, oil temperature change from inlet to outlet, and Syltherm 800 density and

specific heat capacity. To get an average heat transfer coefficient ($W/m^2K$), the heat flux must be divided by the temperature difference between the heat transfer fluid and the tube wall. An average of the inlet and outlet oil temperatures was used for the first temperature. However, the tube wall temperature was not measured in the experiments. Thus, the heat transfer coefficient was first estimated using the measured metal hydride temperature as the tube wall temperature and then the Comsol model was used to iteratively find a scale factor. A scale factor of 1.5 to 2 provided a good match between Comsol prediction and measured metal hydride temperature and produced an estimated tube wall temperature that seemed reasonable. Using these two methods, time-dependent HTCs were produced.

Firstly, the HTCs estimated from test data are compared to those used for design calculations. Since the design calculations used constant values for each of the heating and cooling periods, average values of the estimated HTCs were calculated from the data where flow rate and temperature were near steady-state. These values are shown in Table 6-4. Values are shown from both methods (heat balance with a scale factor of 2 and Nu correlation) for heating (145 °C oil) and cooling (14.5 °C oil). The two sets of values are the same order of magnitude and close to the values used in design calculations despite the different heat transfer fluid and flow rate assumed.

**Table 6-4. Heat transfer coefficient comparison**

| T_ave_oil (C) | Flow rate (gpm) | HTC heat balance ($W/m^2K$) | HTC Nu ($W/m^2K$) |
|---|---|---|---|
| 145 | 1.8 | 3620 | 4590 |
| 14.5 | 0.54 | 1080 | 945 |

Secondly, a direct comparison between the HTCs using the two different methods from experimental data is shown in Figure 6-8. The HTC based on Nu correlations is noticeably higher during the heating cycle, but the two methods compare quite closely for the cooling cycle. Each method includes several assumptions in interpreting the measured data, so the difference in the values for heating is not surprising. Regardless of the method, the values indicated by the test data approach those used in design calculations and indicate good performance of the helical coil heat exchanger.

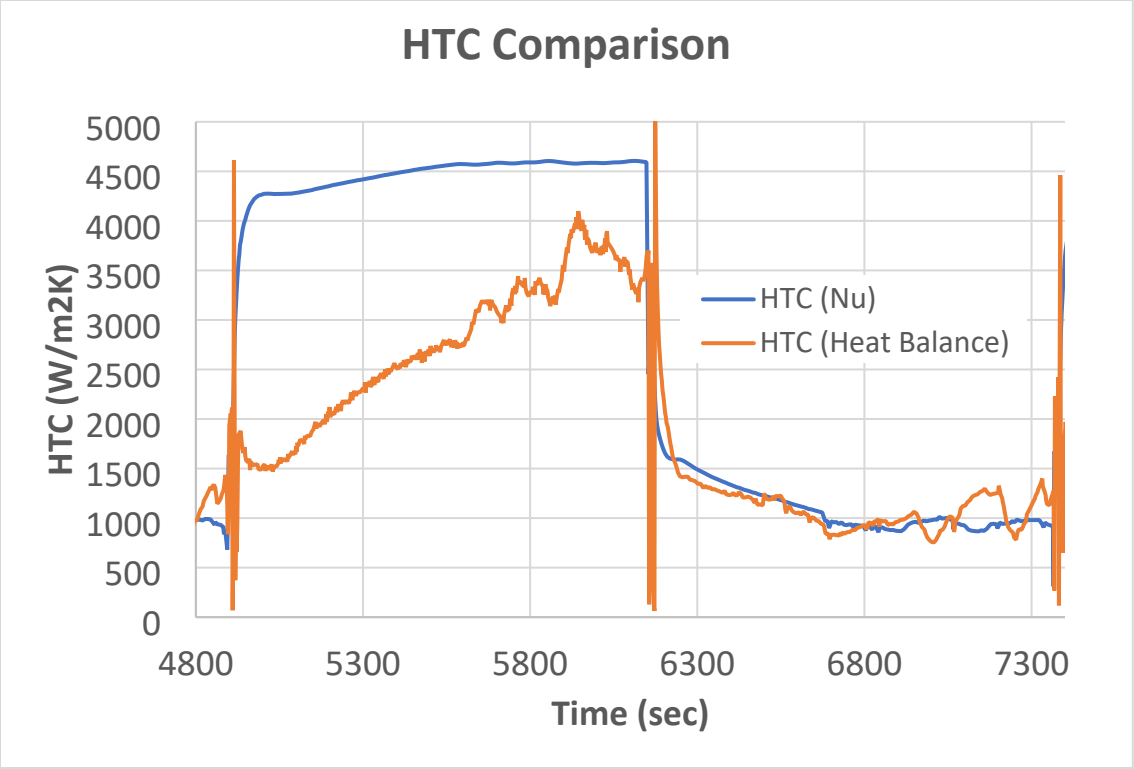


**Figure 6-8. Comparison between methods for calculating HTC.**

#### 6.5.2.3. Compressor bed thermal performance

To assess the overall performance of the helical coil heat exchanger and ENG thermal conductivity enhancement, the measured temperature response in the metal hydride was compared to Comsol predictions. The Comsol model was run using density and estimated thermal conductivity based on the as-built properties of the metal hydride/ENG compacts. This was a density of 3.23 g/cc and effective thermal conductivity of 30 W/mK radially and 14 W/mK axially. Simulations were carried out using the measured oil temperature as the boundary condition along with HTCs from both methods described above. Figure 6-9 shows a comparison of the predicted temperature in the metal hydride at the location where the internal thermocouple provided measured data. The comparison shows that the simulations over-predict the MH temperature response for both HTC methods. During the heating cycle, the Nu-based HTC result significantly over-predicts the initial transient response while the heat balance-based HTC result is much closer to the measured data. This is consistent with Figure 6-8 which shows that the Nu-based HTC is much higher during the heating cycle. During the cooling cycle, both methods produce results that similarly over-predict the measured temperature response. This discrepancy could be due to several causes: the actual HTC could be lower than estimated, the thermal conductivity of the MH/ENG material could be lower than expected, or there could be contact resistance between the helical coil and the MH bed. Each of these causes were examined using the Comsol model.

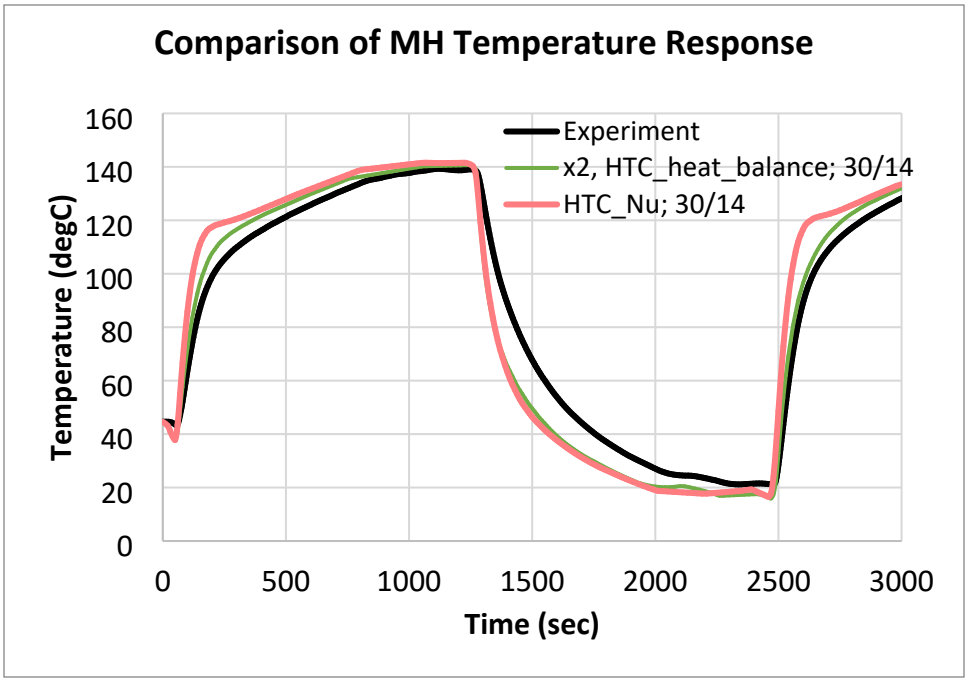


**Figure 6-9. Measured vs. predicted MH temperature (initial HTC estimates)**

While it is possible that the HTC is lower than the estimated values shown in Figure 6-8, it is unlikely that the values are lower than the un-scaled heat balance-based estimate. A comparison to the measured data using this value is shown in Figure 6-10. This comparison assumes the effective thermal conductivity of 30 W/mK radially and 14 W/mK axially and no contact resistance. While the comparison to the measured data is quite close, this would indicate that there is no temperature drop between the helical coil tube temperature and the location where the MH temperature is measured which is near the mid-radius of the vessel.

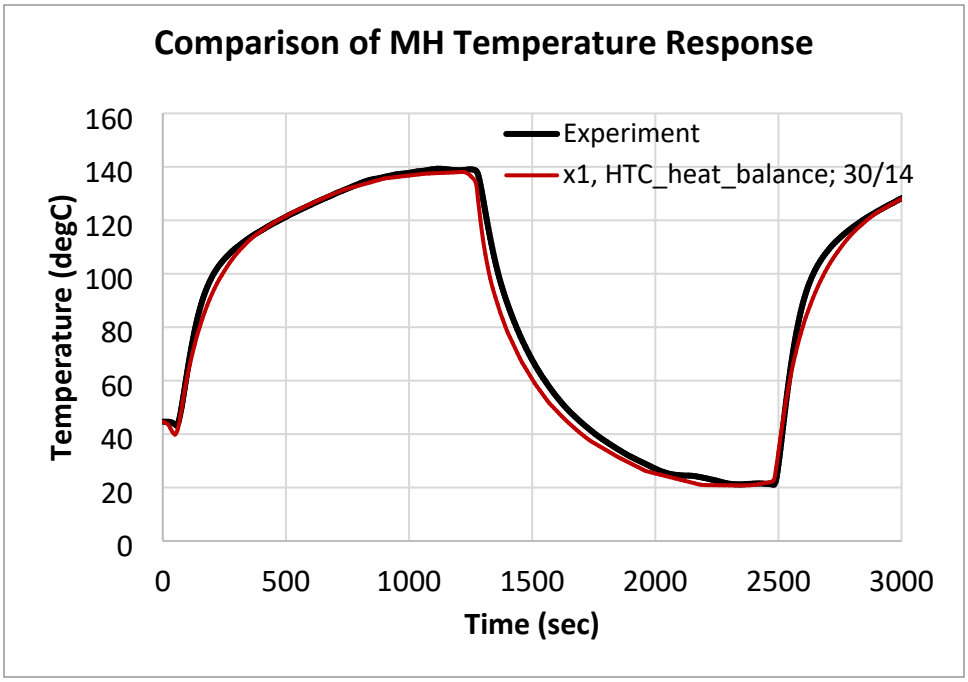


**Figure 6-10. Measured vs. predicted MH temperature (unscaled HTC)**

A more likely explanation is that there is some contact resistance between the helical coil and the MH. The data examined here was taken prior to cycling the bed with hydrogen. Through hydrogen cycling it would be expected that the repeated expansion and contraction of the MH would result in good contact with the helical coil. However, without hydrogen cycling the as-packed material was not in complete contact with the heat exchanger. While the contact resistance cannot be known, the Comsol model was used to examine the effect. An example of this effect is shown in Figure 6-11. This result uses the baseline thermal conductivity and 2X scale factor for the heat balance-based HTC but includes a small (0.1mm) air gap between the helical coil and the MH. As the figure shows, the predicted MH temperature response matches the measured value nearly as well as the unscaled HTC without contact resistance. The conclusion is that these competing affects cannot be decoupled.

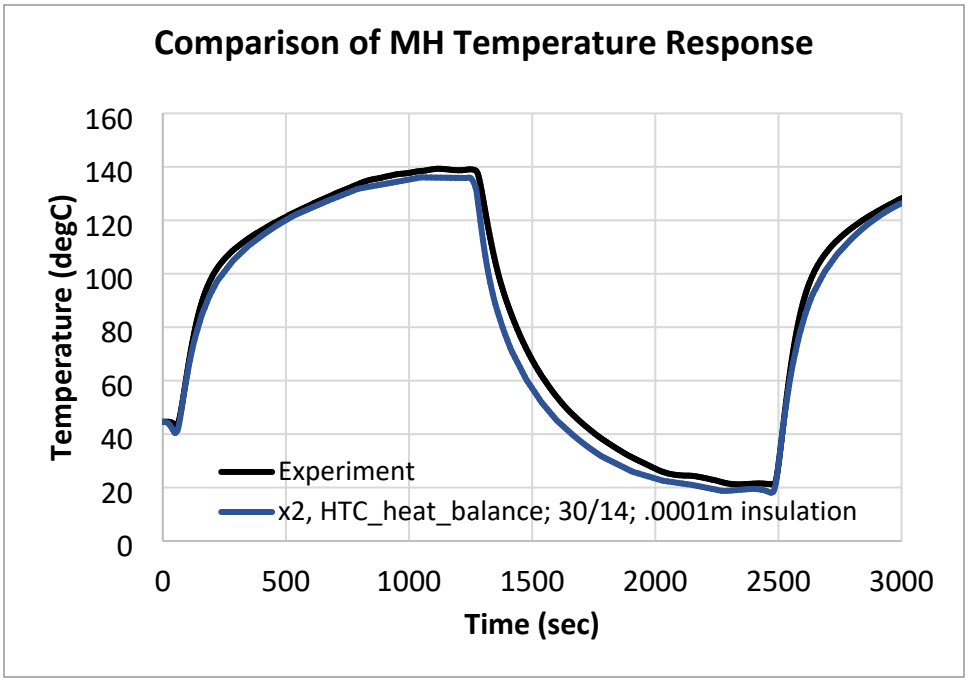


**Figure 6-11. Measured vs. predicted MH temperature (scaled HTC; contact resistance)**

The third factor affecting the MH temperature response is the thermal conductivity of the MH/ENG compacts. The values used in the previous comparisons were based on the values measured from the cylindrical pellets described in Section 4.3 and would be expected to apply to the as-built MH bed. However, the Comsol model was also used to investigate the effect of lower thermal conductivity. The results showed that much lower values of thermal conductivity would be required to account for the differences between the predicted and measured MH temperature response. Since this would be unexpected, the most likely explanation is that a contact resistance existed between the helical coil and the MH and the HTC had values between the 1X and 2X scaled results. Due to the coupled nature of these effects, the actual combination is unknown.

#### 6.5.2.4. Energy consumption and efficiency

During the design phase, the Comsol model as well as the system-level dynamic model were used to estimate the energy required to operate the metal hydride compressor as this is a key performance parameter for the system. As the metal hydride technology is a heat-driven process, these predictions were primarily focused on the amount of heat energy required to heat the compressor beds and drive hydrogen desorption from the metal hydrides. For the prototype system, these values can be estimated from the amount of heat delivered to the beds from the circulating heat transfer fluid. As previously described, this calculation is based on measured oil flow rate, oil temperature change from inlet to outlet, and Syltherm 800 density and specific heat capacity.

To separate the sensible heating of the compressor beds from the heat for desorption, data was used from temperature cycling tests with an inert gas (helium). Tests were carried out with a chiller setpoint of 12 °C and a heater setpoint of 150 °C. The beds were cycled from cold to hot and back multiple times with 20-minute cycle times. Figure 6-12 shows temperature data for the LP Bed during this test. The plot shows oil inlet, oil outlet, and metal hydride temperature over three consecutive cycles. MH temperature cycled from 22 °C to 141 °C and oil outlet temperature cycled from 15 °C to 145 °C.

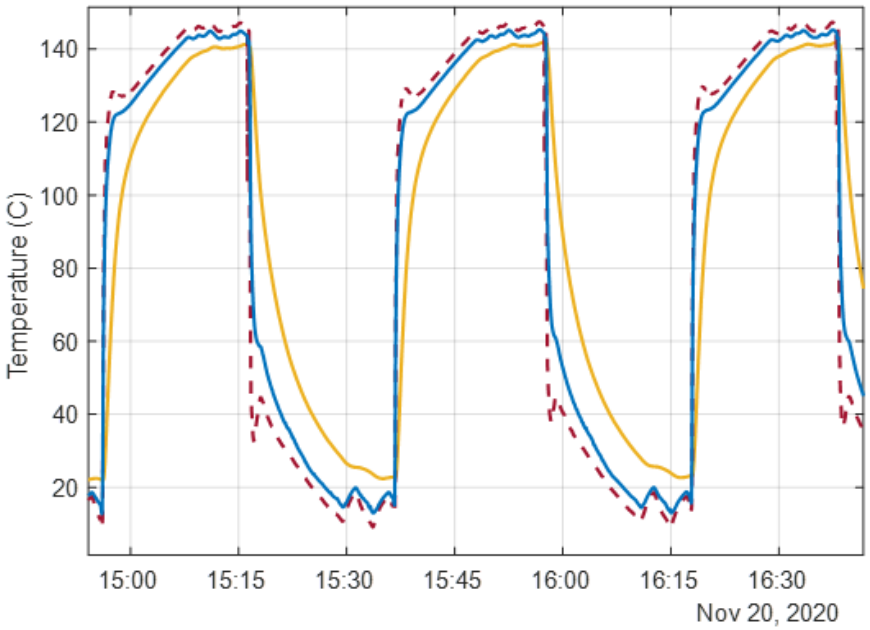


**Figure 6-12. Oil and MH temperatures during consecutive 20 min heating/cooling cycles with He**

Using the oil temperature change from inlet to outlet along with Sylthern 800 properties, heat input in Watts was calculated for the three heating cycles. Integrating this heat input value and summing it over each cycle provided the total heat input to the LP Bed in Joules. Each cycle was consistent with the last cycle showing 638 kJ of heat input to the bed over the 20-minute period. A similar process was used to calculate the heat removed from the bed during the 20-minute cooling cycles. A value of 551 kJ was found. If the system was perfectly adiabatic, the heating and cooling values would match because the state change would be the same in each direction. The fact that the heat input is 87 kJ higher than the heat removed indicates that this heat is lost to the environment during the heating cycles.

As discussed in Section 4.2, the compressor bed design was intended to minimize the sensible heating required to cycle the beds between hot and cold states. This was accomplished in the design primarily by using a high efficiency internal heat exchanger (helical coil) and the Teflon insulating sleeve surrounding the metal hydride. The metric used in the design phase to determine the effectiveness of the design was the excess heat input to the bed beyond that required for the sensible heating of the helical tubing and the metal hydride/graphite compacts. This heat value was calculated from the test data and compared to the total heat input to calculate the excess heat. Table 6-5 shows the results. Helical coil sensible heat is based on average oil temperature change, mass of the helical coil tubing and specific heat capacity of 316L stainless steel. Metal hydride and graphite sensible heat is based on the measured metal hydride temperature change and the mass and specific heat capacities of these materials. 40.5% of the heat input is used to heat the helical coil and MH/graphite while 59.5% is excess heat lost from the helical coil to heating of the Teflon sleeve, vessel, and environment. The excess heat is significant, however if the Teflon sleeve and vessel experience the same temperature swing as the metal hydride, the value would be 4883 kJ. Thus, the measured excess heat value is just 7.8% of what it could be.

**Table 6-5. Sensible heating and excess heat comparison**

| Total heat input (kJ) | Helical coil sensible heat (kJ) | MH sensible heat (kJ) | Graphite sensible heat (kJ) | Excess heat (kJ) |
|---|---|---|---|---|
| 638 | 72.1 | 141.6 | 45.0 | 379.3 |

The Comsol model used during the design phase predicted 210 kJ of excess heat was required for a 15-minute desorption cycle. However, the as-built design was somewhat different than what was assumed in the Comsol model. Also, the design model did not include heat loss to the vessel cover and end. A simulation of the 20-minute cycles analyzed here with an updated model was carried out for comparison. The new Comsol result is shown in Figure 6-13 along with the calculated value from the test data. The Comsol result shown corresponds to Figure 6-11 where the HTC is based on the scaled heat balance method and contact resistance is included. The model result matches the spikes during the heating cycles, but over-predicts the heat input following the initial transient. The spike during the cooling cycle is under-predicted, but the model matches the remainder of the cooling cycle quite closely. Since we are concerned with the heating cycle when considering excess heat, the Comsol prediction was used to calculate the contribution of the excess heat that goes into the vessel cover and end during this cycle. Based on the model prediction, heat loss to the vessel cover and end accounts for almost 50% of the excess heat. A custom designed vessel that minimized this quantity would greatly improve the energy efficiency of the system.

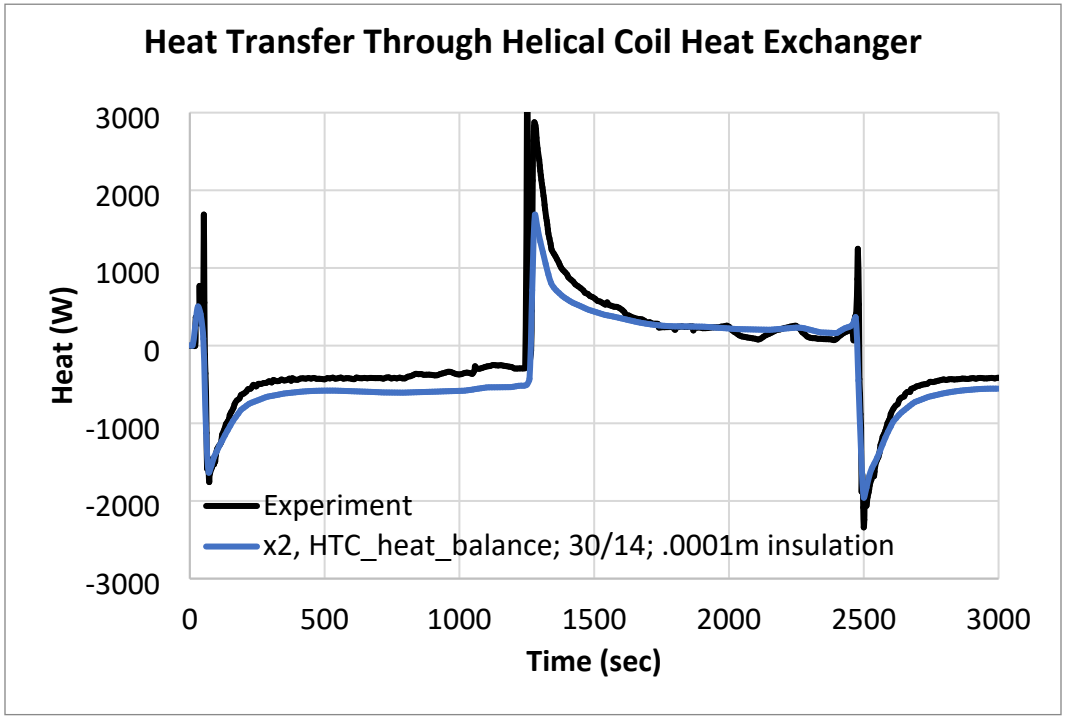


**Figure 6-13. Measured vs. predicted heat input**

# 7. COST ANALYSIS

A preliminary cost analysis for a 100 kg $H_2$/hr production compressor system was completed. A conceptual design for the scaled system was developed and suppliers were contacted to provide estimates for the metal hydrides, heat transfer additives, and pressure vessels.

Initial cost estimates for the metal hydrides have been based on scaling calculations for the production scale system. These scaling calculations are based on several assumptions about the compressor design and performance. Firstly, it is assumed that the system will consist of two beds per stage and two stages, like the prototype system. Operating assumptions include 12-minute half cycles and 1 wt% utilization of the metal hydride. These operating parameters exceed the performance expected and demonstrated by the prototype system. Improved metal hydride performance would be required to provide this level of performance, but literature data suggests that this is feasible. Using these assumptions results in 2000 kg of alloy required per bed, per stage. That translates to 4000 kg each of LP and HP alloys. For heat transfer enhancement, the alloys would be combined with 800-1200 kg of ENG. For reference, a more optimistic assumption of 10-minute half cycles and 1.5 wt% utilization would reduce the required mass of metal hydrides and ENG by 44%.

Initial estimates for at-scale production of metal hydride alloys by vendors in the US, Japan, and China have been solicited. These estimates show the price of the alloys to be between $17/kg and $43/kg. For 8000 kg of alloy, this would be a cost of $136,000 to $344,000 per compressor. A quote was also received for the expanded natural graphite. ENG costs for this scale are quoted at $46/kg. For 800-1200 kg the cost per compressor would be $36,800 to $55,200, a not insignificant amount. More work to refine these estimates and expand the vendor base from which estimates have been received should be completed.

The next largest perceived cost for the compressor are the pressure vessels. The size and number of pressure vessels per compressor was based on the need to store 2000 kg of alloy per bed. The original prototype design was based on storing 25 kg of alloy in each vessel. That capacity would result in 80 vessels for each compressor bed. Combining this number of vessels would be impractical for a commercial system, so scaling calculations were performed to reduce the number to 10 vessels per bed. The resulting conceptual design consists of vessels with 12-inch inner diameter and 36 inch internal length. Each vessel would contain a helical coil heat exchanger fabricated from 1-inch diameter tubing and 200 kg of a compacted mixture of metal hydride alloy and graphite. The low-pressure stage would consist of 20 vessels and 850 ft of tubing rated to > 4000 psi. The high-pressure stage would consist of 20 vessels and 850 feet of tubing rated to >13,000 psi.

An initial estimate was obtained for these pressure vessels fabricated from Nitronic 50. For the low-pressure stage, each vessel was quoted at $43,415. For 20 of these vessels the cost would be $868,296. For the high-pressure stage, each vessel was quoted at $56,472 resulting in a cost of $1,129,440 for 20 vessels. Based on these estimates, the total cost per compressor would be almost $2M. Because of this very high cost, other options for the vessel design including alternative materials and methods of fabrication were examined. These alternatives include alloy steel vessels and Type II and Type III composite vessels like those used for high pressure storage at hydrogen fueling stations.

For a two-stage compressor, an alloy steel vessel could only be designed for the low-pressure stage. Alloy steel vessels are designed for H2 service using ASME BPVC Article KD-10 (Fracture mechanics). Calculations for vessel design include leak before rupture calculations and fatigue crack

growth analysis. A ten-inch inner diameter vessel with 2.5-inch thick walls could be cycled between 50 and 300 bar. Calculations show that hoop stress is only 9% of the tensile strength and leak before rupture criteria is met with $K_{max}$ = 35.9 MPa $m^{1/2}$. A fatigue crack growth analysis gives 187,000 cycles to failure for a 5% crack depth (3.2 mm) and >500,000 cycles to failure for 3% crack depth (1.9 mm).

A three-stage compressor design could allow for all vessels to be fabricated from alloy steel. The high-pressure stage would be the limiting factor with compression from 550 to 900 bar. Fracture mechanics analysis shows that a four-inch wall thickness would be needed to meet design criteria. However, the three-stage design would require 50% more vessels and metal hydride than a two-stage design for the same performance (flow rate and compression ratio). Alloy steel vessels should be much less costly than Nitronic 50, but actual quotes would be required to complete a full cost comparison.

A Type II steel-lined composite vessel could be an alternative. For example, FIBA offers a steel-lined, carbon, hoop-wrapped vessel designed exclusively for the hydrogen fueling market (see Figure 7-1). These vessels are designed for an operating pressure of 13,500 psi. Standard size is 16" OD in several lengths from 7' to 29'. For the MH compressor application, the vessel would have to be designed with on open end to accommodate loading the vessel with the metal hydride and heat exchanger. Discussions with several manufacturers of Type II vessels were conducted to determine if such a design was feasible. Several options were discussed as being feasible, but no official quote was received.

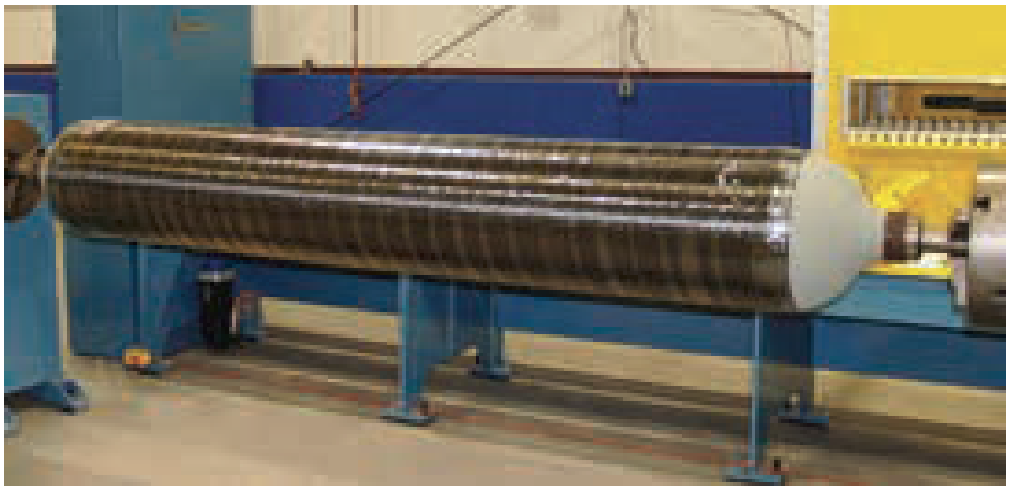

**Figure 7-1. Type II steel-lined carbon composite vessel**

The final vessel alternative considered was an open-ended Type III vessel like that shown in Figure 7-2. One company was contacted who have experience with this type of design. Designs have been produced that would meet the pressure and temperature requirements for the MH compressor (pressures to 1000 bar and temperatures up to 163 °C). An official quote was requested for the full-scale system design and indicated that the vessels could be produced in large quantities for ~$10,000 each. If these vessels were used for just the HP stage, 20 vessels would be required per compressor for a cost of $200,000. This is a significant reduction (~5X) compared to the Nitronic 50 vessels.

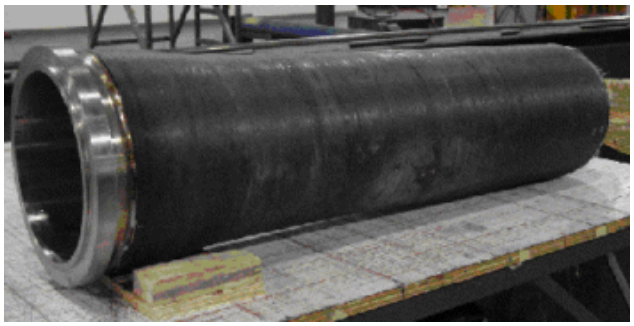

**Figure 7-2. Type III aluminum lined carbon composite vessel**

# 8. SUMMARY AND CONCLUSIONS

There were three overall objectives for this project. The first was to develop and demonstrate on a laboratory scale a two-stage metal hydride compressor with a feed pressure of approximately 100 bar delivering high purity $H_2$ gas at an outlet pressure ≥ 875 bar. The second was to demonstrate an increase in the technology readiness level (TRL) of this technology and enable the development of a comprehensive cost analysis for a production system scaled to 100 kg $H_2$/hr flow rate. The third was to demonstrate through engineering analysis that the compressor design is capable of an energy efficiency of ≤ 4.0 kWh-electric/kg.

## 8.1. Objective #1

Towards the first project objective, metal hydrides were investigated and characterized to find LP and HP materials to compress hydrogen from 100 bar to 875 bar. A literature review identified a dozen candidate materials. Alloy samples were procured from commercial sources for characterization by the project team and GWE. Nine different materials were characterized via PCT measurements and Hydralloy C5 was identified as a good LP candidate. However, a HP material was not identified that could meet design requirements. It was outside the scope of this project to develop metal hydrides; however it is clear from this work that materials development is needed to meet ultimate performance goals for MHCs. Thus, a compromise was made for the prototype demonstration to use the Ames #3 and #2 materials to compress from 150 bar to 875 bar with limited capacity and hydrogen flow.

Through a design trade study an optimized design was developed for the 2-stage MH compressor. The design includes two beds per stage for quasi-continuous hydrogen flow with each bed comprised of cylindrical high-pressure vessels and a helical coil heat exchanger. The helical coil heat exchanger provides uniform heat transfer distance with a single flow path simplifying manifolding and minimizing heat exchanger volume. Compressor thermal management also included thermal conductivity enhancement via ENG compacts and an insulation sleeve to prevent heat loss to the vessel and environment.

A prototype compressor was designed and fabricated to demonstrate proof of concept that used one bed per stage to simplify the experimental system and reduce cost. The prototype was scaled down to 3 kg of material per bed and used a commercially available vessel design from HiP with identical LP and HP vessels. The vessels were designed to 15 ksi MAWP and used Nitronic 50 bodies for high pressure hydrogen compatibility and high strength. The vessel design was compatible with the helical coil heat exchanger with high pressure seals through body and lid. The vessels included a single hydrogen inlet/outlet and one thermocouple feedthrough. The vessels were also designed to accommodate an insulating Teflon liner and a hydrogen distribution tube made from a Mott sintered metal sparge tube.

The helical coil heat exchanger was fabricated from 3/8" diameter medium pressure (20 ksi MAWP) 316 SST tubing. The helical coil geometry was optimized through modeling and analysis considering fluid heat transfer coefficient, flow rate and pressure drop. The heat transfer fluid for the heat exchanger was selected through analysis of HTC, flow rate and pressure drop. Syltherm 800 was used as compromise for compatibility with heat exchange equipment and limited the maximum temperature to 150 °C.

A process was developed to produce MH/ENG compacts in custom shapes achieving high radial thermal conductivity. Various combinations of graphite additives, mass fractions and compaction pressures were investigated based on procedures by Pohlman et al. Radial thermal conductivity of 30 W/mK was demonstrated in cylindrical pellets with 150 MPa compaction pressure. Custom die sets were designed and fabricated to make pellet shapes to fill the helical coil heat exchanger. 56 pie shaped pellets and 26 ring pellets for each bed were fabricated with ball-milled MH mixed with ENG and compacted with a hydraulic press in an Argon glove box.

Bed vessels were assembled with the pellets. The LP bed was loaded with 2.8 kg of material and the HP bed was loaded with 2.9 kg of material. With a 15% graphite and 85% metal hydride mixture, each bed was loaded with about 2.4 kg of metal hydride. The effective density of the LP material was 3.23 g/cc and the effective density of the HP material was 3.35 g/cc.

A test apparatus was assembled for the prototype compressor demonstration. The test apparatus consisted of three primary systems: a high-pressure hydrogen manifold, a temperature control system with hot and cold oil recirculation loops, and a data acquisition and control system. Control of hydrogen flow through the compressor was achieved through the pressure differences across a set of check valves between the supply and the low-pressure bed, the low and high-pressure beds, and the high pressure bed and a back pressure regulator to control delivery pressure. The pressure of the beds was, in turn, controlled by the temperature of the two hydride beds achieved by directing the flow of the two fluid loops using a series of pneumatically actuated valves. These valves could be controlled manually or by a timer and relay circuit that triggered valves to open or close at preset time intervals chosen based on the desired cycle time of the compressor.

The temperature control system consisted of two oil recirculation loops, one at a low temperature and one at a high temperature. The low temperature loop consisted of a chiller with self-contained pump and heat exchanger. The chiller circulated heat transfer fluid at a specified temperature through the oil manifold and had a cooling capacity of 3 kW. The high temperature loop was operated with another self-contained unit with a pump and a 6 kW resistive heater. The unit had an internal expansion tank to allow for expansion of the fluid at high temperature. Flow from the two oil loops was directed to either the low or high-pressure bed through a series of 3-way valves for heating and cooling.

A simple data acquisition and was assembled for the system. Data collected consisted of the flow rate and temperature of the two oil loops, supply pressure, intermediate pressure, and delivery pressure of the compressor, internal and external temperatures of the two compressor beds, and delivered hydrogen flow rate.

Compressor beds were tested with helium to demonstrate pressure and temperature cycling capability of the system prior to hydrogen operations. Initial tests with high pressure He at high temperature resulted in seal failures. The seals were redesigned, and the vessels were modified to correct a design flaw. A second round of testing revealed cover seal leaks. A second modification of the cover seal design was completed and final checks with He through pressure and temperature cycling were successful.

Compressor beds were then activated with hydrogen and performance was characterized. Three hydrogen cycles were used to activate the LP bed and up to 1.7 wt% was initially absorbed. With an absorption pressure of 132-136 bar and desorption to 28-44 bar, a capacity of 1.40 - 1.45 wt% was calculated. This cycling capacity was consistent with, if somewhat lower than, the small sample PCT measurements of the Ames #3 material. During the activation cycles, the LP bed demonstrated a maximum compression from 132 bar (1924 psi) up to 634 bar (9194 psi) with a temperature swing from 15 to 145 °C.

A total of 28 cycles were completed with the low-pressure stage. The cycling performance of the low-pressure stage was assessed with fill pressures of 133 bar (1934 psi) and 150 bar (2175 psi) and desorption pressures of 400 bar (5800 psi) and 450 bar (6525 psi). The LP bed demonstrated compression from 150 bar to 400 bar (2.67:1 compression ratio) with 15.7 grams of hydrogen delivered in 20 minute cycles (average flow rate of 47.1 g/hr) and from 133 bar to 400 bar (3:1 compression ratio) with 13.8 grams of hydrogen delivered in 20 minute cycles (average flow rate of 41.4 g/hr).

Four cycles were used to activate the HP bed. A capacity of 35 grams (1.42 wt%) was estimated for the HP bed during the final 3-step absorption based on the LP bed fills following the exchange cycles. This fill was completed with a maximum pressure of 6150 psi (424 bar) with the HP bed temperature near 20 °C. The Ames #2 PCT data indicated that the capacity at this pressure/temperature combination would be 1.6 wt%, so the capacity of the HP bed was about 11% low. The subsequent desorption of the HP bed showed that while 700 bar (10,150 psi) pressure was achieved at a temperature of just 70 °C, only 8.8 grams was desorbed at this pressure although a total of 28 grams (1.13 wt%) was desorbed to a pressure of 2110 psi. This indicated that due to the highly sloped equilibrium pressure of the Ames #2 material, the hydrogen capacity at pressures greater than 700 bar was very limited. Thus, subsequent performance assessment cycles were only carried out with a desorption pressure of 700 bar.

A total of 13 cycles were completed with the high-pressure stage. Cycles 5-9 assessed cycling performance with 20-minute cycle durations, fill pressures of the low-pressure stage of 133 bar and 150 bar and desorption pressure of the high-pressure stage of 700 bar (10,150 psi). These cycles demonstrated overall system compression from 133 bar to 700 bar (5.26:1 compression ratio) with 8.4 grams (0.34 wt%) delivered in 20 minute cycles (average flow rate of 25.2 g/hr) and compression from 150 bar to 700 bar (4.67:1 compression ratio) with 10.2 grams (0.43 wt%) delivered in 20 minutes (average flow rate of 30.6 g/hr).

Cycles 25-28 of the LP bed and Cycles 10-13 of the HP bed were used to assess the compressor performance with 15-minute cycles using 150 bar/700 bar fill/delivery pressure. An average of 8.4 grams (0.34 wt%) was delivered in these 15-minute cycles. Despite the reduced capacity, the 15-minute cycles allow the prototype compressor to cycle four times per hour compared to three times per hour with 20-minute cycles. The net result is that with 15-minute cycles, the compressor delivers more hydrogen per hour. The effective performance of the prototype compressor is 33.6 g/hr with the shorter cycle time as compared to 30.6 g/hr with 20-minute cycles for the same fill and delivery pressures, a 10% increase.

In addition to the hydrogen compression performance, experimental data was used to assess the performance of the thermal management design. Several metrics were examined including the relationship between pressure drop, fluid flow rate, and fluid side heat transfer coefficient of the

heat exchanger, the heat transfer effectiveness of the helical coil heat exchanger and thermal conductivity enhancement, and the overall energy efficiency of the bed design. An analysis of the pressure drop and flow rate of the heat transfer fluid showed that for the hot fluid (145 °C) the values were within possible measurement error and accuracy of literature correlations, but the predicted pressure drop for the cold fluid was over 70% lower than that measured and for the same pressure drop the predicted flow rate was about double. This larger discrepancy was attributed to the high viscosity of the Syltherm 800 fluid compared that of water which the correlations were based on.

The heat transfer effectiveness of the helical coil heat exchanger coupled with the enhanced thermal conductivity of the MH/ENG pellets was assessed by comparing the measured temperature response of the bed to predictions from the Comsol model. With the expected thermal conductivity of the material and a Nu-based heat transfer coefficient, the Comsol model predicted a much faster temperature response than that measured. However, the measured response could be matched with an HTC based on a heat balance approach along with a contact resistance between the helical coil and the MH. This indicated that good performance was achieved with the helical coil heat exchanger although not as good as that predicted by the Nu correlation. While conclusive evidence did not exist to identify the thermal conductivity achieved the evidence suggested it was at or near that achieved with the cylindrical pellets.

The overall energy efficiency of the bed design was assessed by examining the excess heat added to the bed during desorption cycles. While the percentage of total heat input attributed to excess heat was high (~60%), it was determined that this was a small fraction (7.8%) of the potential heat loss to the vessel. Also, it was shown by the Comsol model that a large fraction of the excess heat went to heating the vessel lid and base which could be minimized in a custom vessel design.

## 8.2. Objective #2

Towards the second objective, a conceptual design for a 100 kg/hr compressor was developed based on the prototype system. The 100 kg/hr compressor would consist of vessels with 12-inch inner diameter and 36-inch internal length. Each vessel would contain a helical coil heat exchanger fabricated from 1-inch diameter tubing and 200 kg of a compacted mixture of metal hydride alloy and graphite. The conceptual design was based on several assumptions about the compressor design and performance. Firstly, it is assumed that the system would consist of two beds per stage and two stages, like the prototype system. Operating assumptions include 12-minute half cycles and 1 wt% utilization of the metal hydride. These operating parameters exceed the performance expected and demonstrated by the prototype system. Improved metal hydride performance would be required to provide this level of performance, but literature data suggests that this is feasible.

With these assumptions, costs were estimated for the costliest aspects of the design: metal hydrides, heat transfer additives, and pressure vessels. Metal hydride estimates show the price of the alloys to be between $17/kg and $43/kg. For 8000 kg of alloy, this would be a cost of $136,000 to $344,000 per compressor. ENG costs for this scale are quoted at $46/kg. For 800-1200 kg the cost per compressor would be $36,800 to $55,200. Three options were identified for the vessel design: alloy steel, Type II and Type III vessels. Alloy steel vessels could be used for the LP stage of a two-stage compressor or for all vessels in a three-stage design. However, no quotes were gathered for this option or for Type II vessels. An official quote was received for Type III vessels indicating that the vessels could be produced in large quantities for ~$10,000 each. If these vessels were used for just

the HP stage, 20 vessels would be required per compressor for a cost of $200,000. While incomplete, this cost analysis suggest that a 100 kg/hr MHC would cost between $600,000 and $800,000.

## 8.3. Objective #3

To address the third overall objective, a system-level dynamic model was developed and exercised to demonstrate the performance of the design. The model demonstrated feasibility of 50 - 875 bar $H_2$ compression and delivery at reasonably achievable temperatures through system-level analysis of a baseline design using literature data for available metal hydrides. The model showed 69% bed utilization with 15-min half cycles resulting in 1.18 kg/hr flow rate for 25 kg beds and 10.3 kWh/kg energy efficiency. The model was used to complete a parameter study to probe the compressor design space including the effects of cycle time, alloy, feed pressure, and bed geometry on hydrogen flow rate and energy efficiency.

Several approaches were identified to achieve 4.0 kWh/kg energy efficiency and hydrogen compression cost targets including heat recuperation, waste heat utilization, and heat pump options. A heat recuperator design was conceptualized that could reduce the sensible heat requirement of the system by ~40%. It was shown that providing this heat by a natural gas burner (assuming natural gas cost of $0.065/mm-btu and 85% burner efficiency) would result in an operating cost of $ 0.25/kg. This would be comparable to a conventional compressor using 2.3 kWh/kg at $0.11/kWh electricity cost.

A simple analysis of an ideal heat pump cycle showed that a VCC with R21 operating between 25 and 125 °C has a coefficient of performance of 2.7 that would result in a compressor energy requirement 3.7 kWh/kg. A VCC system with methanol as the refrigerant might further reduce the energy use to 3.1 kWh/kg.

# REFERENCES


1. Sprik, S., et al., *Next Generation Hydrogen Station Composite Data Products: All Stations (Retail and Non-Retail Combined), Data through Quarter 3 of 2016*. 2017, National Renewable Energy Lab.(NREL), Golden, CO (United States).
2. Lototskyy, M.V., et al., *Metal hydride hydrogen compressors: a review*. International journal of hydrogen energy, 2014. **39**(11): p. 5818-5851.
3. Yartys, V.A., et al., *Metal hydride hydrogen compression: recent advances and future prospects*. Applied Physics A, 2016. **122**(4): p. 415.
4. Schlapbach, L. and A. Züttel, *Hydrogen-storage materials for mobile applications*. Materials for sustainable energy: a collection of peer-reviewed research and review articles from nature publishing group, 2011: p. 265-270.
5. Wang, X., H. Liu, and H. Li, *A 70 MPa hydrogen-compression system using metal hydrides*. International journal of hydrogen energy, 2011. **36**(15): p. 9079-9085.
6. Hu, X.-c., et al., *A 38 MPa compressor based on metal hydrides*. Journal of Shanghai Jiaotong University (Science), 2012. **17**(1): p. 53-57.
7. Kelly, N.A. and R. Girdwood, *Evaluation of a thermally-driven metal-hydride-based hydrogen compressor*. International journal of hydrogen energy, 2012. **37**(14): p. 10898-10916.
8. Cieslik, J., P. Kula, and S. Filipek, *Research on compressor utilizing hydrogen storage materials for application in heat treatment facilities*. Journal of alloys and compounds, 2009. **480**(2): p. 612-616.
9. Karagiorgis, G., et al., *Design, development, construction and operation of a novel metal hydride compressor*. international journal of hydrogen energy, 2017. **42**(17): p. 12364-12374.
10. Madaria, Y. and E.A. Kumar, *Effect of heat transfer enhancement on the performance of metal hydride based hydrogen compressor*. international journal of hydrogen energy, 2016. **41**(6): p. 3961-3973.
11. Laurencelle, F., et al., *Experimental study on a metal hydride based hydrogen compressor*. Journal of Alloys and Compounds, 2009. **475**(1-2): p. 810-816.
12. Popeneciu, G., et al. *Investigation on a three-stage hydrogen thermal compressor based on metal hydrides*. in *Journal of Physics: Conference Series*. 2009. IOP Publishing.
13. Li, H., et al., *A study on 70 MPa metal hydride hydrogen compressor*. Journal of alloys and compounds, 2010. **502**(2): p. 503-507.
14. Hagström, M., et al., *High-pressure AB2 metal hydrides with low hysteresis*. Journal of materials science, 2000. **35**(1): p. 127-131.
15. Zotov, T., et al., *IMC hydrides with high hydrogen dissociation pressure*. Journal of alloys and compounds, 2011. **509**: p. S839-S843.
16. Guo, X., et al., *Laves phase hydrogen storage alloys for super-high-pressure metal hydride hydrogen compressors*. Rare Metals, 2011. **30**(3): p. 227-231.
17. Capurso, G., et al., *Development of a modular room-temperature hydride storage system for vehicular applications*. Applied Physics A, 2016. **122**(3): p. 236.
18. Available from: https://github.com/PurdueH2Lab/MetalHydrideToolbox.
19. C. Arpagaus, F.B., J. Schiffmann, and S.S. Bertsch, . *Review on High Temperature Heat Pumps*. in *Proceedings of the European Heat Pump Summit*. Oct. 2017.
20. Herbrig, K., et al., *Hydrogen storage systems based on hydride–graphite composites: computer simulation and experimental validation*. International Journal of Hydrogen Energy, 2013. **38**(17): p. 7026-7036.

21. Pohlmann, C., et al., *Heat and gas transport properties in pelletized hydride–graphite-composites for hydrogen storage applications.* International journal of hydrogen energy, 2013. **38**(3): p. 1685-1691.
22. Pohlmann, C., et al., *Solid-state hydrogen storage in Hydralloy–graphite composites.* Journal of power sources, 2013. **231**: p. 97-105.
23. Herbrig, K., et al., *Investigations of the structural stability of metal hydride composites by in-situ neutron imaging.* Journal of Power Sources, 2015. **293**: p. 109-118.
24. Heubner, F., et al., *Mechanical stresses originating from metal hydride composites during cyclic hydrogenation.* International Journal of Hydrogen Energy, 2015. **40**(32): p. 10123-10130.

# DISTRIBUTION

**Email—External (encrypt for OUO)**

| Name | Company Email Address | Company Name |
|---|---|---|
| Neha Rustagi | neha.rustagi@ee.doe.gov | DOE HFTO |
| Craig Jensen | thecraig22@hotmail.com | Hawaii Hydrogen Carriers |
| Robert Bowman | rcbjr1967@gmail.com | |
| Bart Smith | smithdb@ornl.gov | ORNL |

**Email—Internal**

| Name | Org. | Sandia Email Address |
|---|---|---|
| Cheryl Lam | 08751 | clam@sandia.gov |
| Anne Mallow | 08446 | amallow@sandia.gov |
| Brendan Davis | 08367 | bcdavi@sandia.gov |
| Kristin Hertz | 08367 | klhertz@sandia.gov |
| Vitalie Stavila | 08341 | vnstavi@sandia.gov |
| Mark Allendorf | 08340 | mdallen@sandia.gov |
| Technical Library | 01177 | libref@sandia.gov |

This page left blank

This page left blank

Sandia National Laboratories

Sandia National Laboratories is a multimission laboratory managed and operated by National Technology & Engineering Solutions of Sandia LLC, a wholly owned subsidiary of Honeywell International Inc. for the U.S. Department of Energy's National Nuclear Security Administration under contract DE-NA0003525.